Title
Direct Ink Writing of Architected Materials for Mechanical and Biological Applications

Author
Thiraux, Raphael

Publication Date
2023

Peer reviewed|Thesis/dissertation

UNIVERSITY OF CALIFORNIA,

IRVINE

Direct Ink Writing of Architected Materials for Mechanical and Biological Applications

DISSERTATION

submitted in partial satisfaction of the requirements

for the degree of

DOCTOR OF PHILOSOPHY

in Materials Science and Engineering

By

Raphael Pierre Thiraux

Dissertation Committee:
Professor Lorenzo Valdevit, Chair
Professor Ali Mohraz
Professor Elliot Botvinick

2023

DEDICATION

To

My family, friends, wife, and daughters

TABLE OF CONTENTS

LIST OF FIGURES

LIST OF TABLES

ACKNOWLEDGMENTS

I would like to acknowledge my advisor, Dr. Lorenzo Valdevit, for giving me the opportunity to work with him. He has always been supportive not only of my work and my choice of research area of interest, but also in my personal life—his flexibility allowed me to complete my PhD while navigating life as a new Dad—first to Adelaide in 2018 and then Eloise in 2022.

I would like to thank the members of the committee, Dr. Ali Mohraz and Dr. Elliot Botvinick, and the members of my qualifying exam, Dr. Dan Mumm and Dr. David Kisailus for their constructing critics and valuable suggestions. Dr. Mohraz has been assisting me on the rheological aspect of my research since the beginning of PhD. He allowed me to use his lab facilities and shared his knowledge and expertise with me. Dr. Dan Mumm let me use his lab facilities which was essential for the success of my research. A very special thank you to Dr. Alexander Dupuy for his unwavering guidance. He helped me stay focused on the big picture and become a well-rounded scientist. I am fortunate to have had him as a mentor and appreciate that his honesty and guidance helped me become a better researcher and writer.

I would like to thank the members of the Valdevit's group, particularly Kate Ainger who recently joined the group and has been helping finish up my PhD, I wish her good luck for her PhD. I would like to acknowledge former members, Dr. Anna Guell, Dr. Jens Bauer, Dr. Cameron Crook, and Nicolas Ruvalcaba for their support, help, and valuable insights. I really enjoyed our conversations during lunch. I would like to acknowledge Dr. Alan Widgerow, Dr. Mary Ziegler, and their team. I have been in charge for the manufacturing aspect of their project on the ear reconstruction. I feel lucky to have been involved in a such exciting project which could have an immense impact on the community. They have been extremely supportive to make sure that this project would be meaningful enough to be part of this thesis. I would like to knowledge the team

ceramics led by Dr. Alexander Dupuy, and composed of Dr. Xin Wang, Arturo Meza, Salma El-Azab, Justin Cortez, Jacob Normam for letting me prepare with them for TMS. During my last quarter, I was able to attend Dr. Diran Apelian's group meeting. I am thankful for his valuable lessons and advice from his industry experience. I would also like to acknowledge Tim Rupert's group for sharing the lab space. I would like to acknowledge Esther Hessong, Dr. Tianjiao Lei and Dr. Megan McCarthy for their friendship. During my PhD, I had the opportunity to run mechanical testing for Dr. Dave Dimas and Metrolaser. I am thankful to have had this opportunity as it allowed me to solidify my mechanical testing skills. I am also thankful for all the conversation I had with Dr. Dave Dimas and for his advice and help in my job search.

I would like to acknowledge support from the BIAM-UCI Research Center. I acknowledge the use of facilities and instrumentation at the UC Irvine Materials Research Institute (IMRI) supported in part by the National Science Foundation Materials Research Science and Engineering Center program through the UC Irvine Center for Complex and Active Materials (DMR-2011967).

CURRICULUM VITAE
Raphael Pierre Thiraux

EDUCATION

Ph.D. Materials Science and Engineering *May 2023*
University of California, **Irvine**
M.S. Materials Science and Engineering *2013*
Ecole nationale supérieure de Physique, Electronique et Matériaux de Grenoble
B.S. Materials Science and Engineering *2010*
Ecole nationale supérieure de Physique, Electronique et Matériaux de Grenoble

EXPERIENCE

University of California Irvine
Graduate Researcher *Sep 2017 – May 2023*

- **Project 1:** Investigation of the mechanical response of ceramic and ceramic matrix composite architected materials printed using Direct Ink Writing (DIW).
  - Developed a custom Direct Ink Writing printer. Set up the entire lab for manufacturing ceramic parts using DIW in the Valdevit's group.
  - Developed, characterized the rheology of the ceramic slurries.
  - Optimized the printing parameters, printed 2D architected materials, and woodpile structures.
  - Characterized the samples using SEM, Computed Tomography, and optical microscopy.
  - Evaluated the architected materials mechanically (compression and 3-point bending) and analyzed the data.
  - Achieved high level of strength for ceramic architected materials at a fraction of the density.
- **Project 2:** Investigation of bio printed scaffolds using Direct Ink Writing for cartilage engineering.
  - Designed a bio ink which can be printable and suitable for co-culture.
  - Investigation of the design of the printed scaffolds and the chemical composition of ink onto the survivability of MSC stem cells.
  - Manufactured scaffold of an ear for cartilage engineering. Created an ink and scaffold suitable for the survivability of the cells and the development of collagen.

University of California San Diego
Visiting Student *Jun 2016 – Jun 2017*

- Studied the molecular dynamics of fatty acid monolayers on aqueous solutions.
- Set up of several systems to analyze the behavior of the different monolayers.
- Researched of the parameters needed for the simulations and looking for previous work on the subject in the literatures.
- Developed codes to study the chemistry of the system.
- Developed a procedure to generalize the study of the system.

PROMAN
Program Design Engineer *Nov 2013 – Jun 2014*

- Developed, tested, and supervised implementation of income statement program.
- Designed the program to utilize accounting software to automatically report data, save report, and push out data to every Proman agency.
- Analyzed the needs of different operators (accountants, salespersons). Managed the project.
- Performed tests to verify the validity of the program.
- Trained employees to efficiently utilize the program, authored training manual, and provided technical support for the Program.

Astrium Space Transportation, EADS
Materials Engineer *Mar 2012 – Aug 2012*

- Studied the filament winding process for composite materials used in aerospace.
- Corrected and validated a numerical model employing Fortran. Established a numerical model on COMSOL Multiphysics (Element Finite Analysis).
- Planned and implemented experiments, acting as a liaison between R&D and experimental team.
- Analyzed the correlation between the models and the experiment in order to understand the material behavior and to optimize the filament winding process.

3S-R Laboratory
Research Assistant *May 2011 – Jul 2011*

- Investigated the strain micro-mechanism of fibrous materials during the Resin Transfer Molding process.
- Prepared the samples, calibrated the sensors and mechanical devices, and characterized using X-ray tomography in situ mechanical testing.
- Designed and conducted a flexion test with fibers.
- Ran experiments to observe the reorientation and movement of fibers during resin impregnation both in the lab and at the Synchrotron of Grenoble.
- Analyzed data with Matlab code to comprehend the strain of fibers.

TEACHING ASSISTANCE EXPERIENCE

Teaching Assistant with Dr. Lorenzo Valdevit *09/2022-12/2022*
09/2022-12/2022

- Lead discussion sections on materials selection and introduction to materials science.
- Held office hours and graded exams and homework assignments.

Teaching Assistant with Dr. Daniel Mumm *03/2022-06/2022*

- Held office hours and graded exams and homework assignments.

PUBLICATIONS

Journal Papers

J1 **Thiraux, R.**, Dupuy, A. D., Ainger, K. M., & Valdevit, L. (2023). A high-throughput process for mechanical characterization of ceramic materials produced by Direct Ink Writing. *Open Ceramics*, submitted.

J2 **Thiraux, R.**, Dupuy, A. D., Lei, T., Rupert, T. J., Mohraz, A., & Valdevit, L. (2022). Damage tolerance in additively manufactured ceramic architected materials. *Journal of the European Ceramic Society*, *42*(13), 5893–5903.

J3 Reddy, S. K., **Thiraux, R.**, Wellen Rudd, B. A., Lin, L., Adel, T., Joutsuka, T., … Paesani, F. (2018). Bulk Contributions Modulate the Sum-Frequency Generation Spectra of Water on Model Sea-Spray Aerosols. *Chem*, *4*(7), 1629–1644.

J4 Adams, E. M., Wellen, B. A., **Thiraux, R.**, Reddy, S. K., Vidalis, A. S., Paesani, F., & Allen, H. C. (2017). Sodium-carboxylate contact ion pair formation induces stabilization of palmitic acid monolayers at high pH. *Physical Chemistry Chemical Physics*, *19*(16), 10481–10490.

Presentations

P1 'A High-throughput Process for Mechanical Characterization of Ceramic Materials Produced by Direct Ink Writing', R. Thiraux et al., presentation at the 152nd TMS Annual Meeting & Exhibition, San Diego, CA, USA, 2023.

P2 'Topological toughness in additively manufactured ceramic architected materials', R. Thiraux et al., presentation at the 151st TMS Annual Meeting & Exhibition, Anaheim, CA, USA, 2022.

P3 'Direct Ink Writing of Ceramic Architected Materials', R. Thiraux et al., presentation at the 150th TMS Annual Meeting & Exhibition, Virtual, 2021.

ABSTRACT OF THE DISSERTATION

Direct Ink Writing of Architected Materials for Mechanical and Biological Applications

by

Raphael Pierre Thiraux

Doctor of Philosophy in Materials Science and Engineering

University of California, Irvine, 2023

Professor Lorenzo Valdevit, Chair

Architected materials are a novel class of materials consisting of a (generally) periodic repetition of a geometrically defined unit cell in three dimensions. As their properties are determined not only by the constituent solid, but also (and predominantly) by the architecture (i.e., the unit cell topology), architected materials can achieve combinations of properties not reachable with conventional monolithic materials.

The complex topologies of architected materials almost inevitably require fabrication by novel additive manufacturing (AM) processes, and nearly any class of AM technologies has been used to demonstrate architected materials with superior combinations of properties. Among all AM technologies, Direct Ink Writing (DIW), a unique class of Material Extrusion (ME), is particularly interesting for its simple implementation and almost unlimited materials palette. In this process, a rheologically optimized complex liquid is extruded along a defined path, building the architected material layer by layer.

In this thesis, we designed and assembled a custom DIW system and employed it to address three important scientific questions: (i) Can we design and fabricate ceramic architected materials that exploit the architecture to control crack propagation and achieve higher strength than the monolithic solid at a fraction of its density? (ii) Can we develop a high-throughput approach to quickly characterize the distribution in mechanical properties of multiple ceramic materials, thus

dramatically accelerating new material design? (iii) Can we demonstrate a framework for the fabrication of architected materials that serve as scaffold for the growth of biological tissue, with special application to the development of cartilage from stem cells?

Collectively, these studies expand the development of Direct Ink Writing as a versatile approach for the fabrication of a wide range of materials for structural and biological applications.

1. Introduction

Architected materials are a class of materials consisting of periodic repetition of a topologically optimized unit cell in three dimensions; their defining characteristic is that their effective mechanical and physical properties are primarily defined by the unit cell topology, rather than solely by the properties of the constituent material(s). When properly designed, architected materials can access combinations of properties (mechanical, acoustic, thermal, …) which cannot be achieved with existing monolithic materials (whether natural or man-made)[1]. Mechanical metamaterials (i.e., architected materials optimized for unique combination of mechanical properties) have demonstrated exceptionally high stiffness and strength at low relative density. If ideal topologies (e.g., plate lattices with cube-octet symmetry[2]) are adopted, these materials can achieve ideal mechanical efficiency (defined as specific stiffness and strength meeting the Hashin-Shtrikman[3] and Suquet[4] upper bounds, respectively). As the effective properties of architected materials are affected by both unit cell topology and constituent material properties, combining these optimal topologies with exceptionally stiff and strong constituent materials has the potential of achieving unprecedented mechanical properties at low density[2,5,6]. One way of optimizing the strength of the constituent material is to architect it at the nanoscale, whereby metals would benefit from grain size reduction according to the Hall-Petch equation [7], and ceramics would benefit from the absence of sufficiently long cracks to induce premature brittle failure. While these concepts have all been demonstrated at the laboratory scale, the ability to routinely process nano-architected materials with complex topologies in a scalable manner is currently lacking.

The topological complexity of architected materials almost requires fabrication by additive manufacturing (AM). Among the plethora of available AM processes, Direct Ink Writing (DIW) – a sub-class of material extrusion (ME) consisting of layer-by-layer deposition of a rheologically

optimized ink according to a 2D pattern, offers an intriguing combination of properties, including resolution at the hundreds of microns scale, ability to print components at virtually any overall size at very high speed, and most importantly an extremely versatile materials palette [8]. For these reasons, DIW is particularly suited for AM of ceramic materials[9–15]: a polymeric ink with proper rheological characteristics can be synthesized and heavily loaded with virtually any ceramic powder, allowing AM of a ceramic slurry. Upon subsequent heat treatment, the polymer is removed, and the ceramic sintered. When architected materials are printed with line diameters of the order of a few hundred microns, sintering to full densification is readily achieved.

While printing very complex architected materials topologies by DIW is possible, it requires careful optimization of the printing strategy, which is beyond the scope of this work[8,16]. In this thesis, we focus on woodpile structures, simple topologies which are uniquely suitable to DIW. Woodpile structures are truss-based architected materials (lattices) fabricated via layer-by-layer deposition of lines in 0/90-degree patterns. Even though woodpile structures are not the most mechanically efficient lattices, they are easily fabricated with virtually any additive manufacturing approach and can be easily implemented in many applications. Woodpile structures can also easily be used as building blocks for fabrication of complex shape objects with carefully controlled internal porosity.

While the characteristics of DIW make it an ideal process for printing of ceramic structures, the polymeric nature of the inks open enormous opportunities for fabrication of soft structures for biological applications, where objects of complex shape can be fabricated with highly tunable multi-scale internal porosity, offering ideal bio-chemo-mechanical environments for the growth of living cells.

In this thesis, I investigate the design, fabrication, and mechanical characterization of woodpile structures made of hard ceramic and soft polymeric materials for structural and biomedical applications, respectively.

This thesis is structured as follows. After an introduction and literature review (chapter 2), chapter 3 investigates the failure mechanism of ceramic woodpile structures under uniaxial compression. An alumina ink is developed, with rheology tuned to enable the printing of tall structures and long overhanging lines. A simple analytical model is implemented to investigate the flow of the ink inside the nozzle. The model and the experimental measurements are compared and used to determine sets of optimal printing parameters (pressure, tabletop speed), which are used to print woodpile structures with remarkable fine features. As the strength of ceramics is extremely sensitive to the size and distribution of their pre-existing flaws, the design of woodpile structures with microscale line dimensions can result in greatly improved mechanical properties compared to fully dense samples manufactured under the same conditions. Indeed, several types of flaws are identified in fully dense parts, which are not present in woodpile structures. Mechanical tests are conducted to relate these differences to mechanical behavior and understand the impact of woodpile topology/geometry on strength and robustness.

The mechanical behavior of the architected material can be further improved by reinforcing or doping the constituent ceramic, thus resulting in an architected complex ceramic system. Unfortunately, mechanical characterization of novel ceramic materials is a time-consuming operation, as the statistical nature of strength in brittle materials implies that a large number of specimens must be tested to extract reliable distribution parameters. In chapter 4, we propose a novel high-throughput testing procedure that allows extraction of statistical information on the strength of ceramic materials. We process large numbers of small-scale bending specimens from

low volumes of material via Direct Ink Writing followed by sintering, and rapidly characterize them mechanically to extract Weibull parameters for the bending strength. We demonstrate the power of this method by (i) characterizing five different ceramics, (ii) investigating the nature of multi-scale defects introduced by the DIW process and their effect on the strength distribution of macroscopic components, and (iii) designing and demonstrating architected structures with bending strength 50% larger than monolithic materials at 20% lower weight. While the results are presented on alumina-based ceramics in the context of DIW, the method proposed herein is general and can provide rapid statistical data on the strength of virtually any ceramic material, for application to any processing technology.

Finally, chapter 5 provides an example of the importance of micro-architected materials (including woodpile structures) for medical applications. Microtia is a congenital condition including diverse malformations of the external ear. Traditional plastic surgery procedures to correct this problem rely on extracting cartilage from a rib of the patient, an approach that is clearly invasive, painful and prone to infections. An alternative – and far less invasive – approach would consist of scanning the existing ear of the patient, printing a mirrored ear with an ink suitable for cell growth with carefully introduced internal porosity, and subsequently grow cartilage via stem cell-based approaches. In collaboration with Prof. Widgerow in the School of Medicine, here we develop/optimize a suitable ink which serves as a carrier for the biological constituent and demonstrate fabrication of a full ear by Direct Ink Writing, with internal porosity in the 200 μm range.

2. Background

2.1 Architected materials

2.1.1 Definitions and properties

Architected materials are a class of materials in which the properties are not only defined by the constituent, but also (and mostly) by the unit cell topology. The design of complex topologies can result in the achievement of new and unique functionalities, from negative Poisson's ratio[17,18] (auxetic response) to negative coefficient of thermal expansion (CTE)[19,20], functionally graded properties[21], tuning of acoustic and elastic wave propagation[22,23], and ultralight lattices which can recover from 50% strain[24,25]. These are all features which are topology-dependent and cannot be achieved in conventional solid materials.

The design of lightweight monolithic materials is limited by the mechanical and physical properties of the constituent material, with strong materials typically exhibiting high mass density. Architected materials based on lattice topologies have the ability to decouple strength and density to a large degree and enable unprecedented combinations of those properties. Lattice materials are generally composed of truss or plate features connected at nodes, thus forming a unit cell which is repeated in different directions to generate the architected material at virtually any dimensional scale. Classic examples are 2D lattices extruded in the out-of-plane direction (e.g., Kagome, triangular, honeycomb topologies) and fully 3D lattices, as shown in Figure 2.1a, b, c, and d, respectively.

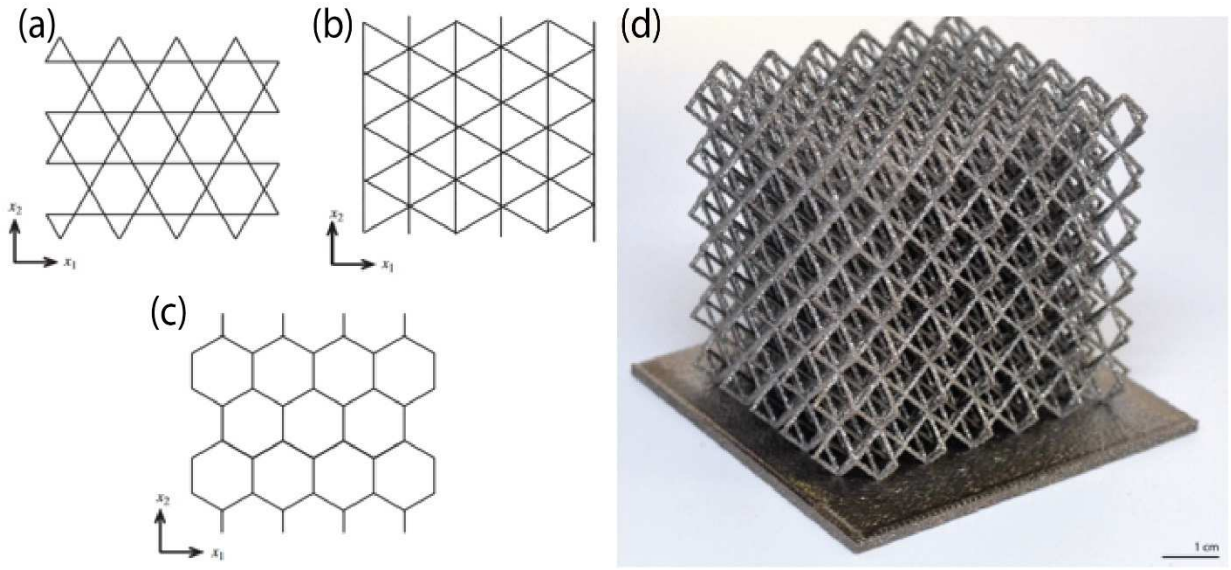

Figure 2.1. *(a) Kagome lattice, (b) triangular lattice, (c) hexagonal lattice*[26] *and (d) octet lattice (by CalRAM, Inc., for HRL, LLC).*

For a given topology, the relative density of lattices ($\bar{\rho}$), defined as the volume fraction of the solid constituent, is only dependent on the thickness (t) and the length (l) of the bar:

$$\bar{\rho} = A\left(\frac{t}{l}\right)^{a} \qquad \textbf{Eq. 1}$$

For 2D lattices, $a=1$. For 3D lattices characterized by open and close-cell unit cell architectures, $a=2$ and $a=1$, respectively. Effective mechanical properties of lattice materials, such as Young's modulus, E, and strength, σ_c, generally scale with the relative density as[26]:

$$\frac{E}{E_S} = B\bar{\rho}^{b} \qquad \textbf{Eq. 2}$$

$$\frac{\sigma_c}{\sigma_{TS}} = C\bar{\rho}^{c} \qquad \textbf{Eq. 3}$$

with E_s and σ_{TS} representing the Young's modulus and the strength of the constituent solid material, respectively; and A, B, C, a, b, and c are topology-dependent non-dimensional coefficients. The power-law exponents for the strength and the Young's modulus depend on whether the lattice is stretching or bending dominated: in the former, external loading is transferred to the individual bars in such a way that each bars primarily deforms axially, whereas in the latter,

bending deformation of the bars is the dominant local deformation mechanism. For stretching-dominated topologies (e.g., Kagome and triangular 2D lattices and 3D octet lattices), $b=c=1$, whereas for bending-dominated lattices, $b,c>1$ (for example, $b=2$ and $c=3$ for honeycomb 2D lattices). The important implication is that stretching-dominated architectures are stiffer and stronger than bending dominated ones, with the advantage growing as the relative density is reduced[27]. The study of those structures has allowed to reach high values of the mechanical properties at low density and to fill up the white space on the Ashby graph as shown in Figure 2.2.

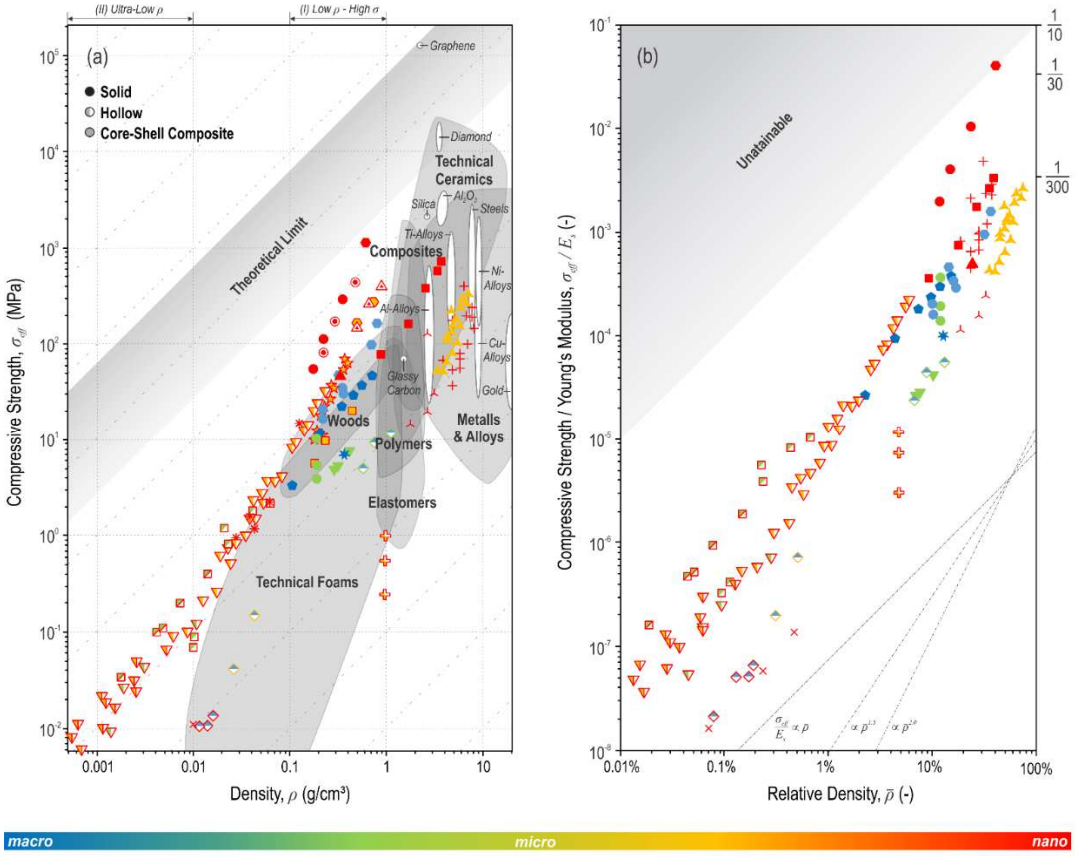

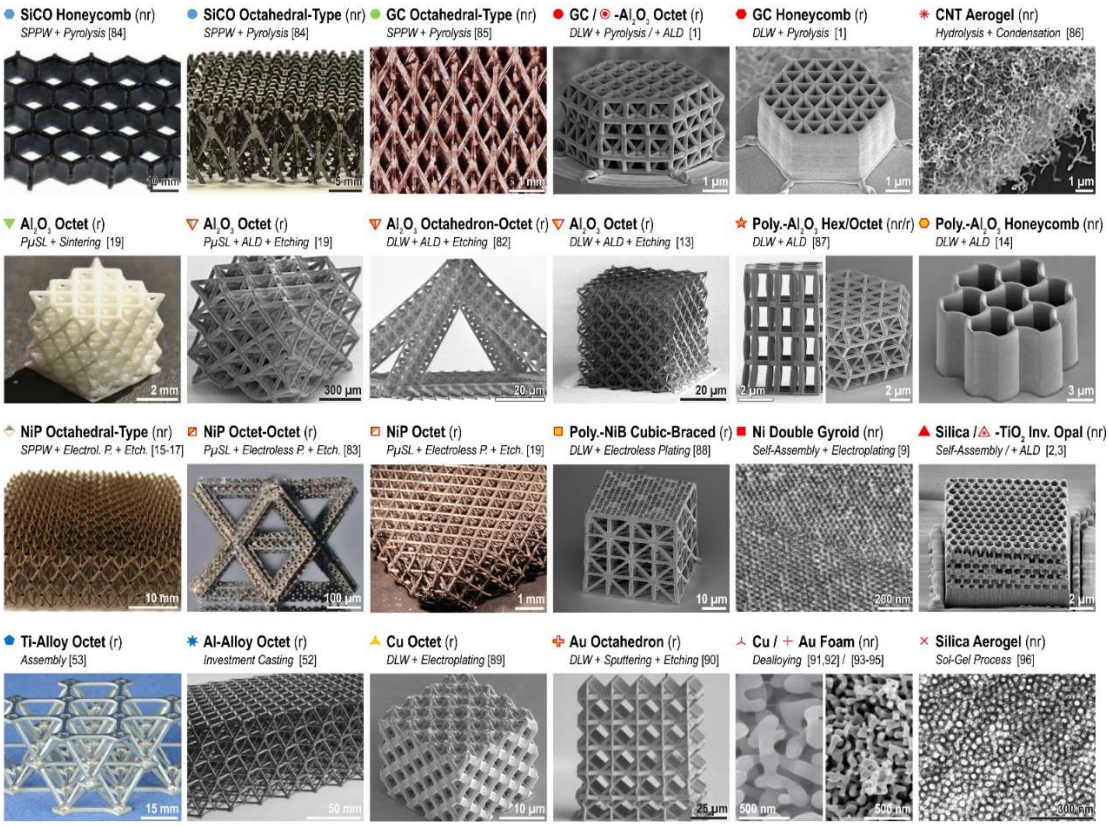

Figure 2.2. *Compressive strength–density materials property chart of different nano-, micro-, and macrolattices as well as stochastic nanoporous and commercial bulk materials. Symbol shapes relate to the constituent material, symbol colors indicate the length scale of structuring (fillings = feature diameter, lines = shell thickness, if any). a) Absolute strength vs. density plot showing that many nanolattices reach far into the low-ρ-high-σ, or the ultralow- "white space". b) Strength normalized by Young's modulus vs. relative density plot, showing that nanolattice materials are capable of exploiting material strengths up to the theoretical limit (E_s/10), whereas the bulk material strengths are often on the order of E_s/300 . For all structures the rigidity of the topology (r = rigid, nr = non-rigid) as well as a brief description of the applied fabrication process is given*[28].

The fracture toughness (K_{IC}) of elastic brittle, isotropic lattices follow a similar trend as stiffness and strength:[29]

$$\frac{K_{IC}}{\sigma_{TS}\sqrt{l}} = D\bar{\rho}^{d} \qquad \textbf{Eq. 4}$$

where σ_{TS} is the tensile strength of the solid constituent material, l is the unit cell size, and D and d are topology-dependent coefficients. For 2D lattices, d can vary from 0.5 for the Kagome structure to 2 for the honeycomb structure, as shown in Figure 2.3. Notice that the fracture

toughness of lattice materials scales with the square root of the unit cell size. The important implication is that lattices become more brittle as their unit cell size is reduced.

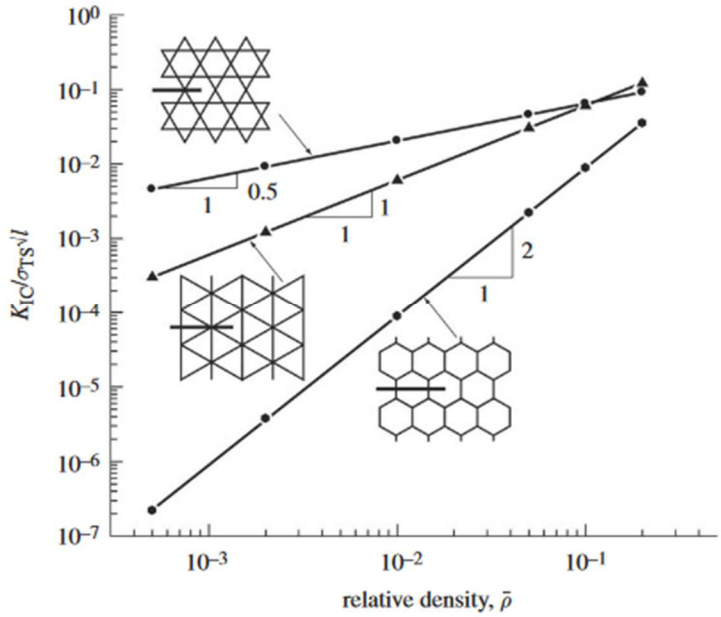

Figure 2.3. *The predicted mode I fracture toughness K_{IC} plotted as a function of relative density $\bar{\rho} \propto {}^{t}/_{l}$, for the three isotropic lattices: hexagonal, triangular and Kagome*[26].

While the scaling laws for stiffness and strength discussed above are scale-independent, size effects on the constituent material properties can introduce remarkable length scale dependence. In particular, the strength of solid constituents can be significantly increased when the dimension of the object is reduced to the nanoscale. For metals, the key phenomenon is the corresponding reduction of the grain size, which reduces the mobility of dislocation and results in significant increase in the yield strength, according to the Hall-Petch law[7]. In ceramics, reduction of the component size below the dimension of the average internal defect may result in control of the defect size. Even tough ceramics possesses exceptional theoretical mechanical properties, actual properties are severely limited by the presence of internal defects (pores, cracks…). Their fracture strength is directly related to the size of the largest crack, because of the inability of ceramics to

reduce stress concentration via plastic deformation. According to Griffith's law[30], the fracture strength (σ_f) scales with the maximum crack size (a) as:

$$\sigma_f \sim \frac{K_c}{\sqrt{a}} \quad \textbf{Eq. 5}$$

The manufacturing of ceramic lattices with feature size at the micro/nanoscale allows controlling the largest crack size, as it cannot exceed the thickness of the truss (t). Below a critical truss thickness, the crack size becomes roughly equivalent to size of the bar, resulting in the scaling:

$$\sigma_f \sim \frac{1}{\sqrt{t}} \quad \textbf{Eq. 6}$$

The fracture strength will thus increase with the decrease of the truss thickness, up to a critical thickness where the fracture strength reaches a theoretical value, of the order of *E/10*, with σ_f the Young's modulus of the material. As for most ceramics, e~200 GPa, theoretical strengths are often 1-2 orders of magnitude larger than strength measured on macro-scale samples. Producing lattices with feature sized below this critical level and sufficient number of unit cells to achieve the desired macroscopic dimensions provides an exciting avenue to take advantage of these size effects in large-scale materials for structural applications. This theorical value is often reached when the largest feature size is about 100 nm. Fabrication techniques based on two-photon polymerization Direct Laser Writing (2pp-DLW) followed by pyrolysis enable demonstration of this phenomenon [2,25,31,32]. Combining this approach with interesting plate-based topologies that are optimally stiff and strong, C. Crook *et al.*[2] have demonstrated carbon-based cubic-octet plate nanolattices with the highest specific strength ever reported for any material (Fig. 2.4). Unfortunately, these incredible properties achieved at the nanoscale are extremely difficult to scale up, as 2pp-DLW is an inherently unscalable technology.

Direct Ink Writing is a far more scalable technology than 2pp-DLW, enabling fabrication of centimeter-scale specimens in a matter of minutes. While the minimum feature size (~100 microns) is far larger than needed to achieve theoretical density, this technology might provide an exceptional compromise between mechanical performance and scalability. This compromise will be investigated in this thesis.

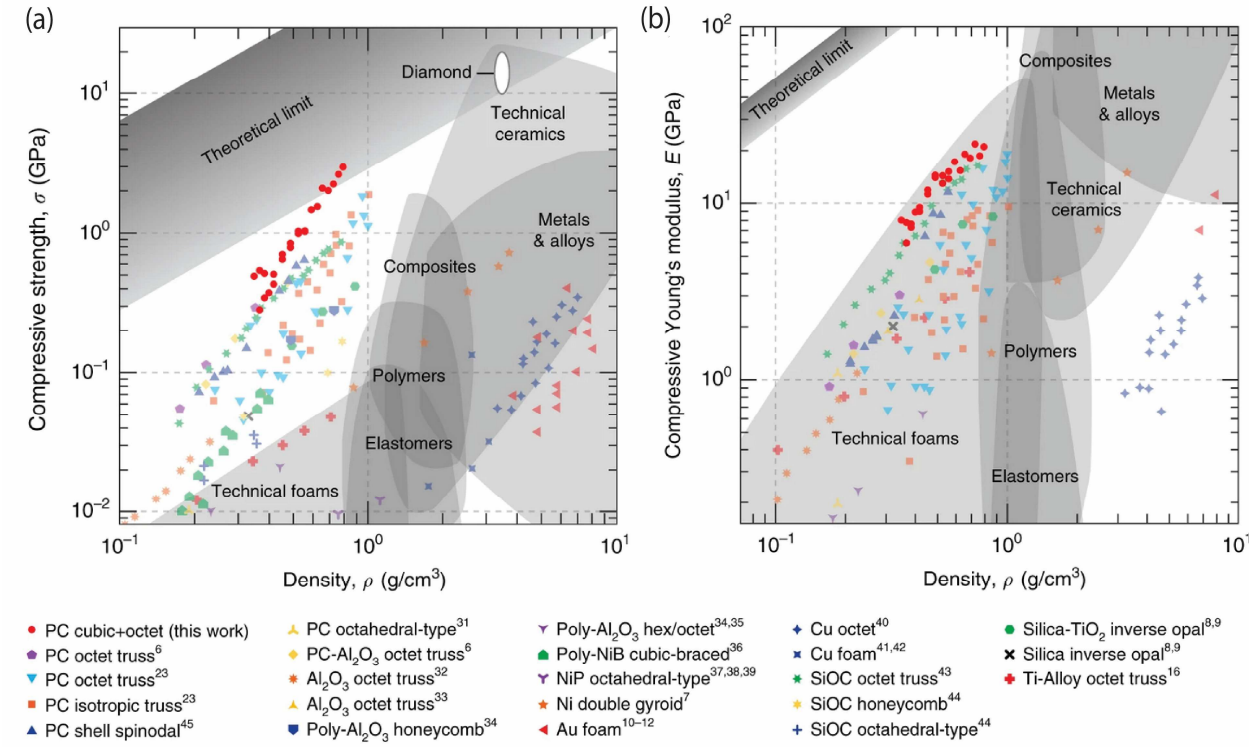

Figure 2.4. *Pyrolytic carbon (PC) cubic+octet plate-nanolattices are the strongest and the stiffest existing materials for their respective densities. Compressive strength (a) and stiffness (b) Ashby maps. The stronger and weaker theoretical limits assume an arbitrary ideal topology with the best possible scaling of one, for two different constituent materials: graphene, the strongest known material at any scale, and diamond, the strongest known bulk material at the macroscale. With up to 639 and 522% average strength and stiffness improvements compared to the most efficient beam-nanolattices, cubic+octet plate nanolattices are the only architected materials to surpass the bulk theoretical strength limit and to reach specific stiffnesses comparable to those of the best performing technical foams*[2].

2.1.2 Common manufacturing approaches for architected materials

The topological complexity of architected materials almost always requires additive manufacturing (AM) technologies for fabrication. AM is a broad class of fabrication approaches, traditionally encompassing 7 different processing techniques: Extrusion, Vat Photo-polymerization, Powder Bed Fusion, Binder Jetting, Material Jetting, Sheet Lamination and Direct Energy Deposition. Each technique is further divided in sub-classes, as shown in Figure 2.5. Among the myriad of additive manufacturing techniques, Direct Ink Writing (DIW), which is classified as a material extrusion base technique, has a lot of potential for the manufacturing of architected materials in the scope of this research.

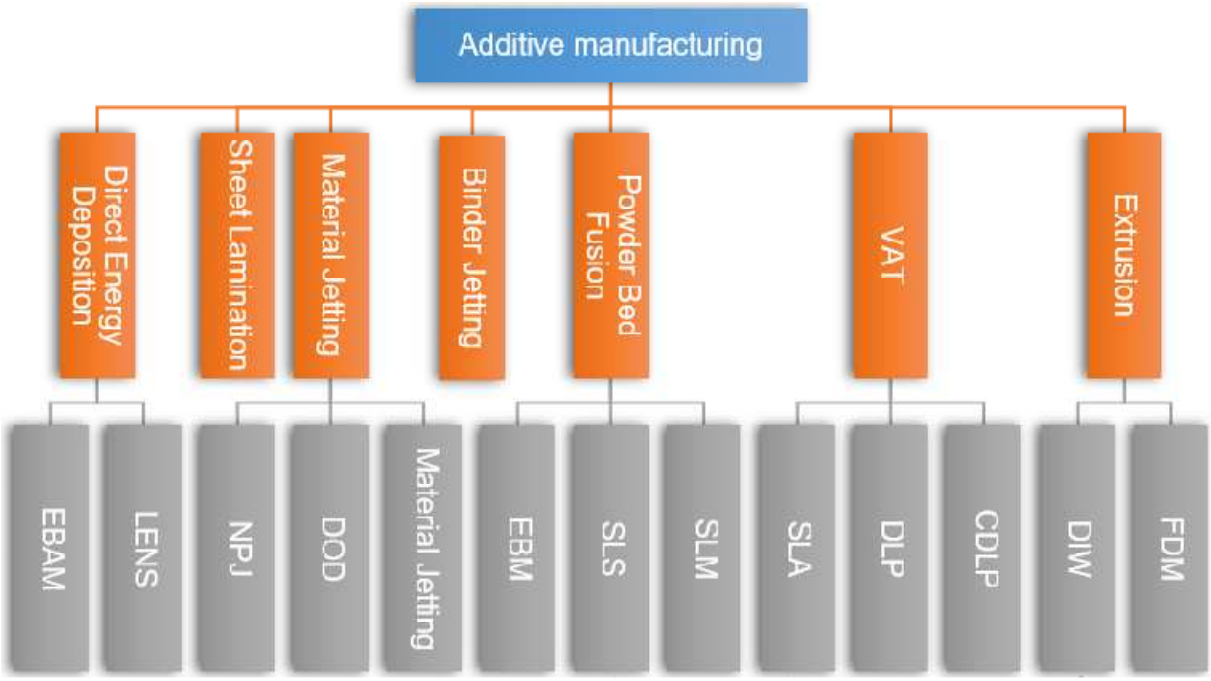

Figure 2.5. *Exhaustive list of additive manufacturing technologies.*

Direct Ink writing consists of the extrusion of a complex fluid (the ink) from a nozzle (with diameter in the sub-millimeter to micron range), combined with the motion of the substrate along three degrees of freedom, allowing layer-by-layer fabrication of complex structures. The technique was first introduced by J. Cesarano[33] in 1999. While not as mature as other AM approaches, DIW

has received significant attention over the past few years, largely thanks to its small-scale printing capabilities combined with a very extensive materials palette: inks can be developed to print metals[8], polymers, ceramics[11,34], and composites[35,36]. Figure 2.6 shows an exhaustive list of materials which can be printed using DIW, alongside the minimum feature size for each material.

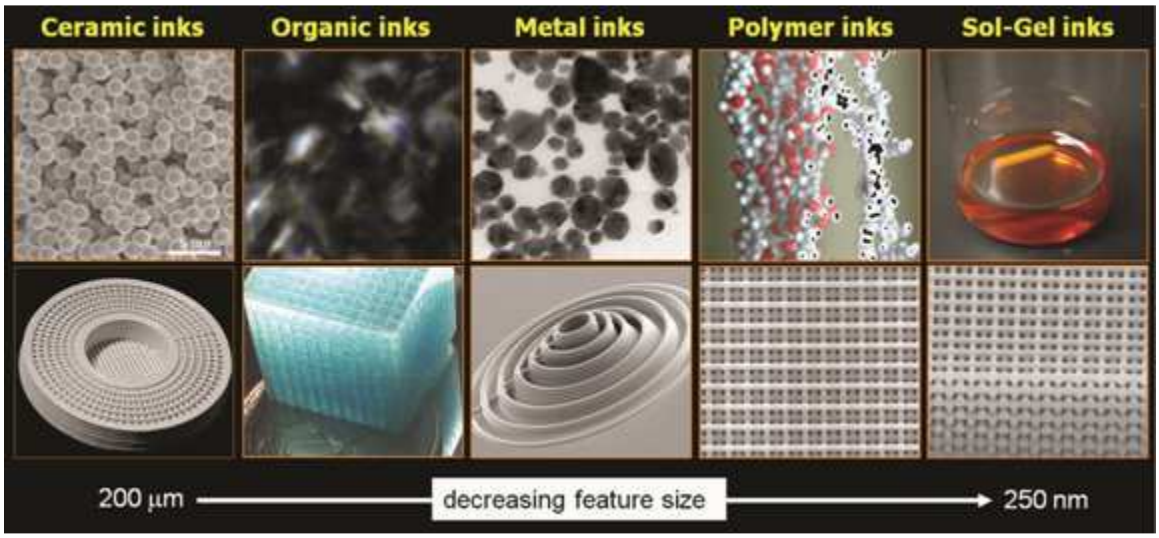

Figure 2.6. *Example of materials printable with DIW and the minimum feature size achievable for each*[37].

Achieving good print quality in DIW requires careful control of the rheology of the ink. A rheological behavior including the existence of a yield stress and a shear thinning response upon flowing are generally required (a so-called Herschel Buckley behavior). When pressure is applied on the ink inside the syringe, the static yield stress of the ink is overcome, and the ink starts flowing through the nozzle[11,34]. After deposition, the ink will relax until the stresses induced by gravity drop below the dynamic yield stress of the ink. The success of a print using DIW strongly depends on the rheology of the ink. Five rheological behaviors exist to describe the flow of the ink: (a) Newtonian, (b) shear-thinning, (c) shear-thickening, (d) Bigham plastic and (e) shear thinning with a yield stress, each of which is characterized by a different stress/strain rate curve, as shown in Figure 2.7. While having a Bingham plastic behavior (Newtonian fluid with a yield stress) is in

principle feasible, a shear thinning behavior allows an easier flow through the nozzle, with lower pressure requirements. The presence of the yield stress has two main purposes: first, it compensates. the force of gravity and prevents the ink from flowing under its own weight; second, it helps maintaining the shape of line after deposition.

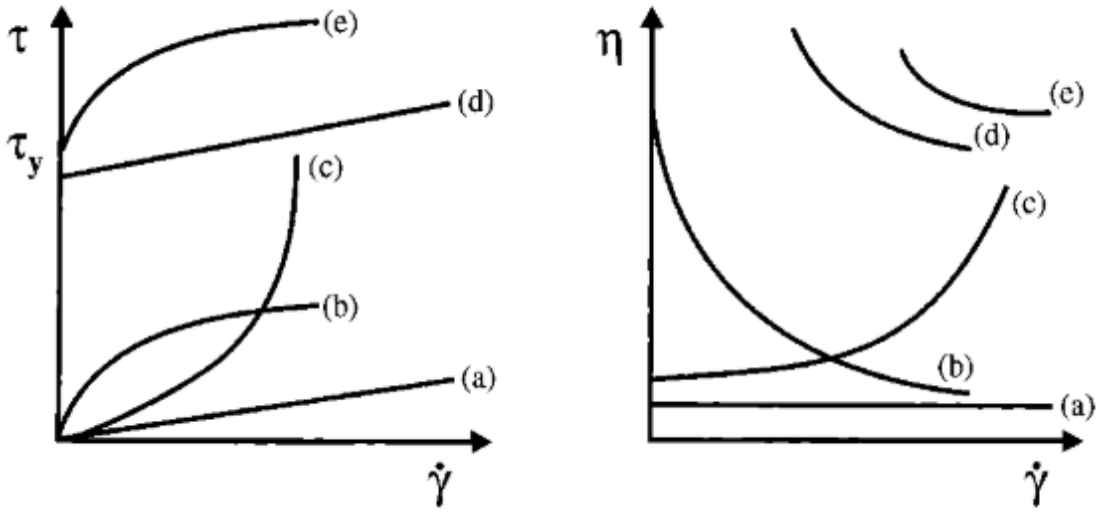

Figure 2.7. *Types of rheological behavior exhibited by colloidal dispersions: (a) Newtonian flow; (b) shear thinning; (c) shear thickening; (d) Bingham plastic; and (e) shear thinning with a yield stress*[38].

The main limitations of DIW are the need for support material for nearly any 3D structures and the inability to stop and start the flow of ink at will during the print, something that is routinely done in its lower-tech brother, Fused Deposition Modeling (FDM). Several groups have tried to overcome this limitation, as summarized in Figure 2.8. J.Lewis *et al.*[8,16] have demonstrated two approaches for printing 3D structures via DIW: (i) designing an ink which can be curable with a laser while printing, and (ii) printing inside a visco-elastic gel. In a different approach, S. Z. Guo *et al.*[39] have used fast drying solvent in the ink, which rapidly increase the ink viscosity while printing, providing structural integrity to the ink: as a result, they were able to print unsupported springs.

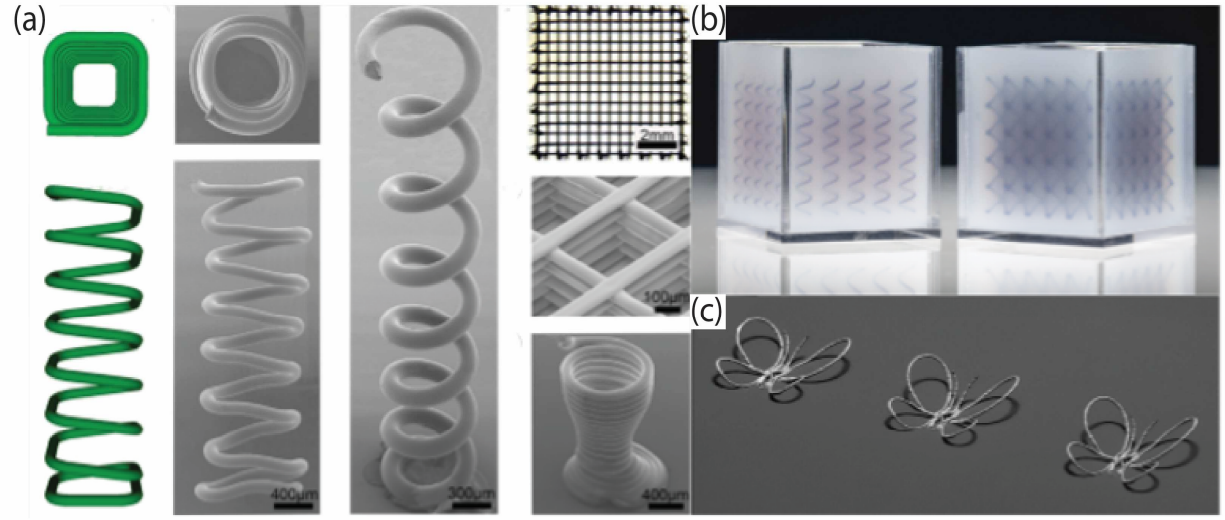

Figure 2.8. *Examples of techniques to overcome geometric DIW limitations. (a) solvent evaporation direct ink writing*[39]*. (b) direct ink writing inside a visco-elastic gel*[16]*. (c) Laser assisted direct ink writing*[8]*.*

2.2 Colloidal suspensions

2.2.1 Definition

As discussed in the previous section, the ability to control the rheological properties of the ink is essential for printability. This section discusses the physics that is responsible for the appropriate ink rheology. Inks containing nanoparticles (as those discussed in this work) can be characterized as colloidal suspensions. A colloid is defined as the dispersion of a discrete phase in continuum medium. Both the discrete and the continuum phases can be solid, liquid or gaseous. For example, we can have liquid, solid particles or gases dispersed in liquid or solid medium; or liquid and/or solid particles dispersed in gases, also known as aerosols, smoke or fog. For Direct Ink Writing of ceramics or CMCs, we will focus on solid particles dispersed in a liquid medium. The particles are in the nanometer to micrometer size range; they need to be larger than the molecules of the medium to support the continuum assumption, and small enough for their motion to be affected by the movement of the molecule of the medium.

2.2.2 Interparticle interactions in a colloidal system

The interparticle forces play a crucial role in determining the rheology of ink. The total potential is the sum of 4 terms, as shown in the following expression[38,40]:

$$V_{tot} = V_{vdW} + V_{elect} + V_{steric} + V_{structural} \quad \textbf{Eq. 7}$$

These potentials are illustrated in Figure 2.9. $V_{vdW}$is the van der Waals potential, which is long range (Figure 2.9a). This potential is always attractive and present. The potential shows a power law dependence on the particle-particle distance, and can be expressed as[38]:

$$V_{vdW} = -\frac{A}{6}\left(\frac{2}{s^2-4} + \frac{2}{s^2} + \ln\frac{s^2-4}{s^2}\right) \quad \textbf{Eq. 8}$$

where $s = \frac{2a+h}{a}$, with h the minimum separation between the particle surfaces, a the particle radius and A the Hamaker constant. This attractive potential will decay over distances of nanometers. Driven by this potential, the particles will tend to agglomerate and create aggregates which will not be able to stay in suspension. To create stability in the suspension, the van der Waals forces must be balanced. Therefore, the other potentials are important. V_{elect} is the electrostatic potential (Figure 2.9c). The electrostatic force is repulsive, and the potential can be expressed as[38]:

$$V_{elect} = 2\pi\varepsilon_r\varepsilon_0 a\Psi_0^2 exp(-\kappa h) \quad \textbf{Eq. 9}$$

with ε_r, the dielectric constant of the solvent, ε_0 the permittivity of vacuum, Ψ_0 the surface potential and $1/\kappa$ is the Debye-Huckel screening length, given by[38]:

$$\kappa = \left(\frac{F^2\sum_i N_i z_i^2}{\varepsilon_r\varepsilon_0 kT}\right)^{1/2} \quad \textbf{Eq. 10}$$

with N_i the number density, z_i the valence of the counterions of type i, and F the Faraday constant. Ψ_0 derives from the dissociation of amphoteric hydroxyl groups present on oxide surfaces and depends on pH and indifferent electrolyte concentration. This potential is only given by analytical

approximations or numerical solutions, with all models assuming equal size spherical particles. This interaction occurs when the outside layer of the particle becomes charged. This layer will interact with the counterions present in the medium and form an electric double layer. The interplay of V_{vdW} and V_{elec} is studied by the DLVO theory (named after Derjaguin, Landau, Verwey and Overbeek), describing the electrostatic stabilization (Figure 2.9b). Close to the surface of the particle, there exists a first well, due to the dominance of the vdW force causing irreversible aggregates. Further away, we can see the formation of a second well, which will cause the flocculation of the colloidal suspension. The flocculation is a reversible process. The electrostatic forces create a maximum in the potential which allows stabilization of the colloidal suspension.

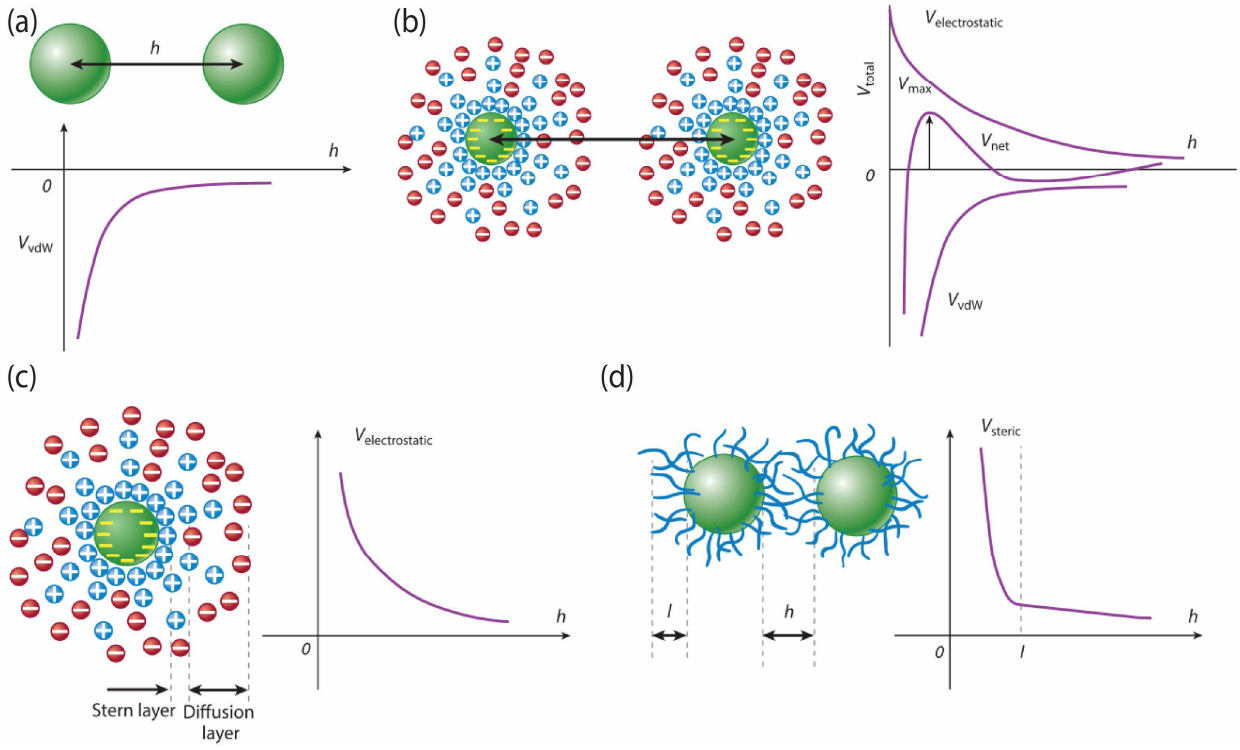

Figure 2.9. *Interparticle interaction in a colloidal system. (a) Van Der Waals potential. (b) combination of Van Der Waals and electrostatic potential. (c) Electrostatic potential and (d) steric potential*[40].

This stability of the suspension can be studied by looking at the zeta potential, which measures the electrostatic potential at or near the beginning of the diffusion of the double layer. As an example, Figure 2.10a shows the zeta potential of an alumina slurry for different amounts and molar weight of PVP. The zeta potential decreases with increasing the pH. The change of sign (in this case at pH 8.5) represents the isoelectric point (IEP). Colloids are unstable around the IEP due to the presence of positively and negatively charged particles. The Figure 2.10b shows the liquid-to-solid transition of a slurry by either increasing the salt concentration or increasing the pH towards the IEP.

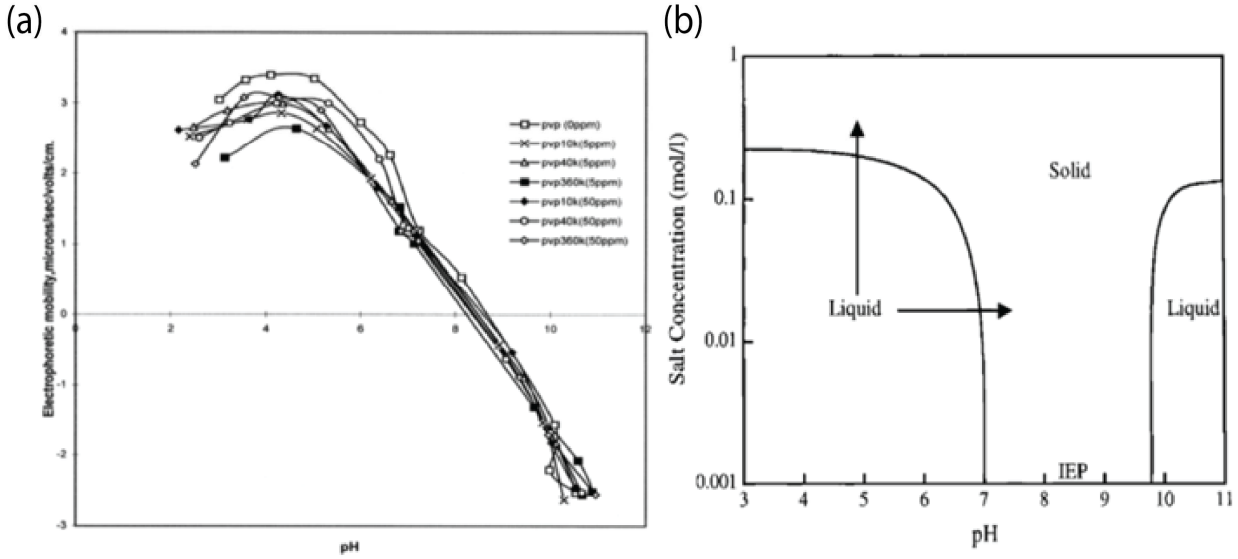

Figure 2.10. *(a) Influence of the amount of rheology modifier on the Zeta potential of an alumina slurry*[41]*. (b) transition liquid/solid depending on the pH and salt concentration for an alumina aqueous suspension*[38]*.*

Furthermore, the stabilization of the colloidal suspension can be tuned using the steric potential, V_{steric} , which is created by the absorption of polymers at the surface of the particles, as shown in Figure 2.9d. This potential will create repulsive forces between colloidal particles. The thickness of the layer δ plays an important role to overcome the vdW potential. The properties of the layer (coverage, adhesion, and conformation) depend on several factors such as on solvent

quality, molecular architecture, number of anchoring groups, active surface site density, and colloid and organic concentrations in solution. Different types of polymers can be used for steric stabilization such as homopolymers, diblock copolymers, comblike copolymers, and functionalized short-chain dispersants, as shown on Figure 2.11.

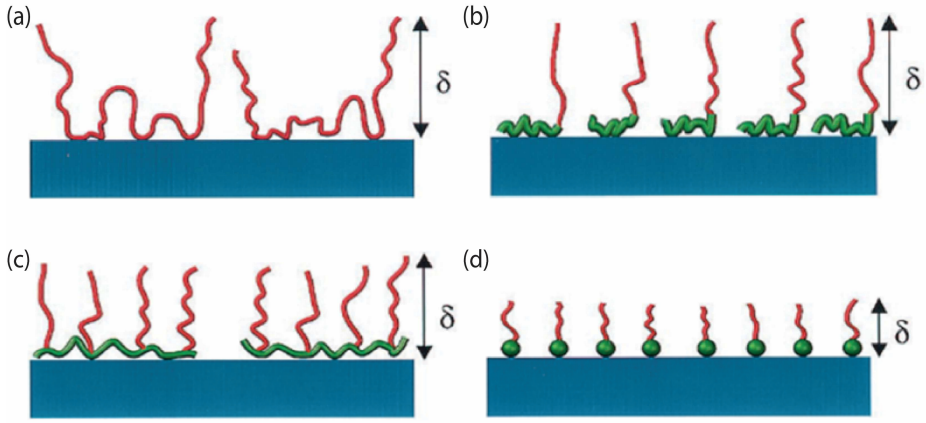

Figure 2.11. *Schematic illustrations of the adlayer conformation on an ideal ceramic surface as a function of varying the molecular architecture: (a) Homopolymer, consisting of tails, loops, and train configuration. (b) diblock copolymer, consisting of short anchor block and extended chain block. (c) Comblike copolymer, consisting of extended segments attached to anchored backbone; and (d) functional, short-chain dispersant, consisting of anchoring head group and extended tail*[38].

The interactions will be counted when the particles will be at a distance less than twice the adlayer thickness. This potential can be decomposed into two parts: the interpenetrational domain ($\delta < h < 2\delta$) and the interpenetrational plus compressional domain ($h < \delta$). While models exist that describe the potential for some materials, those models will not be discussed in here. It is possible to combine the electrostatic and steric interactions by using a polyelectrolyte. A polyelectrolyte can be any polymer cited earlier, but with one or more ionizable segments. Similarly, the layer thickness can be tailored with pH and ionic strength as shown in Figure 2.12. The more the polymer is ionized the more the thickness of the layer will increase to accommodate for the repulsion between the ionized groups. On the other hand, a low ionized polymer will produce a dense layer.

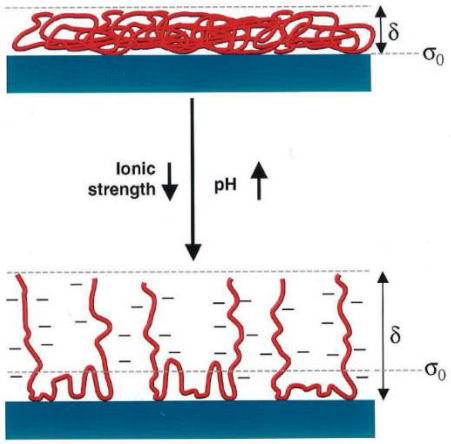

Figure 2.12. *Effect of the ionic strength and pH on the adlayer thickness of the polyelectrolyte*[38].

Different mechanisms occur depending on the amount of polyelectrolyte present at the surface for stabilization of the system: for a small amount, the flocculation by charge neutralization or bridging mechanisms are predominant whereas at higher amount, long-range repulsive forces between absorbed polymers are predominant. Finally, the last interaction in the colloidal system is the structural potential. This interaction is due to the presence of non-absorbed polymer in the system, as shown in Figure 2.13. The polymer particles are small compared to the colloidal particles. The interaction is due to a gradient of those small particles. The concentration is small when the primary particles are close to each other and is larger away in the solution. This interaction can provoke either flocculation or stabilization.

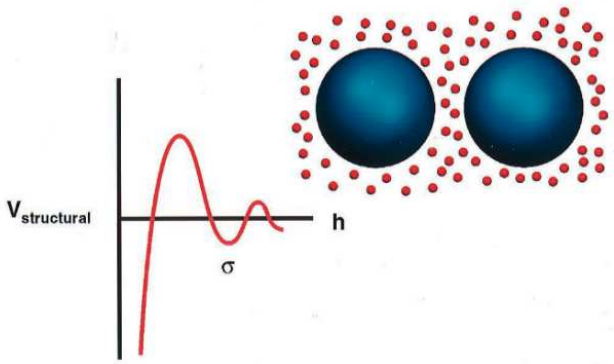

***Figure 2.13**. Schematic of the depletion potential*[38].

The distance between the surface of the particle to the bulk solution is called the depletion layer thickness and it is of the order of the small particle diameter ($2a_{dep}$). The depletion potential for an uncharged depletant species can be expressed as the following[38]:

$$V_{dep}(\lambda) = 0 \quad \text{for } h > 2a_{dep} \qquad \textbf{EQ.11}$$

$$V_{dep}(\lambda) = \frac{a\phi_{dep}^2 kT}{10a_{dep}}(12 - 45\lambda + 60\lambda^2 - 30\lambda^3 + 3\lambda^5) \qquad \text{for } 4a_{dep} > h \geq 2a_{dep} \qquad \textbf{EQ.12}$$

$$V_{dep}(\lambda) = -\frac{3a\phi_{dep}kT}{2a_{dep}} + \frac{a\phi_{dep}^2 kT}{10a_{dep}}(12 - 45\lambda + 60\lambda^2) \qquad \text{for } h < 2a_{dep} \qquad \textbf{EQ.13}$$

where ϕ_{dep} is the depletant volume fraction in solution and $\lambda = (h - 2a_{dep})/2a_{dep}$.

2.2.3 Rheology of colloidal suspensions

Several parameters can affect the rheology of the colloidal system. As shown in Figure 2.14, the viscosity increases with an increase of solid fraction of particles. At low solid fraction and up to 0.3, the increase is linear; above a solid fraction of about 0.6, the viscosity increases sharply. This evolution can be fitted using the two following expressions for a monodisperse system:

$$\eta = \eta_0(1 + 2.5\phi + 6.2\phi^2) \qquad \textbf{EQ. 14}$$

$$\eta = \eta_0\left(1 - \frac{\phi}{\phi_{max}}\right)^{-[\eta]\phi_{max}} \qquad \textbf{EQ. 15}$$

where η and η_0 are the viscosity of the colloidal system and of the pure medium, respectively, and ϕ and ϕ_{max} are the solid fraction and the maximum solid fraction in the system, respectively. For a system composed of perfectly spherical particles, ϕ_{max} is equal to 0.74, corresponding to a close packed structure. Usually, ϕ_{max} is closer to 0.64. The first equation above represents the viscosity at low solid fraction when the colloidal system still shows a close Newtonian behavior because there not enough particle to be able to interact with each other and influence the rheology. This equation was modified from Einstein's formulation by Batchelor[42]. The second equation comes from the model of Krieger & Dougherty[43], describing the viscosity at higher solid fraction.

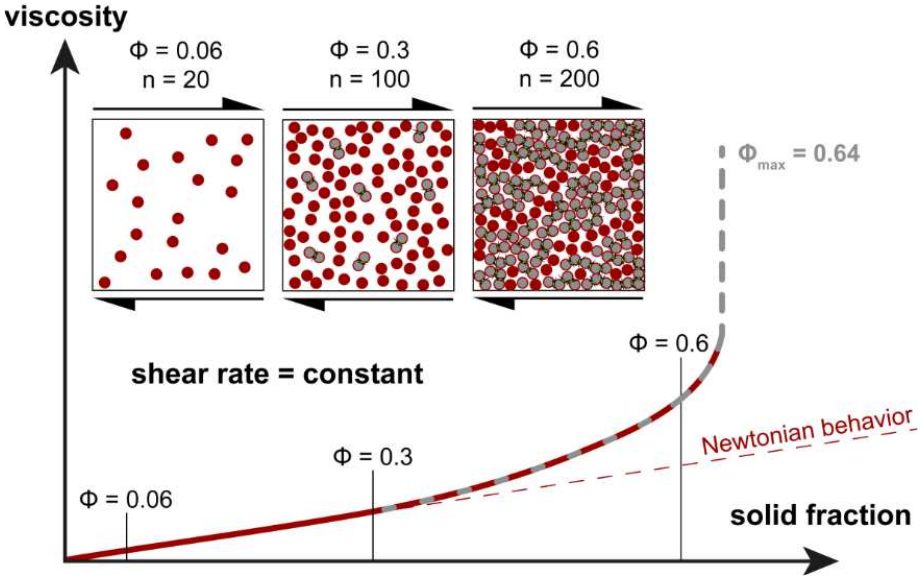

Figure 2.14. *Effect of the solid fraction on the viscosity for a monodisperse system with spherical particles (image from wiki ANTON PAAR website).*

In terms of behavior, at low solid fraction the system is shear-thinning (beyond the Newtonian behavior), whereas at high solid fraction (close to ϕ_{max}) the behavior is shear-thickening (Figure 2.15). The reason is that the interparticle interactions at low solid fraction are fewer and weaker, so the network breaks easily when a shear rate is applied. As the shear rate is increased, the particles can easily move and rearrange themselves along the flow. By contrast, at high solid

fraction, particles cannot easily move and rearrange themselves. Moreover, if the shear rate is high, the molecules of solvent will move fast compared to the colloids creating an area "free" of solvent molecules, thus rapidly increasing the viscosity (e.g., quicksand).

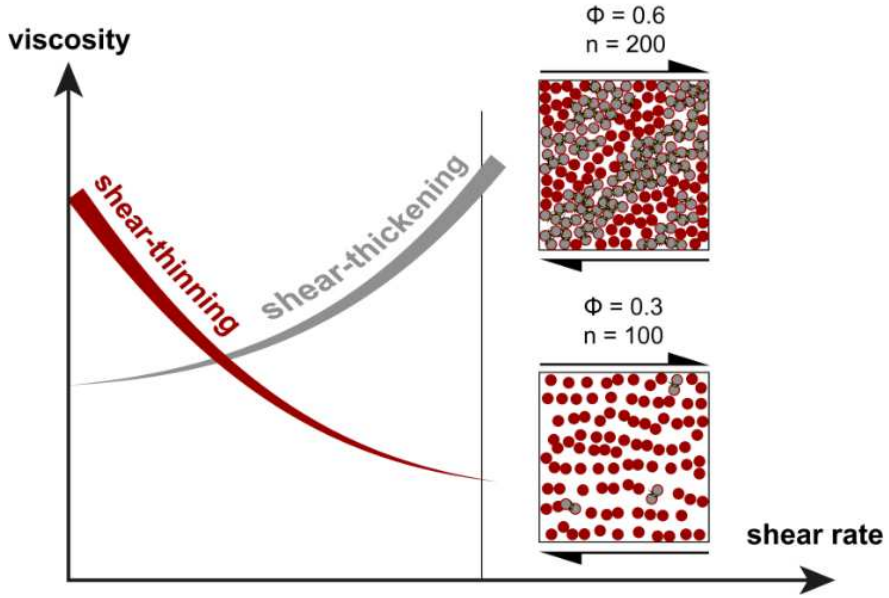

Figure 2.15. *The rheological behavior of the colloidal system for low and high solid fraction (image from wiki ANTON PAAR website).*

The size of the particles has also an effect on the viscosity of the colloidal system. As we said earlier, the viscosity depends on the solid fraction. However, for two systems with the same solid fraction but with different size of particles, the viscosity can be different as shown in Figure 2.16. We can see that at high shear rate when the particle is rearranged with respect of the flow, the particle size does not have any effect on the viscosity. There is an effect at low shear rate due to the higher number of particles which must rearrange with the flow creating a higher viscosity and higher shear thinning behavior for small particles.

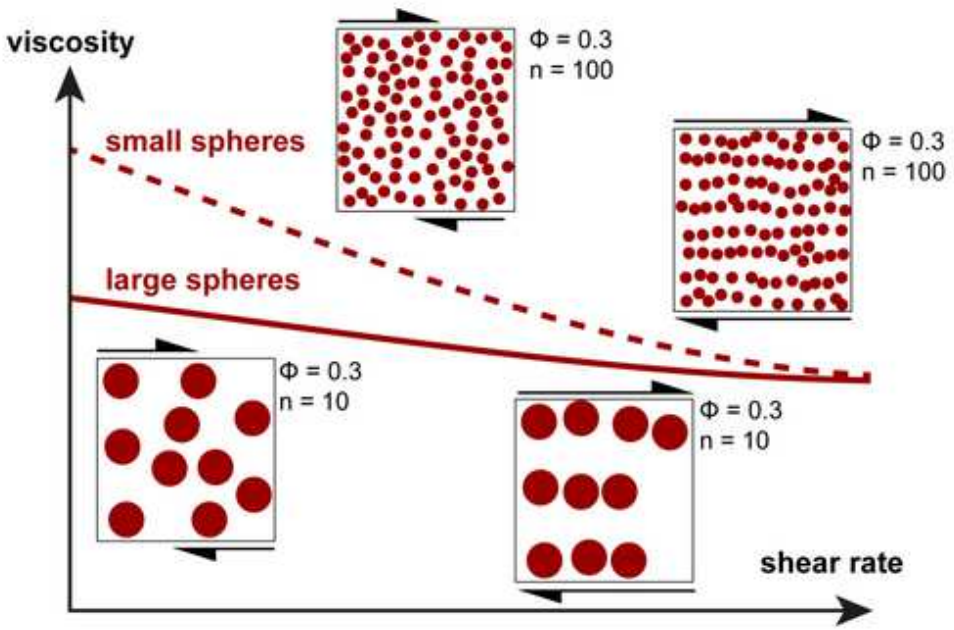

Figure 2.16. *Rheological behavior of the system depending on the size of particles (image from wiki ANTON PAAR website).*

The schematics reported above assumed a monodisperse system. For polydisperse systems, the viscosity can be affected by the size distribution, as shown in Figure 2.17. At constant shear rate and solid fraction, the viscosity decreases with mixing polydisperse particles, as polydisperse suspensions have a higher ϕ_{max}. So, in the Krieger & Dougherty equation, the ratio is lower, and consequently so is the viscosity. At constant solid fraction, the number of particles in a polydisperse system is lower than in a monodisperse system of small particle, implying that it will be easier to move the particles with the flow in the polydisperse system; therefore, its viscosity is lower.

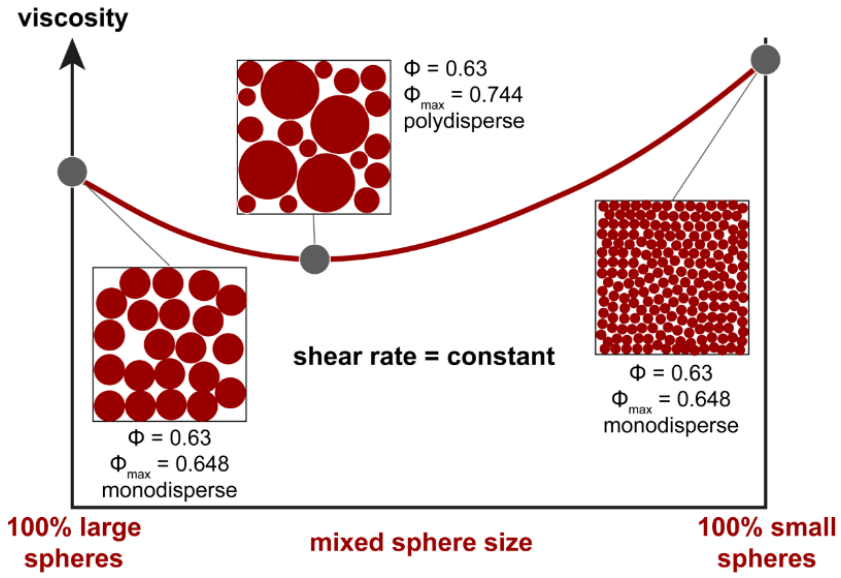

Figure 2.17. *Viscosity of a polydisperse system at constant shear rate and constant solid fraction (image from wiki ANTON PAAR website).*

Finally, the shape of the particles can also influence the viscosity of the colloidal system, as shown in Figure 2.18. In the system with ellipsoidal particles, it is necessary to use higher shear stress to initiate the flow of the system. The randomness of the orientation does not facilitate the flow, making the viscosity higher at low shear rate. Then, when those particles are aligned with the flow, there are less resistance to the flow due to their profile compared to the system with only spherical particle making the viscosity lower at higher shear rate.

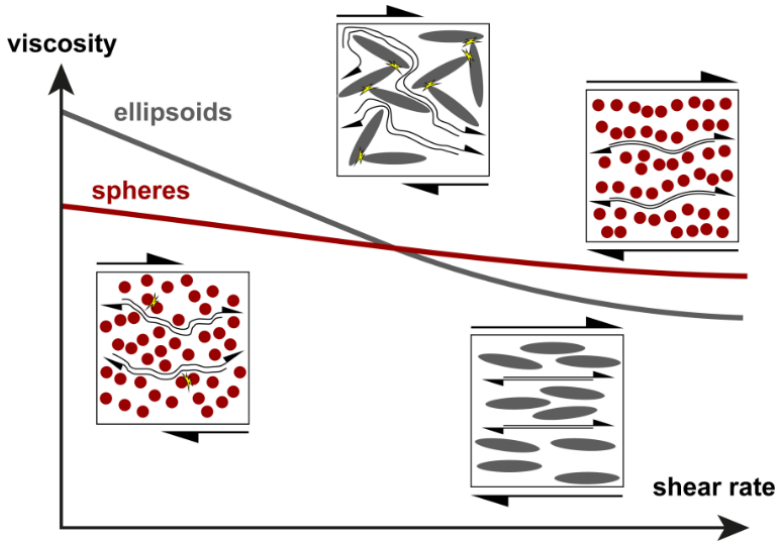

Figure 2.18. *Effect of the shape of the particles on the viscosity for a monodisperse system (image from wiki ANTON PAAR website).*

2.3 Parameters affecting ink printability

2.3.1 Rheology

As mentioned earlier, controlling the rheology of the ink is crucial to ensure printability. For DIW, suitable inks must possess two essential features: (i) a yield stress and (ii) a shear thinning behavior. Fluids that possess these features generally follow the Herschel Bulkley behavior[44]:

$$\sigma = \sigma_0 + K\gamma^n \qquad \textbf{EQ. 16}$$

with σ and σ_0 the shear stress and the yield stress in shear (Pa), respectively, γ the shear rate (s-1), K the consistency index (Pa.s^{-n}) and n the flow behavior index (dimensionless). If $n < 1$, the ink is shear thinning; if $n > 1$, the ink is shear thickening; the fluid is Newtonian if $n = 1$. The yield stress needs to be high enough for the ink to not flow under its own weight when inside the syringe and to maintain it shape after deposition. As discussed earlier, the shear thinning behavior not only facilitates the flow of the ink in the nozzle but also plays a significant role in the maintain of the line shape after deposition. The ink possesses a complex shear modulus G which is expressed as follow:

$$G = G' \cos(\theta) + G"sin(\theta)$$ **Eq. 17**

with G' and G" the storage and loss modulus (Pa) of the ink, respectively, and θ the phase angle. When θ = 0°, the energy is entirely stored, meaning the materials is elastic; when θ = 90°, the energy is entirely lost, meaning the material is viscous. In between, the material is visco-elastic, which is the case for inks used in DIW. The measure of the storage and loss modulus is useful for the determination of the yield stress and the storage modulus at equilibrium. Those materials often exhibit a thixotropy behavior, which implies the reduction of viscosity over time under a constant stress, and the return to its initial state upon load removal.

2.3.2 Flow inside the nozzle

Another important aspect for the printability of the ink is the flow inside the nozzle. Knowing this can help to determine the process parameters. For Direct Ink Writing, there are two common types of nozzles: cylindrical and conical.

2.3.2.1 Cylindrical nozzle

When pressure is applied on the ink inside the syringe to overcome the yield stress, the ink will flow through the nozzle. The radial shear stress inside the ink can be expressed as the following:

$$\sigma_{rz} = \frac{r\Delta P}{2l}$$ **Eq. 18**

with σ_{rz} the radial shear rate, r the radial coordinate, ΔP the pressure difference between the entrance and the exit of the nozzle and l the length of the nozzle. Notice that the radial shear stress increases linearly along the radius. At some point along the radius, the radial shear stress will overcome the yield stress of the material, meaning that the ink in an annular region will start flowing. At that point, the ink is composed of three parts: a core plug that moves as a rigid body, an annular shear thinning layer and outer layer corresponding to the slip of the ink at the wall.

Similarly, the shear rate possesses a radial gradient in the nozzle where the maximum is reached near the wall. The shear rate and the flow rate can be related using the following expression[45]

$$\dot{\gamma} = \frac{4Q}{\pi r^3} \text{ and } Q = sdt \qquad \textbf{Eq. 19}$$

where $\dot{\gamma}$ is the shear rate, Q is the flow rate, *r, s, d, t* are, respectively, the radial coordinate, the ink speed, the diameter of the nozzle and the thickness of the layer. S.L.Morissette *et al.*[45] differentiated the layer thickness from the diameter of the nozzle. This differentiation can be explained by an expansion of the ink after exiting the nozzle or by an over deposition due to a pressure too high. In more recent publications[34], the problem is simplified, and the layer thickness is considered equal to the diameter of the nozzle. By combining Eq.16, 18 and 19, the pressure applied is directly related to the speed of the tabletop. The resulting curve represents the set of parameters corresponding to the optimal line is obtained.

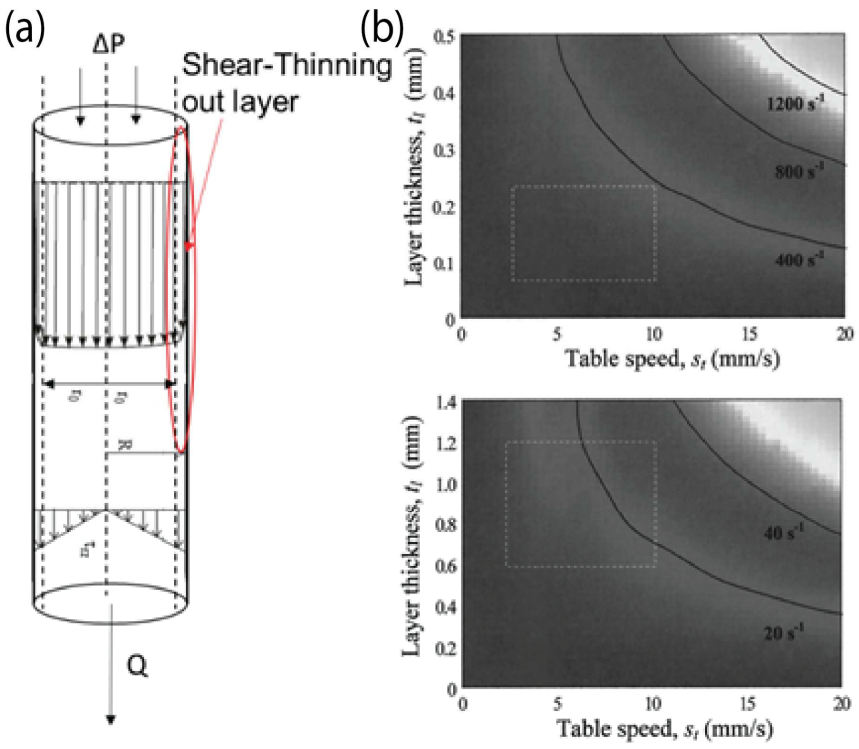

Figure 2.19. *(a) Flow of pseudoplastic fluid in cylindrical nozzle. (b) Relation between the tabletop speed and the layer thickness*[45].

2.3.2.2 Conical nozzle

The shear rate increases with decreasing the nozzle diameter. For a given nozzle diameter, the shear rate is constant all along the cylindrical nozzle. On the other hand, in the case of the conical nozzle, the maximum value of the shear rate is reached only at the exit, making it more suitable for high viscosity material. However, the calculation of the flow is more complicated. The flow rate can be expressed as follows[46]:

$$Q_{shear} = \frac{\pi r_i^3 r_o^3}{4}\left[\frac{3n\,tan(\theta)\left(\Delta P - \frac{2\sigma_0}{tan(\theta)}\,ln\frac{r_i}{r_o}\right)}{2K(r_i^{3n} - r_o^{3n})}\right]^{1/n} \qquad \textbf{EQ. 20}$$

where r_i and r_o are the radius of entrance and exit, respectively; θ is the angle of the nozzle and *K, n,* σ_0 are the rheological parameters from the Herschel-Bulkley model. During the flow through

the nozzle, the highly loaded suspension can experience slip at the wall. The slip flow rate can be expressed as follows[46]:

$$Q_{slip} = \frac{\pi \delta_t r_o^2}{K^{1/n}} \left[\tau_0 + \frac{3n \tan(\theta) \Delta P}{2\left\{1 - \left(\frac{r_o}{r_i}\right)^{3n}\right\}} \right]^{1/n} \quad \textbf{EQ. 21}$$

with δ_t the slip layer thickness. Then, we can calculate the total flow rate of the ink in the tapered nozzle as[46]:

$$Q_{total} = Q_{shear} + Q_{slip} \quad \textbf{EQ. 22}$$

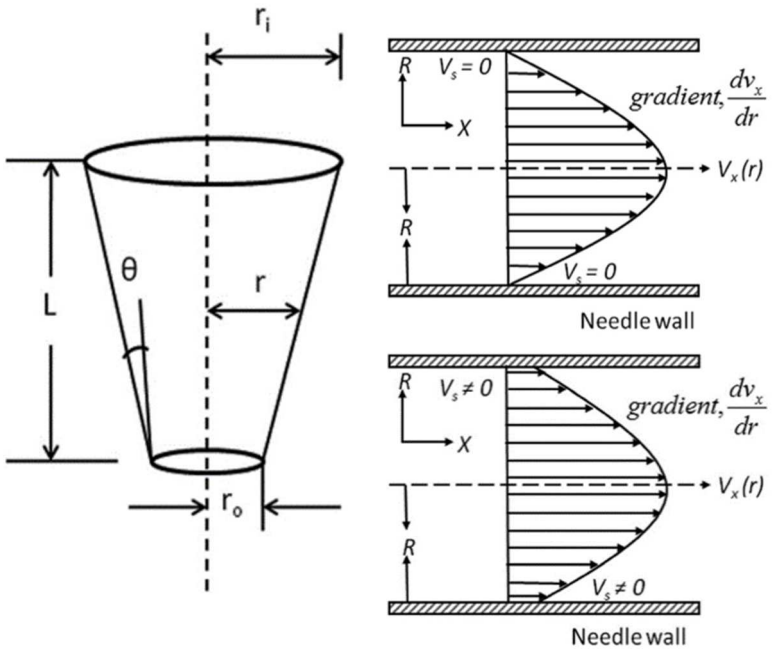

Figure 2.20. *Schematic of a conical nozzle. Flow profile of a fluid in a pipe with and without slip at the wall*[46]

Finally, the flow rate can be directly related to the speed of the tabletop using the following expression[46]:

$$V = \frac{4Q_{total}}{\pi t^2} \quad \textbf{EQ. 23}$$

where V is the tabletop speed and t is line thickness. As previously discussed, an optimal print is achieved when the thickness of the layer is considered equal to the diameter of the line.

2.3.3 Deposition behavior

Several parameters can affect the deposition behavior of the ink. The first aspect is the distance between the nozzle tip and the tabletop. H. Yuk *at al.*[47] have shown that by varying the height and the speed, the shape of the line will be different, going from accumulation mode at low speed and large height, to discontinuous line mode at high speed and lower height. They have shown that by controlling those parameters we can even get line thinner that the nozzle diameter (Figure 2.21).

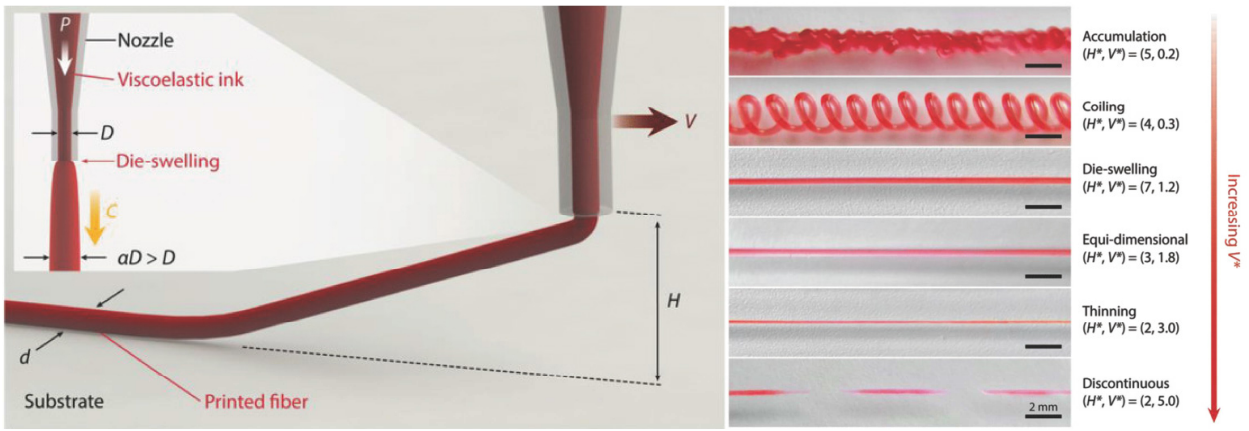

Figure 2.21. *Effect of the speed and height on the printability of a viscoelastic ink*[47].

The second aspect is the span distance of the line between two anchor points. J.Smay *et al.*[48] have shown that it was possible to predict the span distance by knowing the value of the storage modulus at rest. This can be done by using the following expression:

$$G'_{min} \geq 1.4\beta s^4 D \qquad \textbf{EQ. 24}$$

with G'_{min} the storage modulus at rest, β the specific weight of the ink ($0.25(\rho_{gel} - \rho_{medium})g$), s is the reduced span distance (=L/D), L is span distance, D is the rod diameter. The specific weight depends on the density of the medium used for printing. In most cases, this medium is air but can

also be an oil to reduce drying. The results are shown in Figure 2.22 where we can see the deflection of the rod for different values of pH and so values of G (The gelation of the system is control with the pH: above a certain value of pH the ink turns into gel and the storage modulus increases in value).

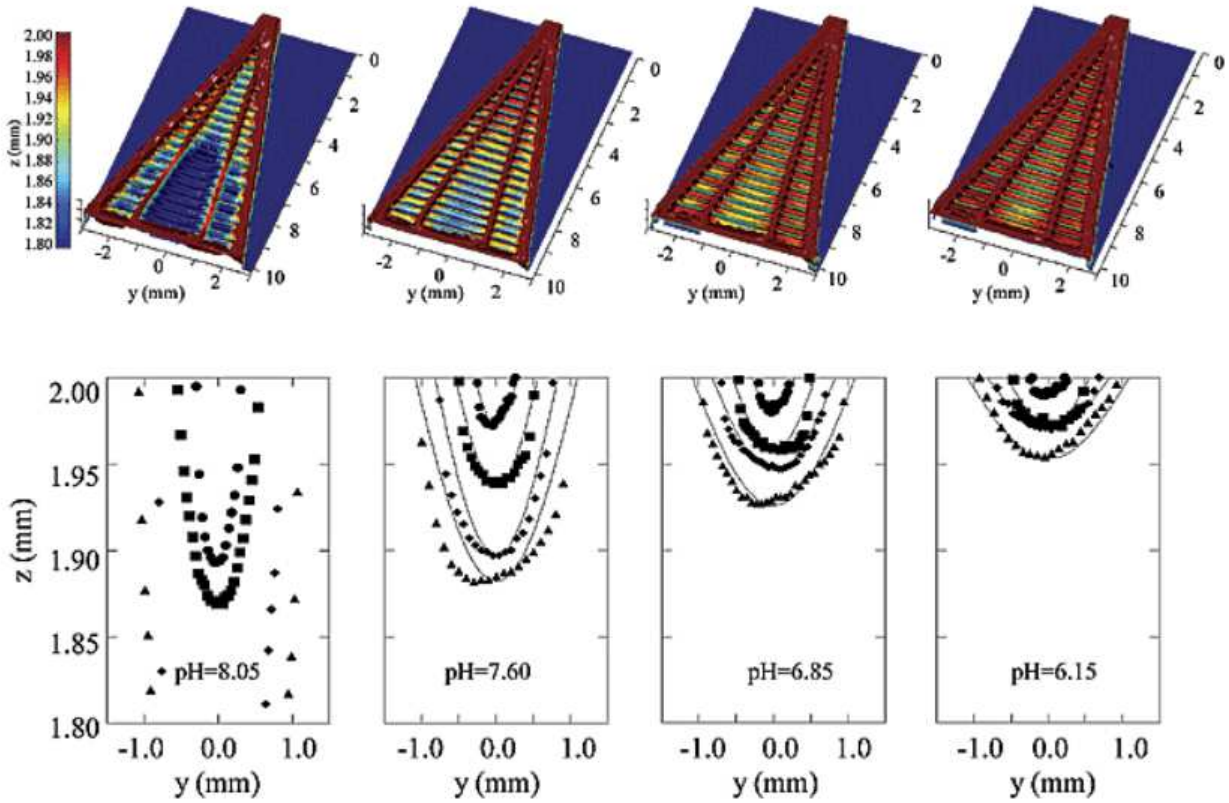

Figure 2.22. *Effect of the pH on the span distance of an ink*[48].

The last aspect is how the line maintains its own shape after being deposed. Forces such gravity and surface tension act on the line. To be able to maintain its shape, the yield stress must overcome the forces applied on the line. A. M'Barki *et al.*[34] have shown this with their boehmite slurry, and defined a parameter expressing the printability of the ink:

$$\Xi = \frac{\sigma_y^{Dyn}}{\gamma_s R^{-1} + \rho g h} \quad ; \quad \Xi_\gamma = \frac{\sigma_y^{Dyn}}{\gamma_s R^{-1}} \qquad \textbf{EQ. 25}$$

where ρ is the density of the ink, g is the gravitational constant, h is the height of the structure, R is the nozzle diameter, γ_s is equal to the suspension's surface tension, σ_y^{Dyn} is the dynamic yield stress, and Ξ is a non-dimensional number and is plotted on Figure 2.23. The plots represent the relation between Ξ and A/A_{th}. A is the area of the printed structure and A_{th} is the theorical area. To get a good printability, the ratio A/A_{th} should be close to 100%, which can be achieved when Ξ is superior to 1. This is shown for different nozzle sizes and different volume fraction of boehmite.

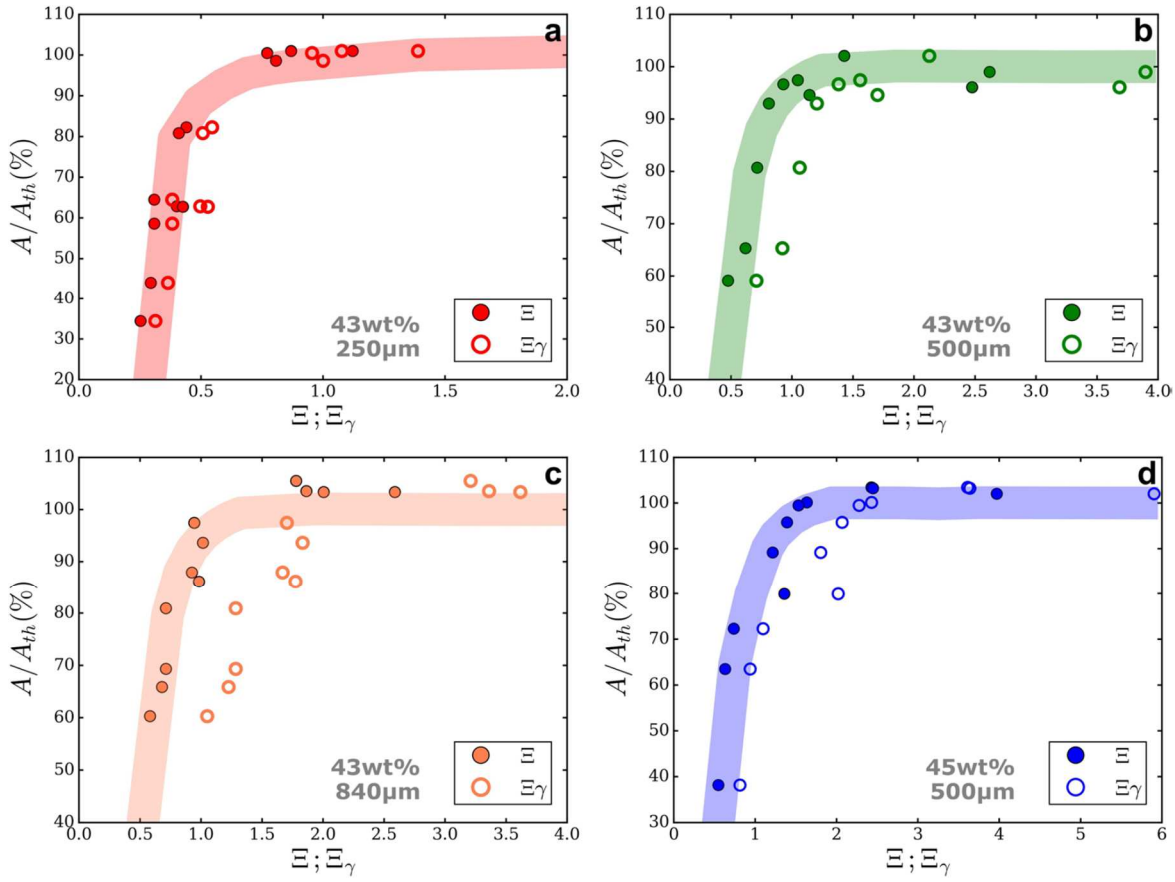

Figure 2.23. *Ability of the ink to maintain its shape for different nozzle and volume fraction*[34]

In conclusion, this literature review provided a deep and complete understanding of the DIW process and the mechanisms governing the process. It showed the importance of the interparticle interactions present in a suspension, their function, and their effects on the rheology. Finally, it revealed how those mechanisms were translated into physical parameters which can be controlled

to obtain an optimal print. This knowledge is necessary to achieve our main goal of fabricating ceramics microlattices.

2.4 Fabrication of a custom DIW printer

As affordable DIW printers are not currently commercially available, a custom printer was assembled for this work. The printer was designed to be composed of three main parts: motion stage, dispensing system, and gantry system.

The motion stage was a 3-axis stage from Aerotech, as shown in Figure 2.24a. It was composed of three ball screw linear stages, which had an accuracy of 1.25 μm over a range of 100 mm. The repeatability was 1 μm. The maximum speed was 300 mm/s. Different ways to arrange the system were possible. We decided to get the stages stacked on top of each other. While not as efficient as the approach with the Z stage mounted on the gantry system, this configuration enabled the entire system to be calibrated and aligned by Aerotech, making us confident that we could get a high-performance stage with 10 μm volumetric accuracy.

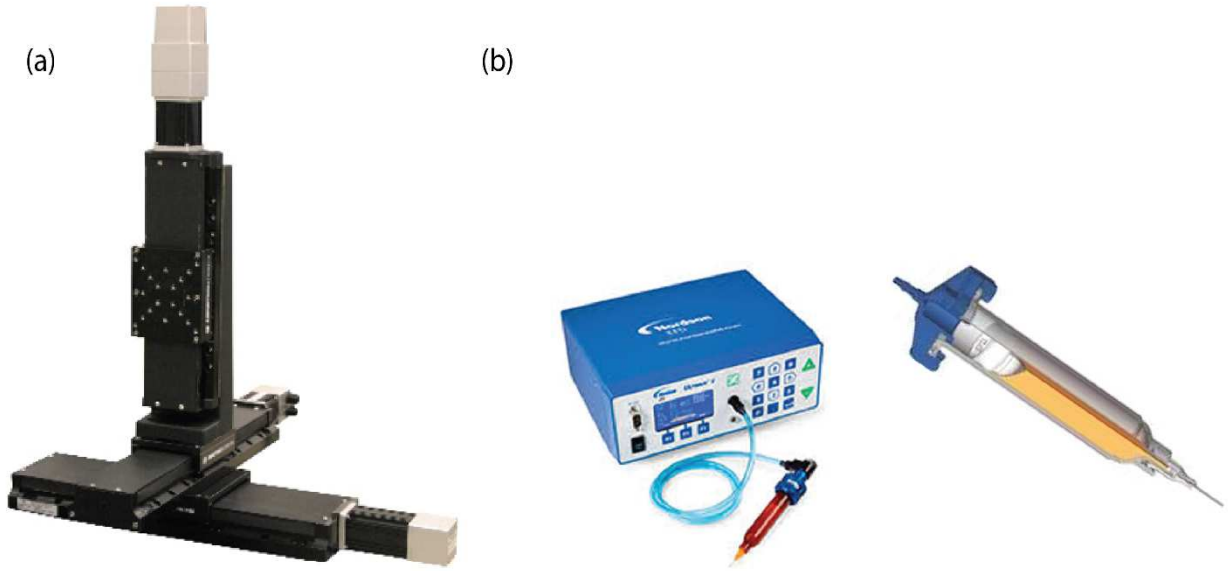

Figure 2.24. *(a) Aerotech motion stage of the custom printer (image from Aerotech). (b) Dispensing system (image from NORDSON EFD website).*

There are two different approaches to dispense the slurry: pneumatic and mechanical. Our dispensing system is composed of the Ultimus V pressure box from Nordson EFD (Figure 2.24b). This pneumatic system can dispense a pressure up to 100 PSI. Several syringes and nozzle sizes can be adapted to the pressure box, respectively, from 5 cc to 55 cc and from 200 μm to 1.19 mm. The syringe is placed on a gantry system made of optical parts from Newport, Inc. The height can be adjusted. Finally, the printer is positioned on an optical table to reduce interferences from the environment (Figure 2.25).

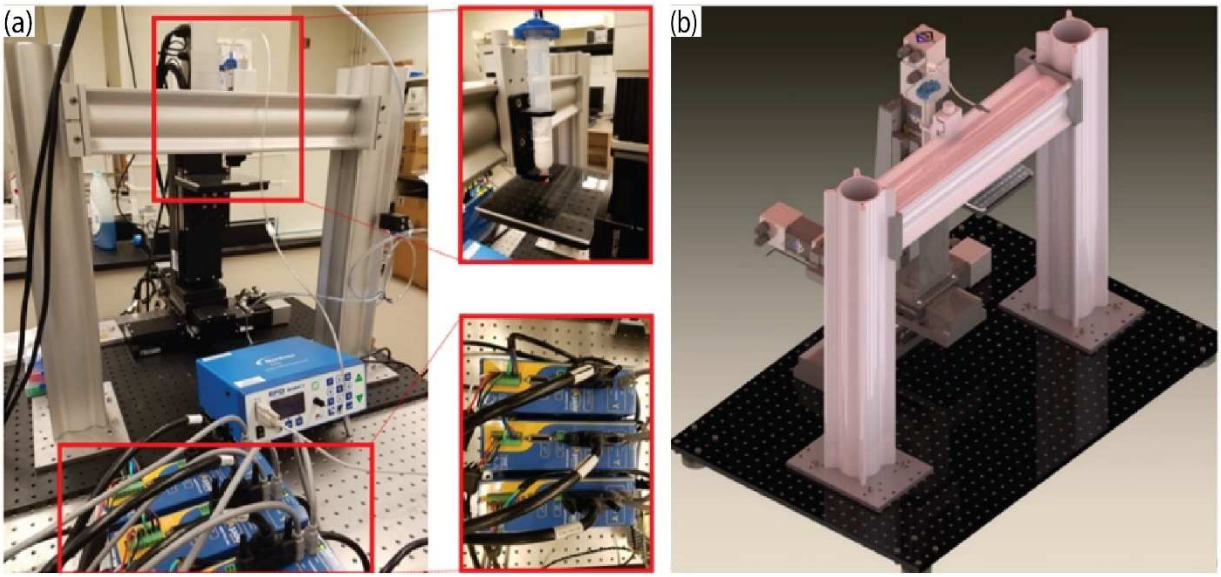

Figure 2.25. *(a) Custom-built DIW printer and (b) CAD model of the complete system.*

2.5 Materials for biomedical applications

The DIW technique is uniquely suited for the rapid fabrication of complex shape components from a wide range of biomaterials. The development and fabrication of biomaterials is a vital area of research in the field of modern medicine, encompassing natural and synthetic materials across the material kingdom, from metals to polymers, ceramics, and glass[49]. A key requirement for most biomaterials is biocompatibility, i.e. the ability of the material to operate inside the human body without eliciting an immune response. Applications of biomaterials span from medical implants and drug-delivery systems to biosensors and tissue regeneration[50,51]. Biomaterials can be broadly categorized into hard, such as ceramics and metals, and soft, such as collagen, gelatin, and hydrogels. Here we briefly summarize the state of the art in bioceramics and hydrogels.

Bioceramics

Ceramics are promising biomaterials, due to their high stiffness and strength and resistance to extreme conditions such as high temperatures, nuclear radiation, and harsh chemicals. Bioceramics

are categorized as bioinert, bioactive, and bioresorbable[52]. Bioinert ceramics are commonly oxides, as their high stability reduces the risk of triggering an adverse reaction through chemical reaction at surface; for example, alumina and zirconia are frequently used for implant applications[53,54]. By contrast, bioactive ceramics elicit a desired response at the interface with tissues, allowing for the formation of a bond; as such, they can be utilized as scaffolds for bone growth to promote tissue regeneration and bone repair[55,56]. Lastly, bioresorbable ceramics provide temporary strength while the tissue regenerates and repairs, gradually being absorbed *in vivo*[57].

Hydrogels

Hydrogels are three-dimensional polymeric network structure able to absorb large quantities of water. Their hydrophilic properties, biocompatibility and biodegradability make them great candidate for biomedical applications, from drug delivery to tissue regeneration, wound healing, and cell delivery. They are also well suited for Direct Ink Writing for several reasons: (i) they often possess the appropriate rheology, (ii) their high-water content prevents premature drying, and (iii) their viscosities can be easily tuned by external elements. In this thesis, the two hydrogels of focus are Pluronic F127 and Alginate acid.

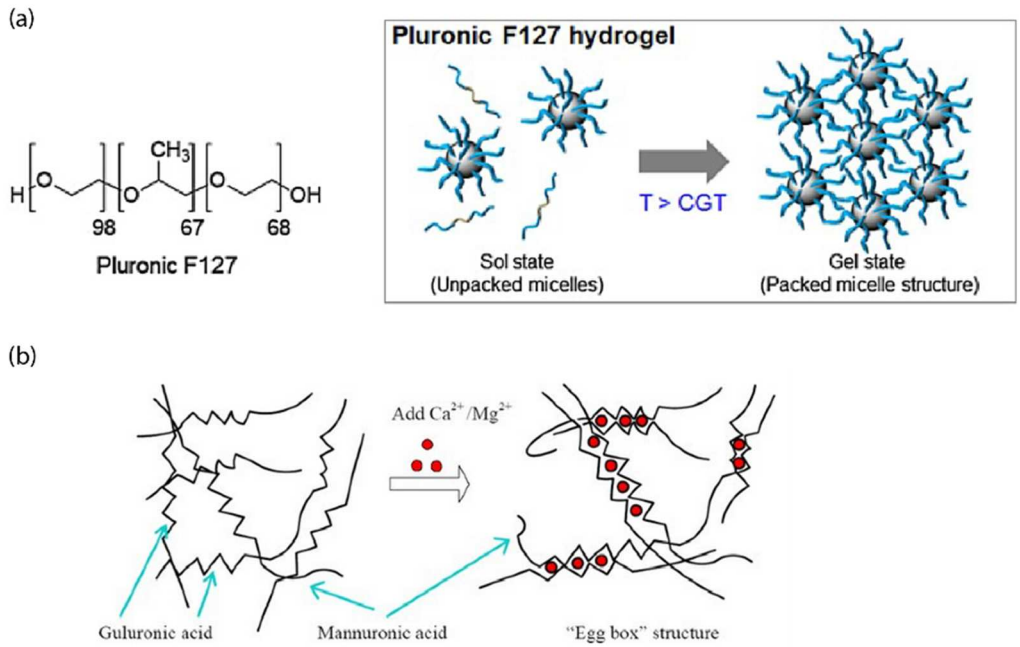

Figure 2.26. *(a) Chemical formula of Pluronic F127 and schematic of the sol-transition of the Pluronic with increase of the temperature*[58]*. (b) Schematic of the crosslinking of alginate by addition of divalent cation to create and "egg box" structure*[59]*.*

Pluronics are a class of synthetic block copolymers. They are composed of hydrophilic poly(ethylene oxide) (PEO) and hydrophobic poly(propylene oxide) (PPO). The hydrophilic block is sandwiched between the two hydrophobic blocks. This combination of hydrophilic and hydrophobic blocks gives surfactant properties to Pluronics. In an aqueous solution, the copolymer molecules self-assemble into micelles in which the PPO block is oriented towards the inside and the PEO towards the outside. The emergence or destruction of those micelles is pH and temperature sensitive. Pluronic F127 is approved by the Food and Drug Administration (FDA) and undergoes a sol-gel transition near physiological temperature and pH, making it a great candidate for biomedical applications. The temperature dependance of the gelation of pluronic simplifies mixing and helps with viscosity control and porosity reduction[13]. The gelation point of pluronic solutions is strongly dependent on the content of pluronic itself (Figure 2.27): 25 wt% of pluronic in an aqueous solution is a suitable formulation for Direct Ink Writing.

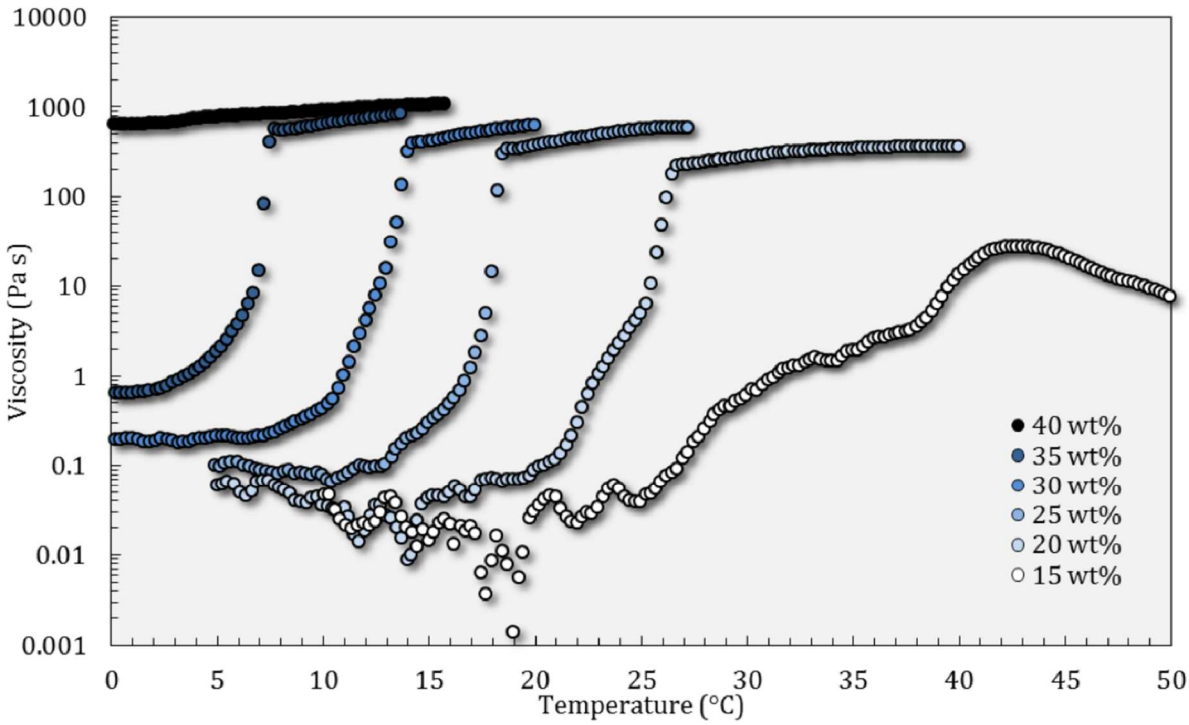

Figure 2.27. *Evolution of the viscosity with temperature for different weight percents of Pluronic. The discontinuity of the curves shows the transition sol-gel*[13].

Sodium alginate is a natural polymer extracted from marine brown algae. It is composed of alternating blocks of α-L-guluronic acid (G) and β-D-mannuronic acid (M) (Figure 2.26b). Alginate has great advantages for biomedical applications such as: biocompatibility, low toxicity, and low cost. The gelation of alginate happens from the guluronic acid blocks in presence of multivalent cations under mild conditions (e.g., Ca^{2+}, except Mg^{2+}) resulting in the formation of a three-dimensional network called the "egg box" model (Figure 2.26b) [59]. The gelation does not require heat or strong stirring. The strength of the gel depends on the calcium concentration as well as the proportion of MM, GG, and MG blocks. For example, a high concentration of G blocks leads to mechanically stronger gel[60]. On the other hand, a high concentration of M blocks produces a softer and more elastic gel with a higher water absorption. Alginate has many biomedical applications, ranging from wound healing to drug delivery and tissue engineering.

3. Damage tolerance in additively manufactured ceramic architected materials

3.1 Introduction

The need for high performance materials with increased temperature resistance, improved mechanical strength and reduced density is a major driving force for materials research, motivated by applications in a wide range of industries, from transportation to aerospace and defense systems. For example, even a modest increase in the high-temperature performance of materials in propulsion systems would significantly raise the fuel efficiency of the engine, with great economical and environmental impact. By virtue of their strong covalent and ionic bonds, technical ceramics exhibit outstanding mechanical properties at high temperature[61,62], and would be exceptional candidates for these applications. Unfortunately, though, their extreme crack sensitivity, coupled with the inevitable introduction of flaws during processing, strongly limits the achievable strength, currently hindering most structural applications in mission critical components. Over the past 50 years, several approaches have been successfully demonstrated to reduce the flaw sensitivity of ceramics and increase their fracture toughness, including transformation toughening and the design of ceramic matrix composites, where toughness is increased via crack deflection, crack bridging and fiber pullout[63]. Yet, in most material systems, the strength of ceramics is still much lower than the theoretical value, often by more than one order of magnitude.

One approach to achieve theoretical strength in ceramics is to reduce the size of the sample to such a small scale that the internal cracks are too small to grow. This approach has been recently demonstrated for silicon oxycarbide (SiOC) and carbon, produced by two-photon polymerization Direct Laser Writing (2pp-DLW) of a suitable pre-ceramic resin followed by pyrolysis[6,31,64], with ceramics exhibiting compressive strengths in excess of 7 GPa. The main shortcoming of this

approach is that samples need to be smaller than a critical length scale, typically in the 100 nm – 10 μm range. One avenue towards scale-up is to design and fabricate micro/nano-architected materials, i.e., periodic repetitions of generally identical unit cells along three directions, where the unit cell architecture is optimized for mechanical efficiency and the feature size within the unit cell is sufficiently small for the material to locally achieve theoretical strength. This approach has also been recently demonstrated and has allowed fabrication of porous architected materials with unprecedented combinations of high strength and low density[5,32,64–68] and sample sizes as large as 30 μm[69].

While 2pp-DLW has allowed demonstration of exceptional combinations of properties in ceramic architected materials, the maximum achievable sample size is still far too small for any realistic structural application. Significant scale-up can be enabled by using Direct Ink Writing (DIW), an additive manufacturing (AM) approach whereby an ink is extruded at room temperature through a nozzle and deposited in the form of lines that can be architected in three dimensions. DIW has been successfully used to deposit a wide range of material systems, from metals[8] to biopolymers[70] and composites[35,36,71]. Most inks consist of a suspension of colloidal particles stabilized by the aid of a dispersant; with a rheological modifier to provide the ink with high yield stress and shear thinning behavior, two characteristics that are crucial for achieving excellent quality prints. If ceramic particles are introduced in the ink, and the structure is sintered after printing, high-quality ceramic architected materials can be produced. DIW is a relatively fast approach with high dimensional accuracy, allowing fabrication of structures with overall dimensions at the cm scale and feature sizes (line diameter) down to ~200 μm, in 5 to 15 minutes. While these feature sizes are still too large to expect theoretical strength from the constituent

ceramic, they are small enough to result in significantly better mechanical properties than at the macroscale.

While DIW is somewhat limited in achievable structural complexity relative to other AM approaches, due to the inability to interrupt the flow of material during printing and the limited span that printed lines can sustain without collapsing, recent work has resulted in several innovative solutions, from laser-assisted printing[8], to fast solvent drying[39,72] and printing embedded in a viscoelastic fluid[16], reducing the gap between DIW and other AM approaches.

In this work, an ink is developed that is optimized for printing of architected materials, and results in pure aluminum oxide (Al_2O_3) upon sintering. This ink is used to fabricate woodpile structures, simple architected materials consisting of periodic repetitions of layers of lines arranged in a 0/90° sequence. While this topology is not as structurally efficient as other lattice designs (e.g., the octet lattice[73]), it allows us to investigate the effect of topology on the failure mechanisms of ceramic architected materials. After characterizing the stiffness and theoretical strength of the constituent material via nanoindentation, the strength and failure behavior of woodpile structures with different feature sizes and relative densities are quantified. The results are correlated with microstructural features (including the presence and location of defects in the prints) and interpreted with the aid of simple mechanical models. Topological features in the architected material design are found to be effective at controlling the crack path during failure: remarkably, this enables fabrication of structures that can be much stronger than heavier solid materials printed and sintered under identical conditions, or structures that can fail graciously, displaying a level of damage tolerance that is extremely unusual for ceramics. While results are exclusively presented for alumina woodpile structures, the mechanical effects unveiled in this work are general and will apply to different architected materials topologies and constituent ceramics.

3.2 Experimental Procedures

3.2.1 Raw materials and ink preparation

The ceramic ink was composed of four materials: (i) Grade A-16 SG alumina powder, with an average reported particle size of 0.5 μm (Almatis, USA), (ii) Ammonium polyacrylate (NHPA) (Darvan 821A, R.T. Vanderbilt Company, USA), used as a dispersant, (iii) 1-ethenyl-2-pyrrolidinone (PVP) homopolymer (Sigma-Aldrich, USA), used as a rheology modifier, and (iv) DI water used as solvent. This chemistry, originally proposed by Lisa *et al.*[74], has two key advantages over alternative compositions: the pH, which controls the cohesion between the colloids, remains constant and slightly higher than the particles' isoelectronic point throughout mixing,[75,76] creating repulsion between the particles and stabilizing the suspension, thus eliminating the need for continuous pH adjustments; furthermore, all components have low toxicity, thus facilitating the manufacture of parts as no special safety equipment or chemical disposal is required.

Relative to the composition reported by Lisa *et al.*[74], the volume fractions of the ink components were adjusted to achieve a higher yield stress and storage modulus, while maintaining the desired shear-thinning behavior of the ink. A larger storage modulus allows deposition of longer suspended features[48] and a larger yield stress enables printing of taller structures[34], both of which facilitate the printing of lightweight architected materials. The final chemical composition of the ink was 53 vol.% Al_2O_3, 9.9 vol.% PVP, 4.2 vol.% NHPA and 32.9 vol.% DI water. NHPA was first mixed with DI water in a vortex mixer (Vortex-Genie, Scientific Industries, USA) for 30 s. The alumina powder was sieved with a 100-micron sieve to eliminate large agglomerates, and gradually added to the solution and mixed in a planetary centrifugal mixer (AR100, Thinky, USA) for 20 s at 2,000 rpm. While the viscosity was still low, the ink was placed in a vacuum chamber

to remove most bubbles. As each step of the mixing process results in some loss of water (which varies from batch to batch), the mass of the ink was measured before and after each step and water was added as needed, to maintain the target proportions. PVP was subsequently added to the solution and mixed using a planetary centrifugal mixer at 2,000 rpm for 60 s. The ink was exposed to vacuum again and then carefully loaded in the syringe using a flat spatula to minimize the introduction of bubbles. Finally, the ink was transferred to a new and clean syringe using a luer-lock style connector and the syringe was placed back inside the planetary centrifugal mixer with an adapter and left to defoam for 300 s.

3.2.2 Rheological measurements

The rheological properties of the ink were measured with an AR-G2 rheometer (TA Instruments, USA), equipped with a standard 40 mm sand-blasted parallel plate geometry with a gap of 1 mm. A solvent trap was used to reduce the evaporation of the DI water during the experiment. A flow ramp was applied with shear rates ranging from 100 to 0.1 s^{-1} (and then back to 100 s^{-1}), to capture the evolution of the shear stress and the viscosity as a function of the shear rate. The flow parameters were extracted on the ramp down of the test, in the range from 40 to 0.1 s^{-1}, as secondary flow could appear at high shear rates, altering the results. To ensure good statistics, all parameters were averaged over eight different tests. Subsequently, stress amplitude sweep measurements at a frequency of 1 Hz were conducted in the range of 1 Pa to 4,000 Pa, to extract the storage and loss moduli as a function of the applied stress.

3.2.3 Direct Ink Writing (DIW) procedure and sintering

All structures were built using a custom ceramic DIW printer, composed of a 3-axis motion stage (Aerotech, USA) and an air-powered fluid dispensing system (Ultimus V, Nordson EFD, USA). The linear stages were stacked on top of each other, assembled and calibrated by Aerotech,

resulting in a volumetric accuracy of 10 μm^3 and a 10 cm × 10 cm × 10 cm maximum build volume. The air-powered fluid dispensing system delivered a maximum pressure of 689 kPa. The syringe was stationary on the gantry system, which was assembled with optical-quality structural components (Newport Inc, USA) and mounted on an optical table to reduce vibrations. The gcode for all prints was programmed in the Aerobasics environment. The geometry and build parameters were programmed using a modified version of the code provided in the technical note by William *et al.*[77] Our Direct Ink Writing system has three controllable printing parameters: (i) layer thickness, (ii) dispensing pressure, and (iii) tabletop speed. The first parameter was set to 85% of the nozzle diameter, to ensure good layer-to-layer contact. The other two parameters must be carefully controlled to achieve the best compromise of printing speed and quality[47]. To choose the optimal tabletop speed for any given dispensing pressure, the mass flow rate was measured as a function of the applied pressure, by weighing the amount of ink extruded under a constant pressure drop for 20 s. The tabletop speed was extracted by dividing the mass flow rate by the area of the nozzle and the density of the ink. Each measurement was repeated three times to ensure consistency. A new nozzle was used for each measurement to minimize errors from possible drying of the ink between measurements. The test was performed for three different nozzle diameters: 410 μm, 580 μm and 840 μm. For each nozzle diameter, a direct relationship was obtained between the pressure and the tabletop speed, enabling selection of printing parameters that allow extrusion of lines with thickness equal to the corresponding nozzle diameter. Three sets of those extrusion parameters were selected and validated with printing of actual structures. By observing the print quality, the printing time, and the success rate, an optimal set of parameters was finally assessed.

In this study, both fully dense cubes and woodpile structures were printed, using the same nozzle sizes as previously discussed. The structures were printed by layer-by-layer deposition of lines,

changing printing orientation by 90 degrees at each layer. The distance between the lines, henceforth called gap (g) and equivalent to the pitch (p) minus the diameter (d), in the woodpile structures was chosen to be equal to one or two times the diameter (d_n) of the nozzle (Figure 3.1). As the relative density of a woodpile structure can be approximated as $\bar{\rho} = \frac{\pi}{4}\frac{d}{p}$, samples with a pitch of two and three times the diameter have theoretical relative densities of 39% and 26%, respectively. The pitch for the fully dense specimens was chosen as 80% of the line diameter, to minimize internal porosity[13]. The dimensions of all prints were 1 cm × 1 cm × 1 cm. To demonstrate the smallest features that can be obtained with this ink, 5 mm × 5 mm × 5 mm woodpile structures were also printed with a 200 μm nozzle, although full characterization was not performed on these structures.

All printed parts were conventionally sintered in air using a muffle furnace (Lindberg, USA). A multistep sintering schedule was employed to ensure that all binders and organics were eliminated prior to sintering. First, the samples were heated up at a rate of 5°C/min to 700°C and held at this temperature for 1 hr to burn off the polymer. Subsequently, the specimens were heated at the same rate up to 1,600°C and held at this temperature for 1 hr to ensure complete densification. Finally, they were cooled down to room temperature at a rate of 5°C/min. Bulk density measurements of the alumina were performed on both fully dense and woodpile structures using the Archimedes method.

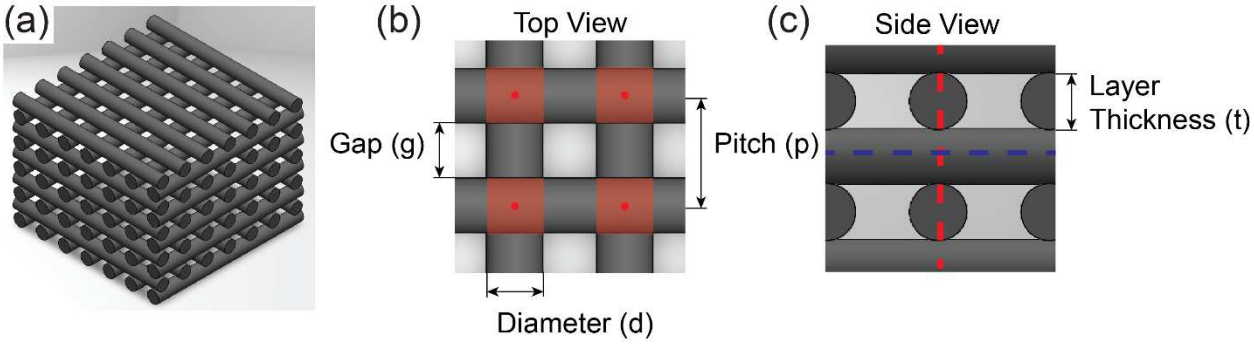

Figure 3.1. *Computer-Aided Design CAD model of the woodpile structure, presented as (a) perspective, (b) top and (c) side view. The red shaded regions represent the area in contact between layers. The red and blue dashed lines represent the columns and bridges, respectively.*

3.2.4 Materials characterization and mechanical measurements

Microstructure and grain size information was acquired from fracture surfaces of specimens using a FEI Magellan 400 XHR scanning electron microscope (SEM), operated at 3 kV. Computed tomography (CT) scans were performed using a Xaria 410 Versa (Zeiss, USA) with a voltage of 55 kV and a resolution of 15 µm.

Nanoindentation tests were performed on the bulk sintered samples using a Nano Indenter G200 (Agilent Technologies). For each sample, at least 20 indentations were performed with a maximum load of 200 mN. The distance between the two nearest indents was 30 µm, which was larger than 30 times the penetration depth (~700 nm), thus avoiding interference. The hardness (H) was extracted from the unloading section of the load-displacement curves as $H = P/A$, with P the load applied on the sample surface and A the projected contact area at that load. The Young's modulus ($E_{Al_2O_3}$) was also obtained from the unloading curve as $\frac{(1-\nu^2)}{E_{Al_2O_3}} = \frac{1}{E_r} - \frac{(1-\nu_i{}^2)}{E_i}$, where ν and ν_i correspond to the Poisson's ratio of the sample (assumed to be = 0.2 for alumina) and the indenter (= 0.07), respectively, and E_i is the Young's modulus of the indenter (= 1141 GPa); E_r is the reduced modulus, $E_r = \frac{\sqrt{\pi}\,S}{2\beta\sqrt{A}}$, where β is a constant related to the indenter geometry (= 1.034),

and S is the elastic stiffness of the contact and obtained from the slope of the initial 50% of the unloading curve. To minimize the effect of structural compliance, woodpile structures were tested in the regions corresponding to columns of multiple line intersections (red regions in Figure 3.1a).

Macroscopic compression tests were performed on the bulk sintered samples using an Instron 8800 servo-electric Universal Test Frame, equipped with a 100 kN load cell. A constant displacement rate of 0.033 mm/s was used for all tests. Images of the samples were collected using a camera (Point Grey, USA) from the digital image correlation system (Correlated Solutions, USA) every 300-500 ms during the test, to provide information on the deformation sequence and the failure mechanisms. Those images are synchronized with the load and displacement measurements from the Instron machine. The nominal sample dimensions are used to calculate the stress and strain. A polymeric pad was interposed between the sample and the top compression plate (the bottom being already flat since the specimen was printed directly on a flat surface), to minimize the risk of premature failure due to stress intensifications related to sample non-planarity.

3.3 Results and Discussion

3.3.1 Rheological properties of the ink

The rheology of the ink is crucial to ensure its printability. For DIW, suitable inks must possess two essential features: (i) a suitable yield stress and (ii) a shear thinning behavior. Fluids that possess these features can generally be described by the Herschel-Bulkley model[44]:

$$\sigma = \sigma_0 + K\dot{\gamma}^n \qquad \textbf{EQ.16}$$

where σ and σ_0 are the applied shear stress and the yield strength in shear (Pa), respectively, $\dot{\gamma}$ is the applied shear rate (s^{-1}), K is the consistency index ($Pa.s^{-1}$) and n is the flow behavior index (dimensionless). The ink is shear thinning for $n < 1$, Newtonian for $n = 1$ and shear thickening for $n > 1$. A shear thinning behavior indicates a decrease of viscosity with increasing shear rate, thus

facilitating the flow through and out of the nozzle. At the same time, the yield strength must be sufficiently large for the ink to not flow under its own weight when inside the syringe and to maintain its shape after deposition. During extrusion, the shear stress increases along the radius of the nozzle. Consequently, the flow profile is typically composed of a solid core experiencing stress lower than the yield strength, and an outer layer experiencing shear-thinning behavior.

The parameters of the Herschel-Bulkley equation are extracted from a flow curve, where the shear rate is progressively increased while the shear stress is measured. The results are reported in Figure 3.2a. The behavior of the ink is clearly shear-thinning, characterized by an average yield strength, $\sigma_0 = 602$ Pa and an average flow behavior index, $n = 0.7$.

The yield stress of the viscoelastic ink can also be independently estimated by an analysis of the evolution of storage and loss moduli (G' and G", respectively) of the material as a function of an applied oscillatory stress (Figure 3.2b). For $\sigma < 1$ kPa, the ink displays a plateau in G' with a value that is about an order of magnitude larger than G", indicating solid-like viscoelastic behavior. At larger stresses, the gap between G' and G" narrows, indicating a decrease in the fraction of recoverable strain and a gradual transition toward a viscoelastic liquid. Finally, at $\sigma \sim 1$ kPa, both moduli precipitously drop, and the trend is inverted (G' < G"), indicating a transition to liquid-like behavior. Hence the transition point, $\sigma \sim 1$ kPa, can be taken as a measure of the yield stress of the ink. Importantly, the value of the zero-shear storage modulus ($G'_0 \sim 300$ kPa) is sufficiently large to avoid line deflection while printing the woodpile structures. We emphasize that a careful rebalancing of the volume fractions of polymer, water, and alumina relative to the amounts used in Lisa *et al.*[74] resulted in an ink with a yield stress ~5 times larger, suggesting that the formulation presented herein is much more suitable for fabrication of architected materials.

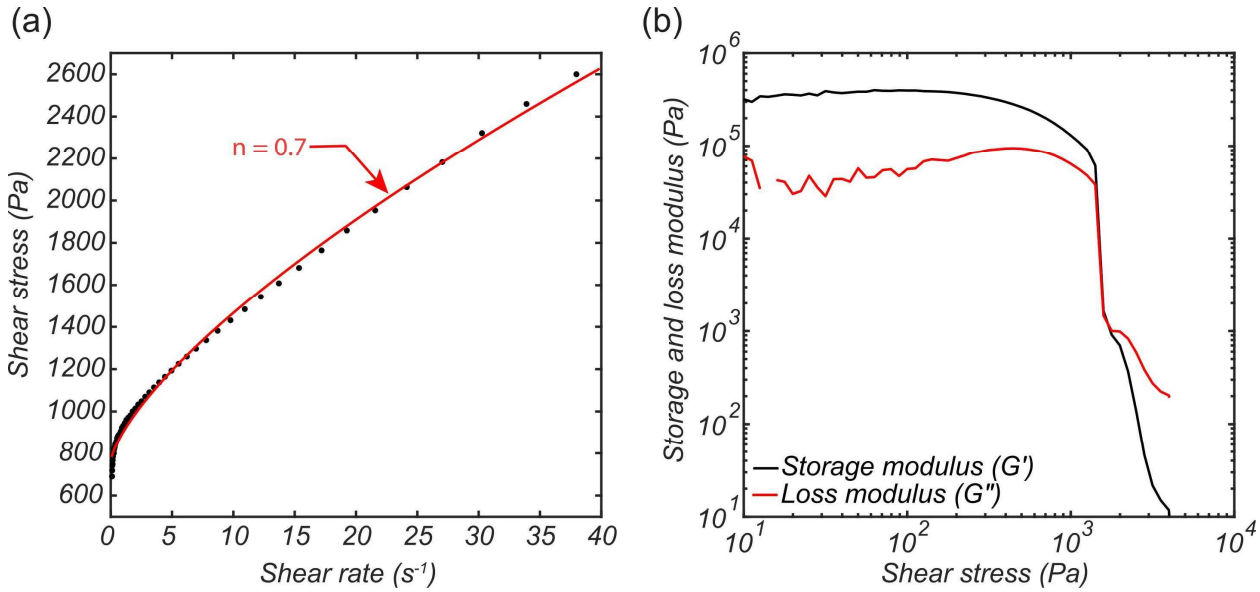

Figure 3.2. *(a) Shear stress vs shear rate for the alumina ink. (b) Storage and loss moduli for the alumina ink, showing a yield stress of ~10^3 Pa.*

3.3.2 Extraction of optimal printing parameters

The optimal relation between applied pressure and tabletop speed is extracted for three nozzle sizes (410 µm, 580 µm and 840 µm), as detailed in Sec. 3.2.3, and plotted in Figure 3.3a. While the nozzle size does not have a significant impact on the pressure-speed relation, these small disparities may influence the quality of the print. Notice that at high pressure the tabletop speed tends to asymptote, indicating a progressive difficulty in extruding the ink at higher speeds. This phenomenon can be tentatively attributed to jamming of the particles near the nozzle tip resulting in a filtering effect, and/or local shear thickening of the concentrated suspension.

While all combinations of pressure and tabletop speed depicted in Figure 3.3a are in principle capable of generating successful prints, not all conditions are equally effective. Increasing the pressure considerably reduces the print time, but excessive pressures will result in extrusion difficulty, as noted above, with potentially deleterious effects on printing performance and/or part quality. The implication is that an optimal printing pressure must be identified. To estimate this value, three sets of pressures / tabletop speeds were selected and used to print test samples at

different nozzle sizes. All test samples are woodpile structures with gap equal to the line diameter, allowing accurate evaluation of the geometric fidelity of the process. The samples printed with a pressure of 69 kPa did not result in successful samples (Figure S1.1). We observe that pressures of 138 kPa and 207 kPa can generate high quality prints (Figure 3.3b). However, at higher pressure (207 kPa), the nozzle clogs more often than at lower pressures, resulting in a lower success rate for the prints. Additionally, high pressure results in over-deposition at the end of the woodpile where the nozzle turns around, resulting in the formation of a nearly dense outer layer: this compromises geometric accuracy, wastes ink and may result in undesired crack nucleation sites. Among the three pressures tested, a pressure of 138 kPa is the most suitable to achieve good and repeatable quality prints, while minimizing the printing time.

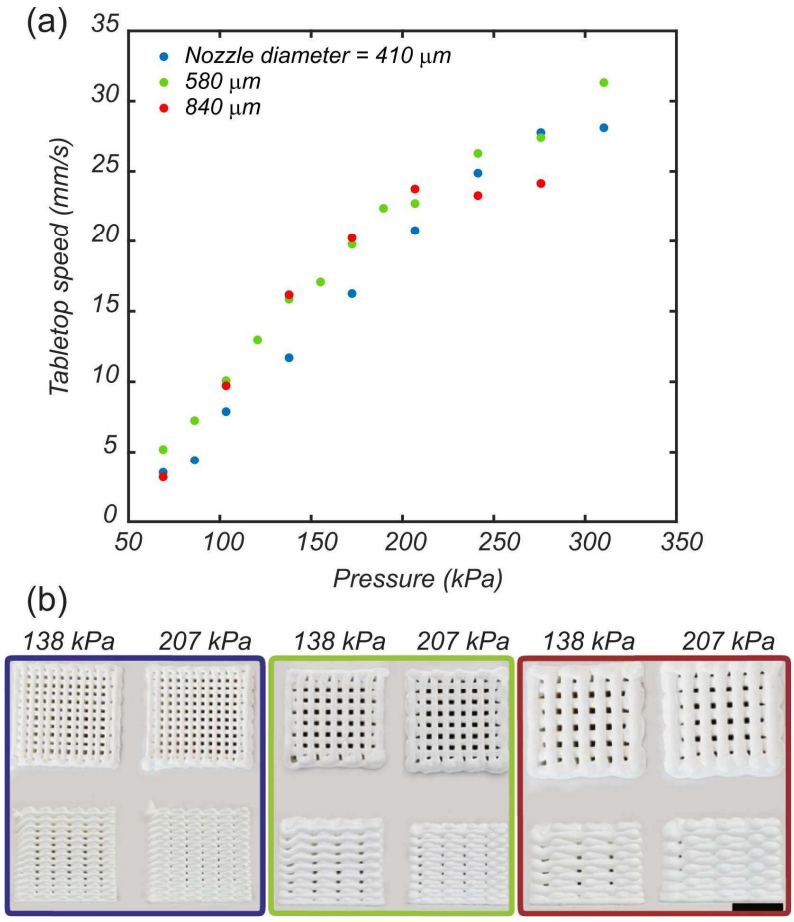

Figure 3.3. *(a) Relationship between the tabletop speed and the pressure applied for different nozzle diameters (410 μm, 580 μm and 840 μm). (b) Green bodies of woodpile structures printed for different pressures and nozzle sizes. Scale bar: 5 mm.*

Figure 3.4a shows a slice from a cross sectional CT scan of the woodpile structure printed with a 580 μm nozzle and a gap nominally equal to the line diameter. Only the lines printed perpendicular to the image plane are shown in the scans. The lines are numbered from the lowest to the highest in the direction of printing, represented with the red arrow. Notice that the lines have a larger diameter (~650 μm) and smaller gap (~300 μm) for the first two layers, as shown in Figure 3.4b. Subsequently, the dimensions stabilize to a diameter of ~500 ± 34 μm and a gap of ~400 ± 54 μm, demonstrating good print quality. The steady-state values of both line diameter and gap are lower than the design values, a discrepancy that can be attributed to the drying and sintering of the

structure. The large line diameter at the beginning of the print (~650 µm) can be attributed to two reasons: (i) the flow needs some time to stabilize after initiation and (ii) the layer in contact with the substrate (layer 0, not shown on the scan) is intentionally more compressed to ensure good adhesion. Figure 3.4c shows a plot of greyscale values along the path denoted by the red arrow in Figure 3.4a. For more clarity, the scan has been converted to a binary image before extracting the histogram (with 1 representing the line and 0 the gap in between). This demonstrates that consistent periodicity was also achieved in the vertical direction.

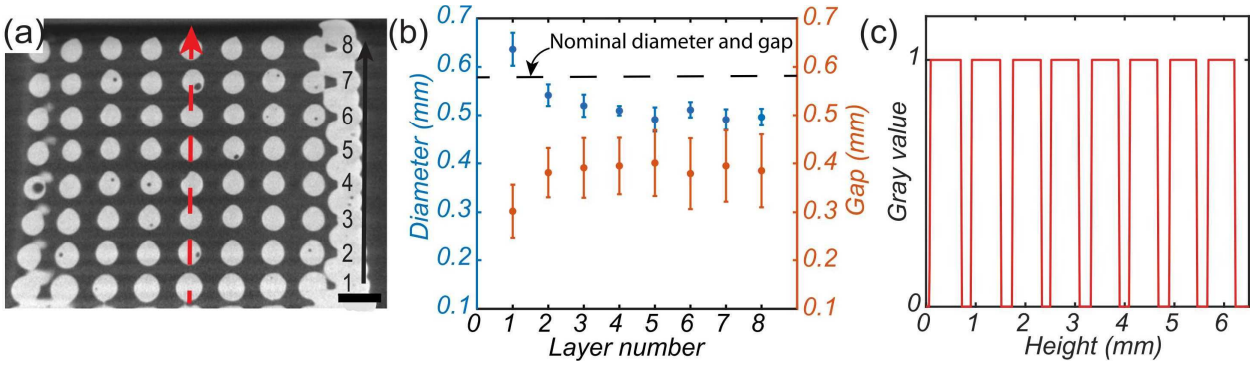

Figure 3.4. *(a) CT scan of the cross section of the alumina woodpile structure printed with a 580 µm nozzle and a gap nominally equal to the line diameter. The black arrow represents the build height direction. (b) Evolution of the diameter and the gap with the printed layer (dimensions are averaged over all lines in a layer). (c) Plot of greyscale values along the red dashed line, indicating excellent periodicity. Scale bar: 1 mm.*

To better understand the impact of nozzle geometry and ink properties on the optimal printing parameters, the relationship between applied pressure and tabletop speed is analytically modeled. For a given pressure, the shear rate increases with decreasing nozzle diameter. While in a cylindrical nozzle the shear rate is uniform along the nozzle length, in a conical nozzle (as the ones adopted in this study) the maximum value of the shear rate is reached only at the exit, making it more suitable for extrusion of high viscosity materials. The flow rate of a viscoelastic material following the Hershey-Bulkley behavior in a conical nozzle can be approximated as follows[46]:

$$Q = \frac{\pi d_i^3 d_o^3}{256}\left[\frac{3n\ tan(\theta)\left(\Delta P - \frac{2\sigma_0}{tan(\theta)} ln\frac{d_i}{d_o}\right)}{2K\left(\frac{d_i^{3n} - d_o^{3n}}{2^{3n}}\right)}\right]^{1/n} \quad \textbf{Eq. 26}$$

where ΔP is the pressure drop along the nozzle length, d_i and d_o are the diameters at the entrance and exit of the nozzle, respectively, θ is the angle of the nozzle, and K, n, and σ_0 are the rheological parameters of the ink. Finally, the flow rate can be trivially related to the tabletop speed (V) as $V = 16Q/\pi t^2$, where t is the line thickness. It is assumed that under optimal printing conditions, the diameter of the line (d) equals the nozzle diameter (d_n).

In Figure 3.5a, the experimentally derived pressure-tabletop speed relations (from Figure 3.3a) are compared to the model (black line), using the Herschel-Bulkley parameters extracted from the rheological measurements. As expected, our experimental data are in good agreement with the model at low pressure. As the pressure is increased, the experimental data starts plateauing and diverges from the model. This discrepancy could be attributed to multiple causes, including the use of a parallel plate geometry for the rheological measurements (resulting in variable shear rate along the radius), the fact that the model does not account for the actual surface roughness of the syringe and conical nozzle, the possibility that particles experience jamming and self-filtration in the converging flow, or shear thickening at the exceedingly high shear rates near the nozzle tip (see below). Despite these disagreements at higher pressure, this data demonstrates the usefulness of first-order analytical models in extracting optimal printing parameters from simple rheological experiments. The maximum shear rate experienced by the ink at any section of the nozzle was calculated along the nozzle length for different values of the dispensing pressure (Figure 3.5b). Notice that the shear rate significantly increases closer to the tip and this increase happens further upstream in the nozzle at higher pressure. The dark red area in Figure 3.5b indicates the region of the nozzle where the shear rate is higher than 40 s^{-1}. In this regime, the behavior of the ink becomes

harder to experimentally characterize, as the centrifugal forces in the rheometer start expelling ink from the plates. This region is present for every nozzle size and for every pressure studied here. The important implication on the selection of optimal printing parameters is that a trade-off must be sought between the evaporation of the solvent resulting in clogging of the nozzle at low pressure, and the dominance of high shear rate in the nozzle causing a resistance to flow at high pressure. We observed that good printing quality is obtained at the pressure ranges in which experiment, and model are in good agreement. At higher pressures, a significant amount of ink experiences high shear rates at the nozzle tip, triggering the secondary effects described above, and resulting in lower print quality.

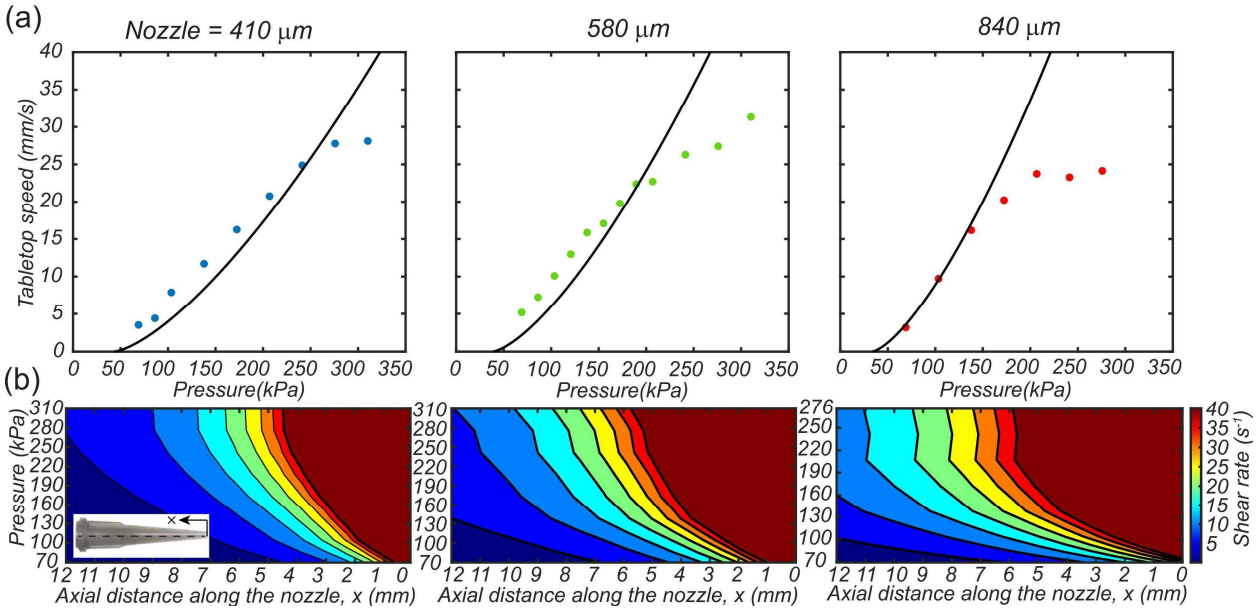

Figure 3.5. *(a) Comparison between the analytical model and the experimental measurements. (b) Map of the maximum shear rate along the conical nozzle, at different dispenser pressure values. Results are presented for three nozzle diameters: 410 μm, 580 μm and 840 μm.*

This understanding of the ink rheology and its behavior inside the conical nozzle allows the printing of highly dense ceramic woodpile structures with small feature size. Figure 3.6 shows two examples of alumina woodpile structures printed with a 200 μm diameter nozzle, differing in the

gap size (equal to one or two times the nozzle diameter) and hence in relative density. Notice that the gap in the printed and sintered structures (103 ± 10 μm and 254 ± 22 μm for the single-diameter and double-diameter structures, respectively) is smaller than the programmed value, consistent with findings reported in Figure 3.4. Nonetheless, we note that even at this small nozzle diameter, which approaches the printability limit for such a highly loaded ink, the diameter of the line (236 ± 6 μm and 259 ± 22 μm for the single and double gap structures, respectively) is close to the size of the nozzle diameter.

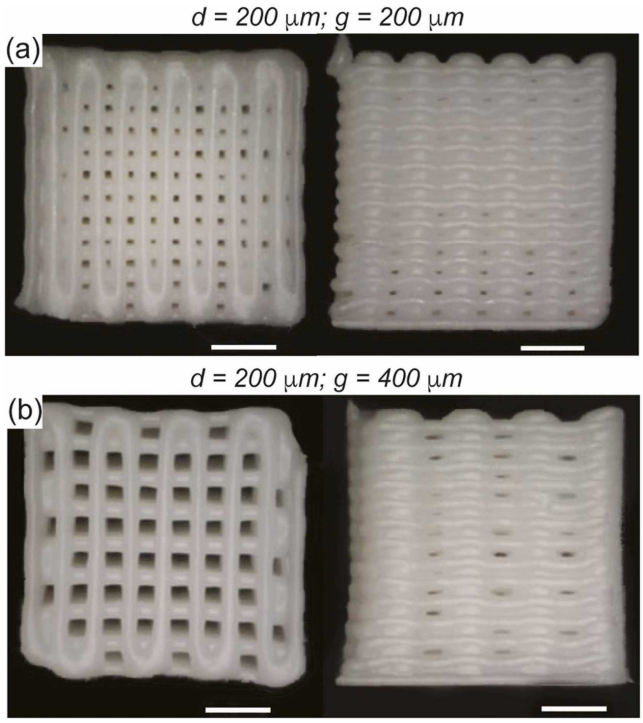

Figure 3.6. *Woodpile structure manufactured using the 200 μm nozzle with (a) a pitch equal to the line diameter and (b) a pitch that is twice the line diameter. Scale bar: 1 mm.*

3.3.3 Microstructural Evolution

Figure 3.7 shows fracture surface SEM micrographs of a woodpile structure (Figure 3.7a) and fully dense specimen (Figure 3.7b) after sintering, both printed with a 580 μm nozzle. A large pore on the inner surface of the woodpile structure is shown in Figure 3.7c. The bulk density and

average grain size for the strut of the woodpile structure and the fully dense specimen are similar. The bulk density is found to be around 98% of the theoretical density of alumina. This excellent bulk density value (low porosity) is attributed to the fine particle size distribution of the powder and the high temperatures used during sintering. From the micrographs, we extracted an average grain size of 2.22 ± 1.25 µm for the woodpile structures printed with the 580 µm nozzle size, 2.80 ± 1.39 µm for those printed with the 410 µm nozzle (not shown on the figure) and 1. 9 ± 0.9 µm for the fully dense specimen. The grain size inside the large pore is the same as the grain size calculated on the fracture surfaces, indicating that the distribution of the grain size is homogeneous throughout the sample. Two different types of pores are observed, corresponding to defects at two different length scales. The largest pores range from several hundred microns to ten microns and are often randomly distributed. The surface of a representative large pore is depicted in Figure 3.7c. These pores originate from the ink preparation and the formation of bubbles. Pores smaller than 1 micron are observed between grains (Figure 3.7a) and are attributed to residual porosity left over after sintering.

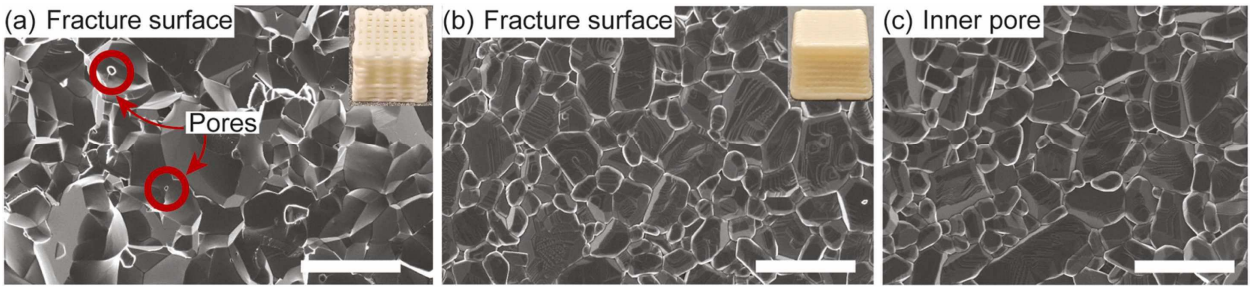

Figure 3.7. *Scanning electron micrographs of sintered alumina structures printed with a 580 µm nozzle size: (a) fracture surface of a woodpile structure; (b) fracture surface of a fully dense sample; (c) inner surface of a large pore in the woodpile structure. Notice that the grain size is ~2 µm in all specimens. Scale bar: 5 µm.*

Computed tomography (CT) scans are extracted to investigate the quality of the print. Figure 3.8 shows representative slices of the CT scan for fully dense samples (Figure 3.8a-b) and

woodpile structures (Figure 3.8c), after sintering. All scans were taken parallel to the platform, with the line direction for the fully dense specimens indicated by an arrow. Flaws and defects are visible as darker regions in the CT scans. A few important observations can be extracted:

(a) Whereas in ideal woodpile structures each pair of adjacent layers is connected by individual points (see Figure 3.1), the choice of a layer thickness lower than the line diameter and the relaxation that follows ink deposition lead to extensive overlap between layers. As a result, two adjacent layers are observable in a single CT slice, with both horizontal and vertical lines (Figure 3.8c).

(b) Both the fully dense and woodpile samples show uniform shades of gray throughout the sample, indicating homogeneous sintering.

(c) Different types of defects can be clearly identified. (i) *Delaminations*, which can be observed as dark shadows moving through the slice (Figure 3.8a), are only observed in the fully dense sample and form during sintering. (ii) *Cracks* are only present in the fully dense samples (Figure 3.8b) and do not follow the printing direction. (iii) *Pores* are present and randomly distributed in both structures. In the woodpile structure, pores are clearly visible within the lines. These pores originated from mixing and loading of the ink inside the syringe; even though the mixing process was optimized to reduce the number of bubbles inside the ink, complete elimination of the bubbles is impossible[78]. Additionally, in the fully dense specimens, entire rows of pores changing direction by +/-90° from one layer to another (Figure 3.8b) can also be observed. These pores are related to imperfect bonding between adjacent lines.

While array of pores between adjacent lines have previously been observed in SEM micrographs of dense ceramic specimens fabricated via Direct Ink Writing[78,79], extensive

delaminations between layers and curved cracks are not generally reported in the literature. While process parameter optimization may certainly mitigate the presence of these defects (e.g., increasing line overlap can eliminate inter-line array of pores[79]), we point out that these delaminations and curved cracks can only clearly be observed by CT scanning, a technique that is not routinely employed for characterization of ceramics. In any case, the lack of delaminations and curved cracks extending through multiple print lines in our woodpile structures confirm that architected material design strategies can be used to effectively control defect population, size and shape in 3D printed ceramic materials.

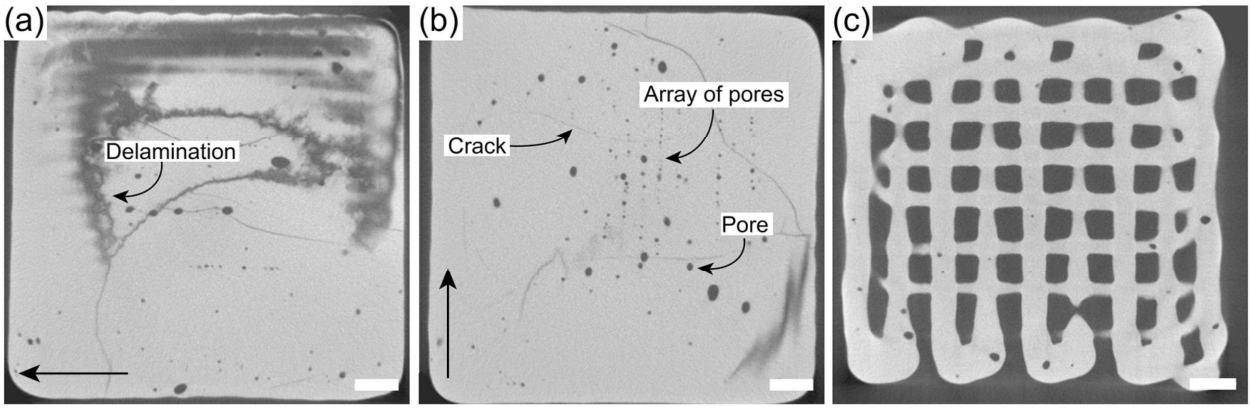

Figure 3.8. *CT scans of sintered alumina structures: fully dense sample showing extensive delamination (a) and rows of aligned pores (b), and woodpile structure showing isolated pores and well-sintered square connection areas between layers (c). Scale bar: 1 mm.*

3.3.4 Mechanical properties

To explore potential size effects on mechanical properties related to the line diameter, nanoindentation is performed on a fully dense sample printed with a 580 μm nozzle diameter and woodpile structures printed with 200 μm and 580 μm nozzle diameters, respectively. The results are shown in Table 3.1.

	Young's Modulus (GPa)	Hardness (GPa)
Fully dense sample (580 μm nozzle)	*383± 13*	*22.5 ± 1.7*
Woodpile structure (200 μm nozzle)	*384 ± 13*	*23.3 ± 1.4*
Woodpile structure (580 μm nozzle)	*352 ± 16*	*22.4 ± 1.2*

Table 3.1. *Summary of nanoindentation results on fully dense specimens and woodpile structures printed with 200 μm and 580 μm nozzles.*

The Young's moduli of the fully dense structure printed with the 580 μm nozzle, the woodpile structures printed with the 200 μm and the 580 μm nozzle are nearly identical, and in good agreement with literature values for both conventionally sintered dense alumina (340-400 GPa for sample with porosity between 0 to 2%)[80,81] and alumina samples printed via DIW (300-370 GPa for samples with porosity between 1 and 5%)[78,79]. All three samples also have nearly identical hardness (H~23 GPa), in good agreement with literature data (20-26 GPa)[82]. From Tabor's relationship[83], the theoretical strength of alumina ($\sigma_{Al_2O_3}^{f,th}$) can be estimated as $\sigma_{Al_2O_3}^{f,th} \sim H/3 = 7.5$ GPa. While this relationship is commonly applied to non-strain-hardening metals, it has also been shown to be reasonably accurate for ceramics (including Al_2O_3) under low strain rates[84,85]. Collectively, these results show that (i) sintered lines printed with different nozzle sizes have virtually the same mechanical properties (no size effect in this feature size range), and (ii) all samples are fully sintered, and reach the mechanical properties of dense alumina with minimal porosity.

Several sintered woodpile structures printed with different nozzle sizes and pitches were subjected to quasi-static macroscale compression experiments, alongside a few sintered dense specimens. The actual geometric dimensions of each sample are reported in Table S1.1 in the Supplementary material. Representative stress-strain curves are shown in Figure 3.9, with strength

and damage tolerance data presented in Figure 3.10. The compression strength is extracted from the stress-strain curves at the highest stress drop that corresponds to catastrophic failure of the structure, represented as the black dots in Figure 3.10. The relative densities experimentally measured and reported in Figure 3.10a deviate quite significantly from the theoretical predictions (Table S1.1 and S1.2 in the Supplementary Material). As previously discussed, the gap and the line diameter are smaller than the predicted ones due to drying, sintering, choice of layer thickness smaller than the line diameter to ensure good contact and relaxation of the ink after deposition, resulting in denser woodpile structures.

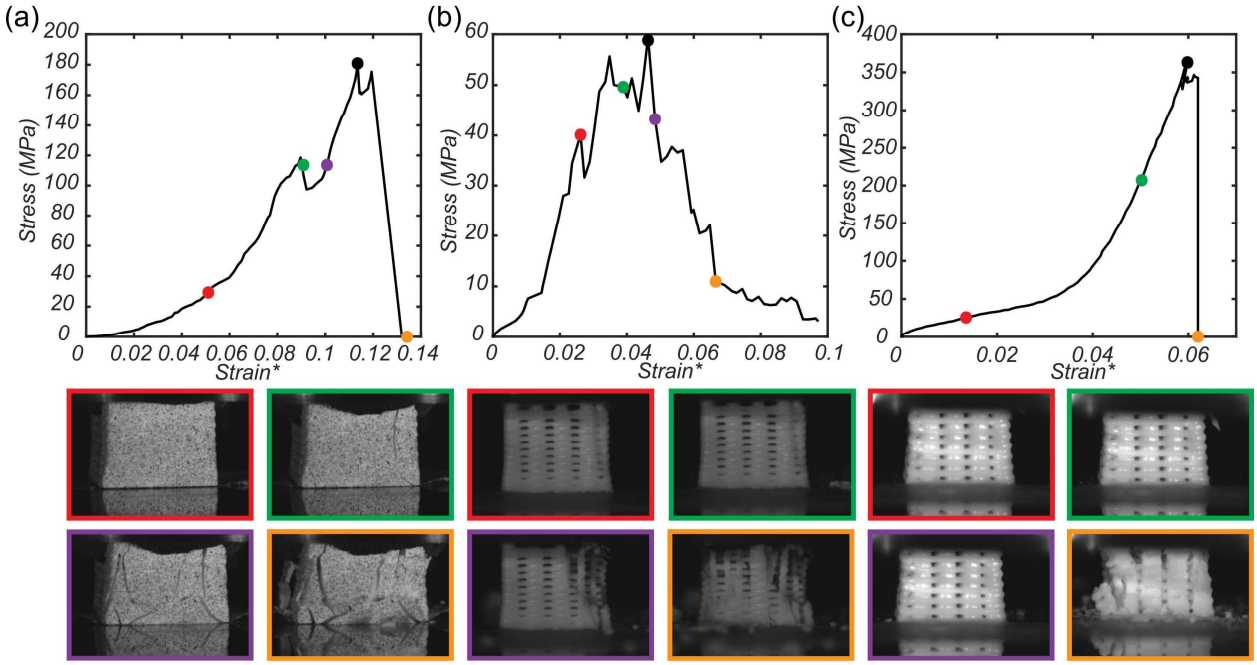

Figure 3.9. *Stress/strain curves of representative (a) fully dense specimens, printed with a 580 µm nozzle size and (b, c) woodpile structures, with the following characteristics: d = (410 µm,580 µm); g = (410 µm,580 µm);* $\overline{\boldsymbol{\rho}}$ *= (0.55, 0.59). Notice that woodpile structures can be designed to fail less catastrophically than fully dense structures (b) or to be much stronger than fully dense specimens that are twice as dense (c). The black dots represent the events used to measure the compressive strength. *Note that the strain does not represent the true strain of the specimen but rather a combination of the strain of the specimen and the elastomeric pad interposed between sample and loading plate to mitigate stress intensifications.*

Three important observations can be extracted from representative stress-strain data (Figure 3.9): (1) Fully dense specimens (Figure 3.9a) fail catastrophically by through-sample propagation of critical cracks, at stresses that are ~50 times lower than the theoretical strength of the material. This brittle behavior is attributed to the presence of rows of pores along the inter-line boundaries, cracks and delaminations throughout the sample (Figure 3.8a, b). (2) Low-relative density woodpile structures (Figure 3.9b) can be weaker than fully dense specimens, but they display damage tolerance, with gradual failure characterized by multiple sequential load drops. Each load drop corresponds to the failure of a column of material, with columns separating from the rest of the sample upon failing. This unusual behavior is attributed to topological toughness, whereby the separation of load-bearing elements in the sample introduces robustness. (3) High-relative density woodpile structures can be more than twice as strong as fully dense specimens with only half the density. This interesting behavior is attributed to the presence of less pre-existing delamination in woodpile structures, and the absence of rows of pores and cracks that extend beyond a single line diameter. These strong woodpile structures tend to fail catastrophically, whereby a column of material fails and induces collapse of the entire structure.

From observations (2) and (3), we conclude that the mechanical behavior of our woodpile structures can be engineered by tuning their relative density: in particular, as relative density increases, our metamaterials transition from a gradual to a catastrophic failure mechanism, with corresponding tradeoffs in the mechanical properties. While graduate failure in ceramic cellular materials loaded in compression has been observed for decades in a variety of material systems,41 to the best of our knowledge the transition in failure mode reported herein (and the ability to control it via additive manufacturing) has not been previously reported. While Martin *et al.*[87] observed a similar gradual failure during the compression of hydroxyapatite woodpile structures, they did not

observe a transition from gradual to catastrophic failure with increasing relative density, likely due to the low strength of hydroxyapatite, leading to the premature failure of individual columns and bridges.

Simple mechanical modeling can help elucidate the impact of materials properties and topological features of the architected materials on their strength and damage tolerance. When loaded along the vertical direction, only the material adjacent to the nodes, red shaded regions in Figure 3.1b, contributes to the load carrying capacity of the structure. Approximating those load bearing regions as square columns of cross section $d \times d$ and length l equal to the thickness of the sample, the compressive strength of the woodpile structure can then be expressed as $\sigma_{wp} = \sigma_{col}\bar{\rho}_a$, with $\bar{\rho}_a = (d/p)^2$ the areal density of columns in the sample and σ_{col} the compressive strength of an individual column. When loaded under compression, columns can fail by brittle fracture or elastic buckling. In the former case, $\sigma_{col} = \sigma^f_{Al_2O_3}$, with $\sigma^f_{Al_2O_3}$ the brittle strength of alumina. In the latter case, the strength of a column supported by horizontal braces (the bars in the *(x,y)* plane as shown as the blue dash line in Figure 3.1c) can be estimated with the theory of buckling of columns on elastic foundations[88], leading to $\sigma_{col} = \frac{\pi^2}{12} E_{Al_2O_3} (\frac{d}{l})^2 \,/\, (\frac{L_{eff}}{l})^2$, with $E_{Al_2O_3}$ the elastic modulus of alumina, l the thickness of the sample (length of the column), and L_{eff} an effective length of the column that depends on the stiffness of the elastic foundation. $\frac{L_{eff}}{l} = f(\Pi)$, where $\Pi = \frac{3\pi}{4} \frac{d}{l-d} \left(\frac{l}{d}\right)^4$. The function f is a decreasing function of Π, with $f(0) = 1$ (corresponding to the case of no horizontal braces), and $f(\infty) = 0$[88]. For the samples investigated in this study, Π ranged between 48,858 and 1,448,249, resulting in $\frac{L_{eff}}{l} = 0.032 - 0.074$, and predicting buckling strength for the column in the range 4.1 X 10^5 - 4.0 X 10^4 GPa. While the value of $\sigma^f_{Al_2O_3}$ depends on the concentration of defects (pores, cracks) within the columns and is not known a priori,

$\sigma^{f}_{Al_2O_3} < \sigma^{f,th}_{Al_2O_3}$ ~7.5 GPa. The conclusion is that elastic buckling is never an active failure mechanism for the materials under consideration, and brittle fracture of the columns dominates. The analytical strength prediction can be plotted against the relative density of the woodpile structure for different values of $\sigma^{f}_{Al_2O_3}$ (Figure 3.10a) and compared with measurements performed over 34 woodpile structures with different topological parameters. A value of $\sigma^{f}_{Al_2O_3} = 300$ MPa agrees best with the experimental results. Fitting of the experimental strength data on a power law equation yields a scaling of $\sigma_{wp} \sim \bar{\rho}^{2.2}$ (Figure S1.2), in good agreement with the theoretical prediction of $\sigma_{wp} \sim \bar{\rho}^{2}$. The low R-square ($R^2$=0.165) is not surprising for flaw-sensitive ceramic materials. While the scatter in the strength data is larger than in previously published studies on similar materials [87], this is partly attributed to the fact that we report the measured relative density of each specimen, as opposed to the value based on the ideal geometry.

To assess the impact of topological parameters on the damage tolerance of ceramic woodpile structures, we invoke the following mechanical argument. When a woodpile structure is loaded along the vertical direction, all columns are loaded in compression. Statistically, one column will contain the critical defect that will induce premature failure. Once a column fails, two possibilities exist: the failing column can induce failure of the adjacent columns, with resulting catastrophic failure of the entire specimen (as seen in Figure 3.9c), or the failing column can separate from the adjacent columns by breaking the connecting horizontal lines without inducing failure in other columns; in the latter case, after a small load drop, the woodpile structure can continue bearing load until the next column fails. This behavior is characterized by multiple subsequent non-critical load drops (Figure 3.9b) and results in robustness and damage tolerance. Figure 3.10b plots the number of load drops experienced by a specimen (here taken as a proxy for damage tolerance) as a function of relative density. While the number of load drops cannot be estimated by a simple

mechanical model, the experimental results seem to indicate that damage tolerance scales with the inverse of the square of the compressive strength, as illustrated in Figure 3.10b (for data fit, see Figure S1.2b), albeit with very large scatter. The fact that the strength of the woodpile structure scales as and its damage tolerance scales as $\bar{\rho}^{-2}$ implies that strength and damage tolerance are inversely related. This is clearly observed in Figure 3.10c (for data fit, see Figure S1.2c). While certainly approximated, these simple mechanical models can help in the design of ceramic woodpile architected materials for specific mechanical objectives.

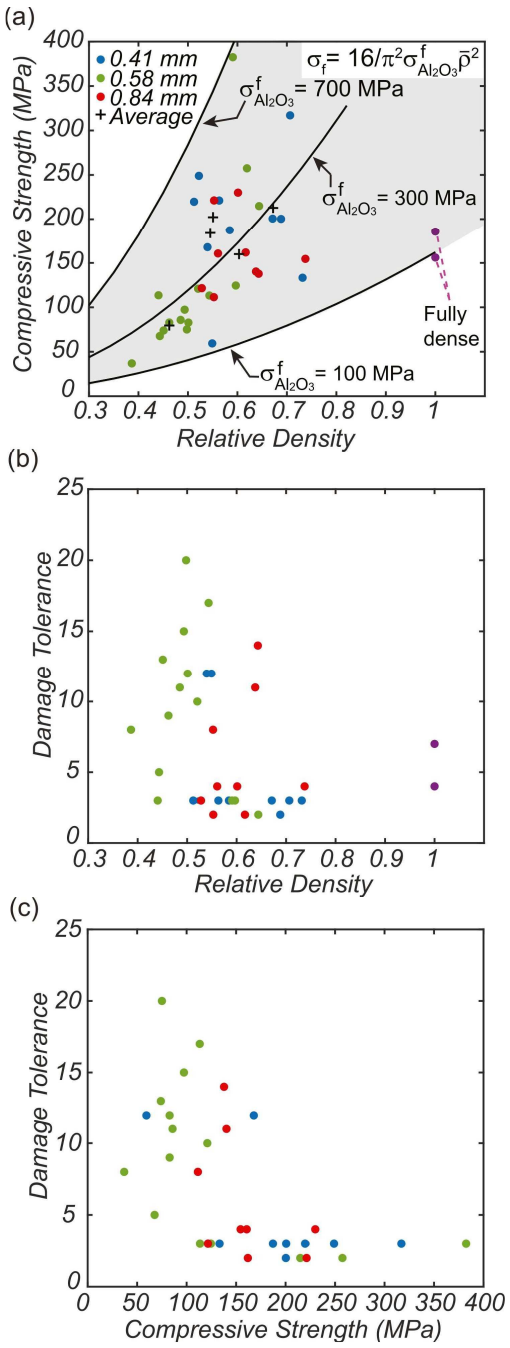

Figure 3.10. *(a) Compressive strength of woodpile structures and dense specimens as a function of relative density. While the scatter is significant (as expected for ceramic architected materials), the experimental data agree with a quadratic scaling, as predicted by the model (for the exact fit on experimental data, see Figure S1.2). Experimental data are consistent with a fracture strength for individual alumina lines of 100 to 700 MPa. (b) Damage tolerance of woodpile structures (defined as the number of stress drops that lead to catastrophic failure) as a function of relative density. (c) Compressive strength cross-plotted against damage tolerance, indicating an inverse relationship between the two properties (for the exact fit on experimental data, see Figure S1.2).*

Conclusions

A new alumina-loaded polymeric ink was developed and characterized. While the rheology of the ink is not fully understood at high shear rate, a combination of experiments and simple modeling allows extraction of a suitable range of optimal parameters, in turn enabling consistent DIW and complete sintering of alumina woodpile structures with line diameters as small as 200 μm. Individual alumina lines achieve Young's modulus and theoretical strength values consistent with fully dense alumina ($E_{Al_2O_3}$~380 GPa and $\sigma^{th}_{Al_2O_3}$~7.5 GPa), independent of line thickness. Quasi-static compressive experiments on fully dense samples and woodpile structures with different line diameters reveal significant *damage tolerance* in woodpile structures, which manifests itself in two key ways: (i) high-density woodpile structures can be twice as strong and twice as light as fully dense specimens printed with identical ink and processing parameters, and (ii) low-density woodpile structures exhibit significant damage tolerance, indicated by multiple stress drops before catastrophic failure. These intriguing features are attributed to the lack of continuous crack paths across the entire sample and the physical separation of load-bearing elements in the woodpile architecture. A simple analytical model captures the strength data and provides guidelines for optimal design. It is demonstrated that architected material topology can be used as an effective tool to control the population and the evolution of defects in additively manufactured ceramic materials, allowing tailoring of the failure mechanisms and tuning of strength and damage tolerance.

4. A high-throughput process for mechanical characterization of ceramic materials produced by Direct Ink Writing

4.1 Introduction

Ceramics have exceptional thermo-mechanical properties, such as high stiffness, high theoretical strength, high melting point and low density. However, their sensitivity to defects (stemming from low fracture toughness) can lead to crack initiation and catastrophic failure during mechanical loading (particularly under tension), severely limiting their applications in mission-critical structural components. Improving the fracture toughness of ceramics entails increasing the energy required to drive a crack in the material. Over the past five decades, three strategies have primarily been pursued towards this goal[89]: (i) increasing the crack tortuosity during crack growth, thus exploiting non-mode I fracture toughness[90–92], (ii) introducing energy dissipation mechanisms around the crack tip, e.g. frictional losses during pull-out in fiber-reinforced ceramic matrix composites (CMCs)[93–97], or (iii) introducing compressive stresses near the crack tip by virtue of stress-induced phase transformations that are accompanied by substantial specific volume increase, e.g., tetragonal-to-monoclinic phase transformations in stabilized zirconia, which gave this exceptional material the moniker 'ceramic steel'[98–100].

More recently, the development of ceramic architected materials (e.g., porous materials with generally periodic and topologically optimized unit cells) has provided new strategies to increase the tensile strength of ceramics. The first one consists of fabricating metamaterials where the constituent ceramic is locally never thicker than a few hundred nanometers, thus ensuring that any processing-introduced cracks are too small to grow and the material locally achieves theoretical strength; while exceptionally promising, this technique requires scalable manufacturing of metamaterials with an enormously large number of unit cells, a currently impossible task. The second approach involves careful design of the material topology to impede fast growth of a

continuous crack through the entire component[101–104]. In the previous chapter, we demonstrated that 50% dense alumina metamaterials with an architected woodpile topology possessed similar compressive strength as fully dense bulk alumina samples printed with the same technology[105]. This study strongly suggested that manufacturing of ceramic systems with complex internal architectures presents an intriguing and promising pathway to produce a new class of strong and light materials for thermo-structural applications.

The complex topologies of architected materials, combined with the reduction in processing-induced internal cracks that arises from scale reduction at the sub-unit cell level, necessitate the use of highly precise additive manufacturing (AM) methods. Among the multitude of AM techniques, Direct Ink Writing (DIW) offers unique combinations of properties, namely resolution at the hundreds of microns scale, ability to print components at virtually any overall size, and an extremely versatile materials palette, allowing printing of virtually any ceramic material with minimal internal porosity[9]. DIW involves the layer-by-layer deposition of a slurry, whereby control of the rheology is crucial to achieve good printability and thus viable parts.

The development of DIW strategies for printing of ceramic materials and structures with optimal mechanical properties involves formulation of an ink with the desired Hershey-Buckley rheological behavior, optimization of the printing parameters (pressure, speed and printing strategy), and identification of the optimal sintering cycle[13,34,105]. In the conventional process[34,71,74,78,106,107], performance is ascertained by microstructural analysis and mechanical testing (generally via compression) on centimeter-scale samples, often in bulk form or woodpile architecture. In typical DIW systems, this involves synthesis and rheological characterization of multiple batches of ink, as well as several sintering cycles, a long and tedious process that is not well suitable to test the large number of samples required for proper statistical analysis of ceramic

strength. Furthermore, tensile or compressive fracture of a ceramic sample containing a multi-scale distribution of defects (pores, cracks, potential inter-layer delamination…) is a complex process, not easily amenable to the extraction of meaningful and well-defined mechanical properties. By contrast, three-point bend testing is much less sensitive to internal flaws.

Here we propose a novel high-throughput testing procedure that allows extraction of statistical information on the strength of DIW ceramic components, accounting for the effect of defects at multiple scales, using a very small amount of material. We use this method to rapidly characterize five different ceramic materials, down-selecting two for optimal mechanical properties, and use the results of this investigation to design and demonstrate architected structures with bending strength 50% larger than monolithic materials at 20% lower weight. While the results are presented on alumina-based ceramics in the context of DIW, the method proposed herein is general and can provide rapid statistical data on the strength of virtually any ceramic material, for application to any processing technology.

4.2 Methods

4.2.1 Raw materials

In this work, five different ceramic materials were investigated: (1) pure alumina (Al_2O_3); (2-3) zirconia-toughened alumina (ZTA10 and ZTA20), with 10 and 20 vol% zirconia (ZrO_2), respectively, and (4-5) titania (TiO_2) and magnesia (MgO)-doped alumina (TDA and MDA), with 0.4 wt% and 0.25 wt% of dopant, respectively. Three powders were used: Grade A-16 SG alumina powder, with an average reported particle size of 0.5 μm (Almatis, USA); TZ-3Y-S partially stabilized zirconia powder with 3 mol% Yttria (TOSOH INC, USA), with an average reported particle size of 90 nm; magnesia powder (US Research Nanomaterials Inc, USA); and titania powder (US Research Nanomaterials Inc, USA).

4.2.2 Ink preparation

All materials were produced by DIW of an appropriately designed viscoelastic ink, followed by sintering. The ink is composed of four materials: (i) Ammonium polyacrylate (NHPA) (Darvan 821A, R.T. Vanderbilt Company, USA), used as a dispersant, (ii) 1-ethenyl-2-pyrrolidinone (PVP) homopolymer (Sigma-Aldrich, USA), used as a rheology modifier, (iii) DI water, used as solvent, and (iv) ceramic powder. The based alumina ink was carefully optimized for printability in our earlier study[105] and was used here with no modification. The process consisted of three steps: (1) the alumina powder was mixed with a solution of DI water and dispersant in a centrifugal planetary mixer; (2) the resulting ink was subsequently placed in a vacuum chamber to remove bubbles while the viscosity remained low; (3) the rheological modifier was added and the ink was mixed again in the planetary mixer. The weight of the ink was measured before and after each step, and DI was added as needed to compensate for evaporation. For the other inks, the secondary ceramics were added before the primary alumina powder to ensure a good homogenization of the minority phase while the viscosity of the ink is low. The new chemical compositions were created by removing the same volume percent of alumina as the added volume percent of secondary ceramic. As the difference in size, shape and physical properties (e.g., hygroscopicity) among the different powders may alter the rheology of the ink, the volume ratio of ceramic powder to DI water was slightly adjusted for each ceramic powder composition, until we observed a similar consistency and printing parameters as for the previously optimized base ink.

4.2.3 Direct Ink Writing procedure

All samples were printed using a custom Direct Ink Writing system, composed of a 3-axis motion stage (Aerotech, USA) and a pneumatic dispenser (Ultimus V, Nordson EFD, USA). More details can be found in the previous chapter. The substrate was coated with Teflon spray to help

the release of the samples after printing. All parts were printed using a 580 µm nozzle diameter. A new nozzle was used for each print to ensure consistent quality of the printed parts and to avoid premature clogging of the nozzle. Additionally, the distance between the nozzle and the substrate/previous layer was set to be 85% of the nozzle diameter to ensure a good adhesion between the printed layers and to allow the lines to relax after deposition. For the study of the single lines (section 4.3.2), the samples were printed in batches of 25 lines with lengths of 25 mm. A rim was printed around each batch to prevent the warping of the lines during drying. After printing, silicone oil with low viscosity was applied to the samples to slow down the drying process and allow the sample to dry homogenously, further reducing the warping. Finally, at the end of the ink transition from gel to dry solid, but before the samples were completely dry, a small weight was applied to the samples to minimize warping. For the multi-line study (section 4.3.3), the printing process was similar to the single-line samples, except that the batches were reduced to 5 to 10 samples. In section 4.3.4, the multi-track samples were scaled up to bulk samples and architected sandwich structures, with as-printed dimensions of approximately 42 mm x 4 mm x 3 mm. The printing direction for the bulk sample was the same as the multi-track to ensure consistency. The sandwich structures consisted of flat single-layer face sheets and an architected core with woodpile topology. The face sheets were printed similarly to the multi-track samples. For the bulk samples, the lines were printed with an overlap of 20% to ensure good inter-line contact. For the first (bottom) layer of the sandwich samples, the inter-line overlap was set to 0%, to provide the ink with sufficient time to stabilize, and the layer height was set smaller than the nozzle diameter, resulting in wider lines. However, for the final (top) layer, it was observed that an overlap of 20% would result in a similar layer quality as the bottom layer. This change was critical to ensure symmetry and avoid sample warping upon drying.

4.2.4 Sintering

All samples were sintered using the same conditions, inside a box furnace (Thermcraft, USA) in air environment. The sintering cycle consisted of an initial ramp to 700 °C at 5 °C/min, followed by a dwell for 1 hr to burn off the polymer. Subsequently, a second ramp was performed up to 1,100 °C at 5 °C/min, followed by a dwell for 1 hr. Finally, the temperature was increased in 100°C increments at a rate of 1 °C/min followed by a 1 hr dwell, until reaching 1,500 °C for a last 1 hr dwell. This multi-step sintering procedure was chosen to avoid warping of the samples, which was observed to occur at temperatures higher than 1,100 °C under faster heating. After the final dwell, the furnace was cooled down to room temperature at a rate of 5 °C/min. Some weight was applied onto the samples during the sintering cycle to further prevent warping upon sintering.

4.2.5 Material Characterization

The fracture surfaces of the samples were imaged using an Olympus DSX10-UZH digital microscope (Olympus, Japan). The grain size of the alumina and ZTA samples were investigated from fracture surfaces using a FEI Magellan 400 XHR scanning electron microscope (SEM), operated at 3 kV. Computed tomography (CT) scans were performed using VJ Technologies micro-CT scan with a voltage of 150 kV, a power of 10 W and a resolution of about 10 μm. The focus of material characterization was placed on the alumina and ZTA10, as these materials were down-selected for the following part of the study.

4.2.6 Mechanical Measurements

Three-point bending tests were performed on the single tracks and single-layer samples using a Q800 dynamic mechanical analyzer (DMA) (TA instruments, USA) with a 18 N load cell. The DMA was used in displacement control with a rate of 60 μm/min. The remaining samples were tested using an Instron ElectroPuls load frame (Instron, USA) with the same displacement rate.

The flexural strength was calculated from beam theory as $\sigma_f = \frac{My}{I}$, with y the distance from the center of mass to the tensile face of the sample, $M = \frac{FL}{4}$ the moment at the center of the beam, L the inter-span distance and I the moment of inertia. As the shape of the cross section of the samples is irregular, I and y were extracted from binarized images of the fracture surface, obtained from optical images via ImageJ processing, via a MATLAB code implementing the method proposed by Borislav *et al.*[108] For the studies of the single tracks, multi-tracks and bulk/structure samples, 20, 10 and 6 samples were tested, respectively. The distribution of flexural strength from nominally identical samples was quantified with Weibull statistics[109]. According to Weibull theory, the probability of failure, P, of a brittle material scale with the applied stress as $P = 1 - \exp(-(\sigma - \sigma_0)^m)$, with σ_0 the strength parameter (expressing the most likely fracture strength of the material) and m the Weibull modulus. After the fracture strength of each sample in the population is extracted, a plot of $\ln\{\ln[1/(1-P)]\}$ versus σ can be fitted to a line of slope m. A large value of m denotes a narrow distribution of strength.

For the analysis of the fracture surface, the side of the sandwich samples was imaged. Using those images, the fracture angle was measured by taking the angle between the bottom and the fracture surface of the samples as shown in Figure 4.11 and Figure 4.12. Furthermore, the same images were used to measure the length of the fracture by tracking of the edge of fracture surface. Then, the angle and the length were correlated to the load at breaking.

4.3 Results and Discussion

4.3.1 A multi-scale high-throughput procedure for statistical analysis of ceramic strength

The development of DIW strategies for printing of ceramic materials and structures with optimal mechanical properties involves formulation of an ink with the desired Hershey-Buckley

rheological behavior, optimization of the printing parameters (pressure, speed, and printing strategy), and identification of the optimal sintering cycle. In the conventional process [34,71,74,78,106,107], performance is ascertained by microstructural analysis and mechanical testing (generally via compression) on centimeter-scale samples, often in bulk form or woodpile architecture. In typical DIW systems, this involves synthesis and rheological characterization of multiple batches of ink, as well as several sintering cycles, a long and tedious process that is not well suitable to test the large number of samples required for proper statistical analysis of ceramic strength. Furthermore, tensile or compressive fracture of a ceramic sample containing a multi-scale distribution of defects (pores, cracks, potential inter-layer delamination…) is a complex process, not easily amenable to the extraction of meaningful and well-defined mechanical properties. By contrast, three-point bend testing is much less sensitive to internal flaws.

Here we propose a novel high-throughput testing procedure that allows extraction of statistical information on the strength of DIW ceramic components, accounting for the effect of defects at multiple scales, using a very small amount of material. The procedure, schematically depicted in Fig. 1, consists of the following steps: (1) a ceramic particle-loaded polymeric ink is formulated, synthesized, rheologically characterized, and loaded in a syringe; (2) three families of multiple beam-shaped specimens are DIW printed: single lines, multi-line and multi-line multi-layer samples; (3) this large collection of small samples is sintered; (4) fast 3-point bending tests are performed on all specimens to extract the fracture load; (5) fracture surfaces of all specimens are optically imaged and binarized, to extract detailed information on the cross-sectional shape and enable calculation of the flexural strength (modulus of rupture); (6) a Weibull plot can be rapidly constructed, to extract average strength and Weibull parameter.

By comparing and contrasting the mechanical properties obtained at the single-line level with those extracted on multi-line and multi-line multi-layer samples, an accurate assessment of the role of printing defects at multiple scales can be readily extracted and used to develop printing strategies for large scale complex components.

Here we demonstrate this multi-scale procedure by (i) characterizing the single-line strength distribution for seven different alumina-based ceramic materials, down selecting the two most promising formulations; (ii) investigating the strength distribution of multi-line multi-layer specimens from these two formulations, identifying the effect of printing-induced defects; and (iii) designing a sandwich-type structure that leverages the printing strategies to achieve bending strength larger than for bulk specimens at a fraction of the weight. For this study, about 1,500 samples have been printed, over 300 of which have been characterized in detail.

We emphasize that the ink formulation we present here is compatible with virtually any ceramic powder and, subject to the choice of an appropriate sintering cycle, can be used to print any ceramic material. Sintering small-scale single-line samples is generally very easy and results in high-density ceramics. The important implication is that, although this chapter focuses on the characterization of DIW components, the high-throughput single-line process described here is an extremely fast, versatile, and economical approach for extraction of Weibull parameters for any ceramic system fabricated with any process.

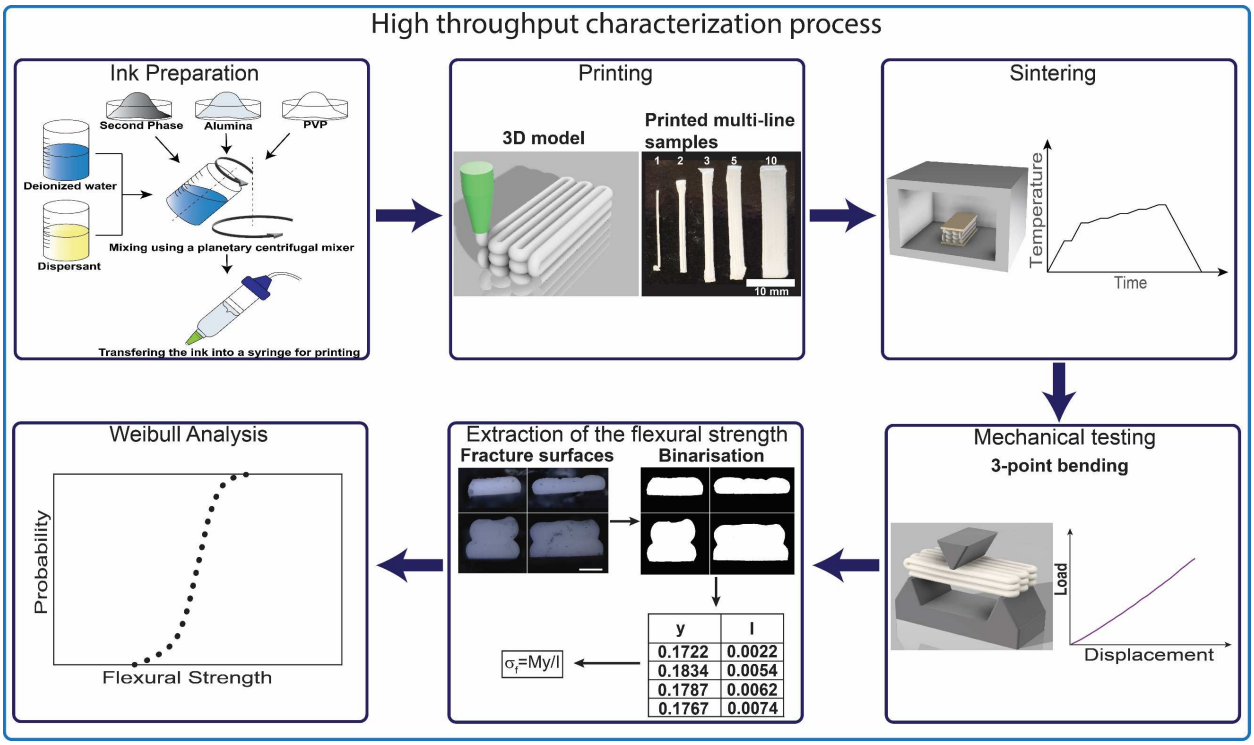

Figure 4.1. *Schematic of the high throughput testing process for the investigation of the mechanical properties of ceramics.*

4.3.2 Statistical analysis of material strength at the single-line scale

Multiple material systems were synthesized and characterized to verify the validity of our proposed high-throughput approach, namely: (1) pure alumina (Al_2O_3); (2-3) zirconia-toughened alumina (ZTA10 and ZTA20), with 10 and 20 vol% zirconia (ZrO_2), respectively, and (4-5) titania (TiO_2) and magnesia (MgO)-doped alumina (TDA and MDA), with 0.4 wt% and 0.25 wt% of dopant, respectively. These material systems have been heavily investigated and their mechanical behavior is well established. Rheologically optimized slurries were prepared for each composition as described in Sec. 4.2.2-4.2.3. More than 20 single-line samples were printed for each composition. All samples were printed and sintered under similar conditions, regardless of composition, as described in Sec. 4.2.3-4.2.4.

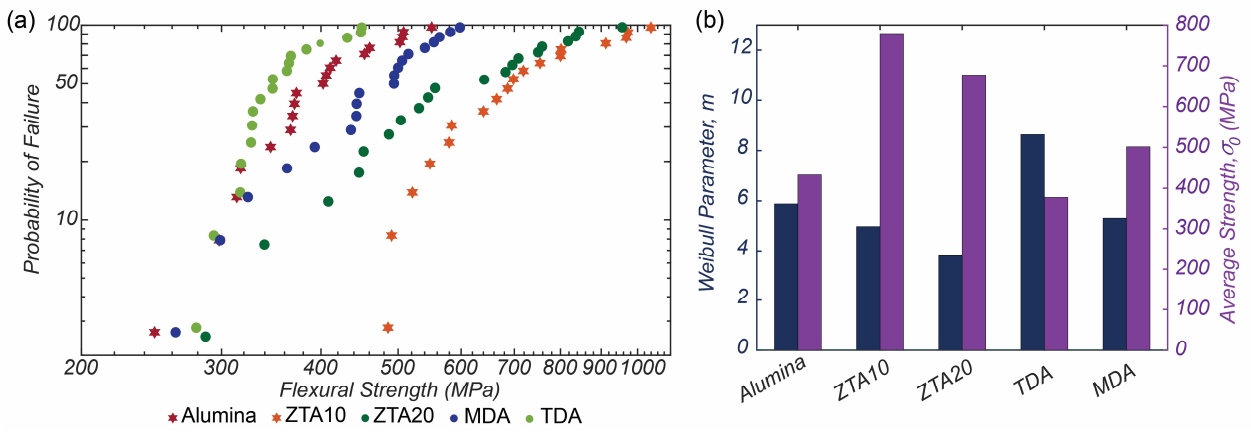

Figure 4.2. *Weibull analysis on single lines for alumina and alumina-based material systems. (a) Probability of failure of the single lines for the related flexural strength. The second moment of inertia and the distance from the center of gravity to the bottom face were calculated from the images of the cross section. Star symbols were used for Al_2O_3 and Al_2O_3/10vol% ZrO_2 as these materials were down-selected for further study. (b) Comparison of the Weibull coefficient (m) and strength parameter (σ_0) for seven material systems.*

Figure 4.2 shows (a) the Weibull distribution of flexural strength for each material system, and (b) the corresponding Weibull coefficient, m and strength parameter, σ_0. As commonly done, we interpret the strength parameter as a proxy for the average flexural strength of the material. The alumina lines have a strength of 432 MPa, in good agreement with the literature and approaching some of the highest values reported for alumina[34,74,79,110–114]. The value m = 5.9 is toward the lower values of m found in the literature[115–117]. The addition of zirconia significantly strengthens the material, as expected from the literature,[118–123] with strength values for ZTA10 and ZTA20 averaging 779 MPa and 677 MPa, respectively. Although ZTA20 has a higher strength than pure alumina, it displays a lower strength parameter than ZTA10. A decline in ZTA strength with increasing ZrO_2 content above ~10 wt% has been observed previously in the literature and is often attributed to grain size effects. If the zirconia grain size reaches a critical value, premature phase transformation from tetragonal to monoclinic zirconia may occur, reducing the potential for transformation toughening and hence depressing sample strength[124–126]. MgO is a well-known

sintering aid for alumina[127,128]. Consistently, the strength of our MDA sample reaches a strength of 501 MPa, a 16% increase from pure alumina, in good agreement with the literature[129], while no significant change in the Weibull modulus was observed. Finally, the addition of TiO_2 as a dopant in alumina reduces the strength of the material system compared to undoped alumina, with our TDA sample strength averaging 357 MPa. A reduction in the strength of Al_2O_3 with the addition of TiO_2 has been observed previously and is commonly attributed to abnormal grain growth and the formation of trapped porosity during sintering[130,131].

4.3.3 From single line to DIW component: statistical analysis of strength of multi-line multi-layer samples

Single printed lines of ceramic material will inherently exhibit higher strength than a large bulk sample, thanks to the confinement of defects and critical flaws. As ZTA10 exhibits the highest flexural strength, we down-select this material for further studies, with pure Al_2O_3 used as reference. Figure 4.3a shows a fracture surface of a representative alumina sample, clearly showing intergranular fracture, and revealing a dense microstructure with an average grain size of 2.2 ± 1.25 μm. The microstructure of the ZTA10 fracture surface is shown in Figure 4.3b: notice that a bimodal grain structure can be observed, with large alumina grains (1.1 μm) surrounded by smaller zirconia grains[132,133].

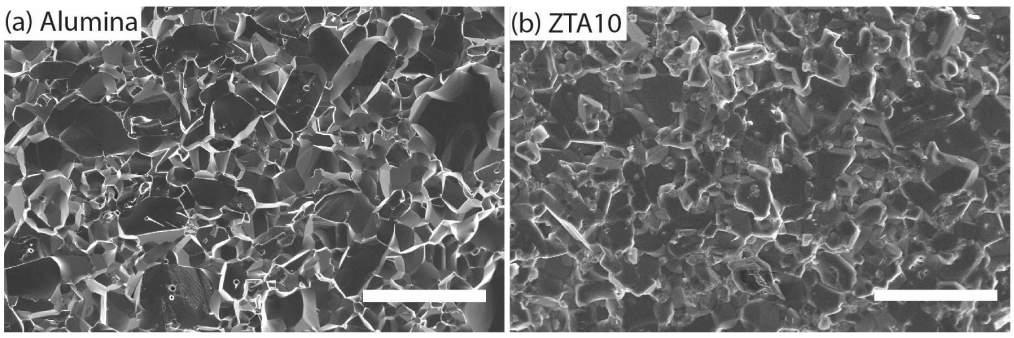

Figure 4.3. *Fracture surface of (a) alumina (scale bar: 10 μm), and (b) alumina with 10 vol% zirconia (scale bar: 5 μm).*

CT scans were performed on a single line for the alumina and ZTA10 in order to characterize the sample porosity and explore its connection to sample strength. Figure 4.4 shows micrographs and CT scans of a representative pure alumina sample (the other two materials showed similar features). The observed pores originate from the bubbles present inside the ink. Quantitative results are reported in Table 4.1. The average pore size is similar across the two different material systems, indicating that the porosity differences are not responsible for the differences in strength. Additionally, the absence of clear stress concentration regions due to their rounded shapes indicates that those pores are unlikely to control the failure of the lines [134–136].

	Pure Alumina	**Alumina/10Vol% ZrO2**
Average diameter (μm)	61	77
Standard deviation on diameter (μm)	4.7	14
Density (%)	98	97

Table 4.1. *Average diameter of the pores within the lines for pure alumina, alumina/10 vol% alumina and alumina/ 10 vol% zirconia. The measurements were performed using CT scanning. The density of the sample was measured using the Archimedes method.*

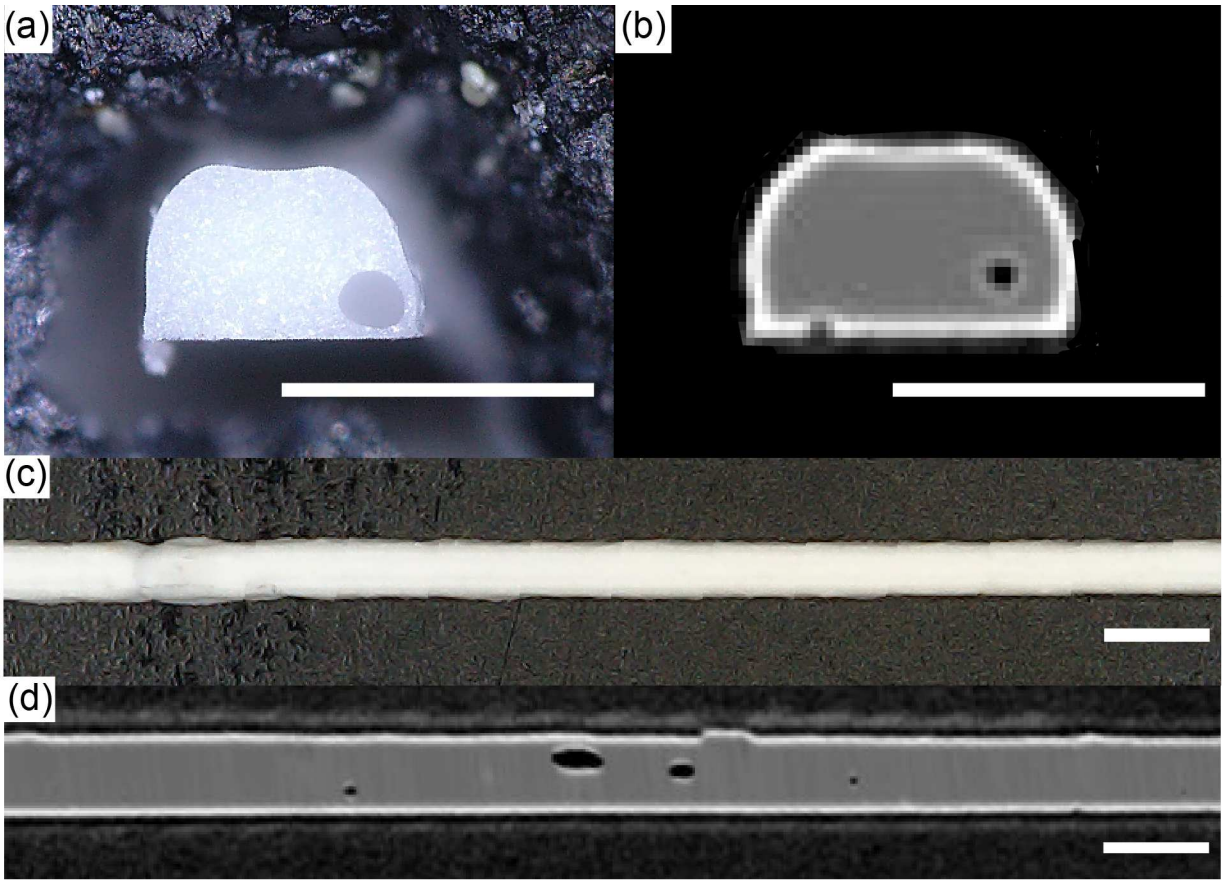

Figure 4.4*. (a and c) Micrograph of the fracture surface of a line and along the line. (b) Slice of the CT scan of (a). (d) CT scan along the line. Scale bar: 0.5 mm.*

Those lines can be considered as a building bock, each of which containing a limited number of defects. When a part is printed, these building blocks are replicated horizontally and vertically to create multi-line multi-layer structures. As a result, the final component will contain two families of defects: those contained within individual building blocks and those formed between building blocks. As the part is scaled up, the likelihood of containing a critical flaw increases, with a consequent decrease in strength. In this section, we print progressively larger samples (1-10 lines and 1-2 layers) and investigate the effect of sample size on flexural strength and Weibull modulus. Flexural strength is extracted from 3-point bending experiments, as in sec. 4.3.2. Figure 4.5 illustrates (a) the 3D model of the ideal geometry of the samples and (b) micrographs of some

fracture surfaces of a few representative samples with different numbers of lines and layers. Pores are present within the prints, which is consistent with our observations on single line specimens. The fracture surfaces of the single line specimens (Figure 4.4a) and the scaled-up samples appear similar. Not surprisingly, the discrepancy between the 3D model geometry and the shape of the as-sintered samples is significant. The top and bottom surfaces of the samples are significantly flattened, which we attribute both to the viscoelastic relaxation of the ink after deposition and the tendency to reduce surface energy upon sintering. This shape change is useful, as it significantly reduces stress concentration. Nonetheless, some areas of concentration still remain, as shown in Figure 4.5b (dashed red circle).

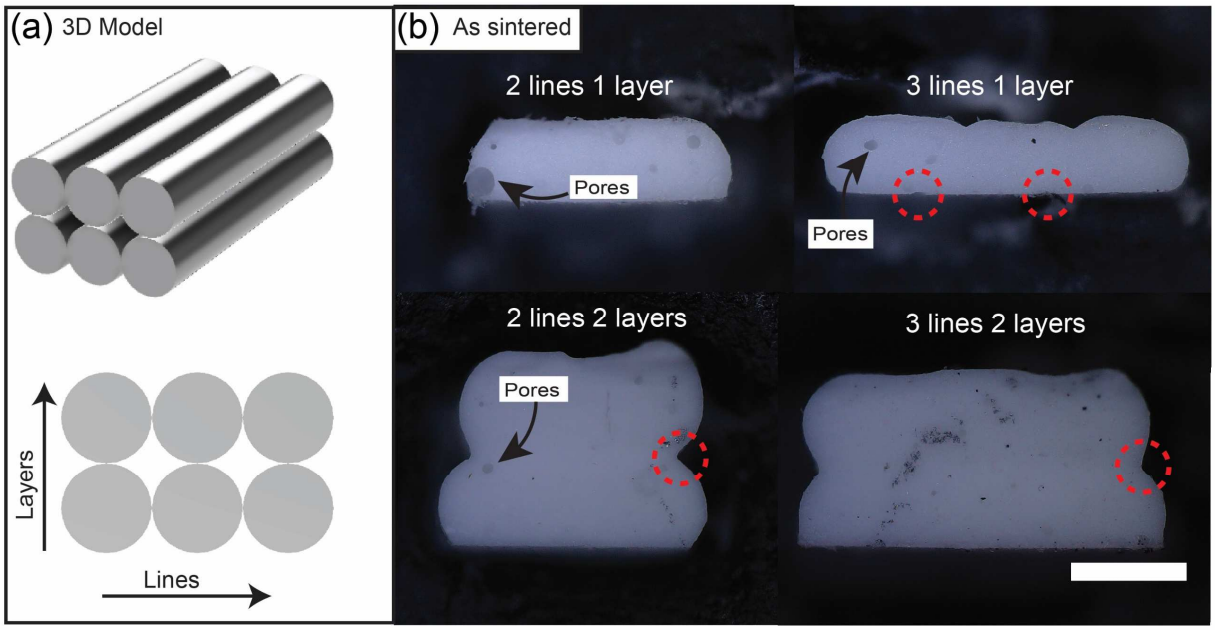

Figure 4.5. *(a) 3D model of a 3-line 2-layer sample as it was programmed for printing. (b) Fracture surfaces of the samples after testing. The voids between the lines are filled due to the relaxation of the ink after deposition. The dashed circles show areas of potential stress concentration. Scale bar: 500 µm.*

The Weibull diagrams and the evolution of average strength and Weibull modulus with the number of lines and layers is depicted in Figure 4.6 and Figure 4.7, for the pure alumina and the

ZTA10 materials, respectively. Bulk samples consisting of 10 lines and 6 layers were also printed for comparison.

For pure alumina (Figure 4.6), the average strength decreases with increasing the number of lines and number of layers, until a plateau in strength is reached at 5 lines. While single-line specimens are clearly the strongest, all multiple line samples have relatively similar strength (10-line single-layer specimens have a strength of 375MPa, 13% lower than the single line value), indicating the quick emergence of a plateau. The effect of number of layers is more pronounced, with bulk specimens (6-layers) exhibiting a strength of only 200 MPa, over 54% lower than single-layer specimens with the same number of lines. With the exception of a few outliers, the Weibull modulus generally increases with the number of lines for single-layer specimens (from *m=6* to *m=9*) and decreases with the number of lines for 2-layer specimens (from *m=6* to *m=4*). These results can be rationalized as follows. In single-layer specimens, printing multiple lines introduces *interline* defects in the tensile region (see Figure 4.5b), which act as stress intensification points and reduce the strength of the sample. At the same time, spreading the load over a wider beam reduces the deleterious impact of the occasional critical pore *within singe lines* (see Figure 4.5b), reducing scatter and increasing the Weibull modulus. For 2-layer samples, the probability of introducing deleterious defects between layers (in particular at the diamond-shaped intersections at two lines and two layers) increases with the number of lines, causing a reduction in both the average strength and the Weibull modulus. The further significant decrease in strength from a 2-layer sample to a 6-layer (bulk) sample can be explained by the nature of the bending test: as the number of layers increases, the interlayer surface defects (see red circled regions in Figure 4.5b) move progressively closer to the region of maximum tensile stress in the sample (the bottom surface), playing a more dominant role on controlling sample strength.

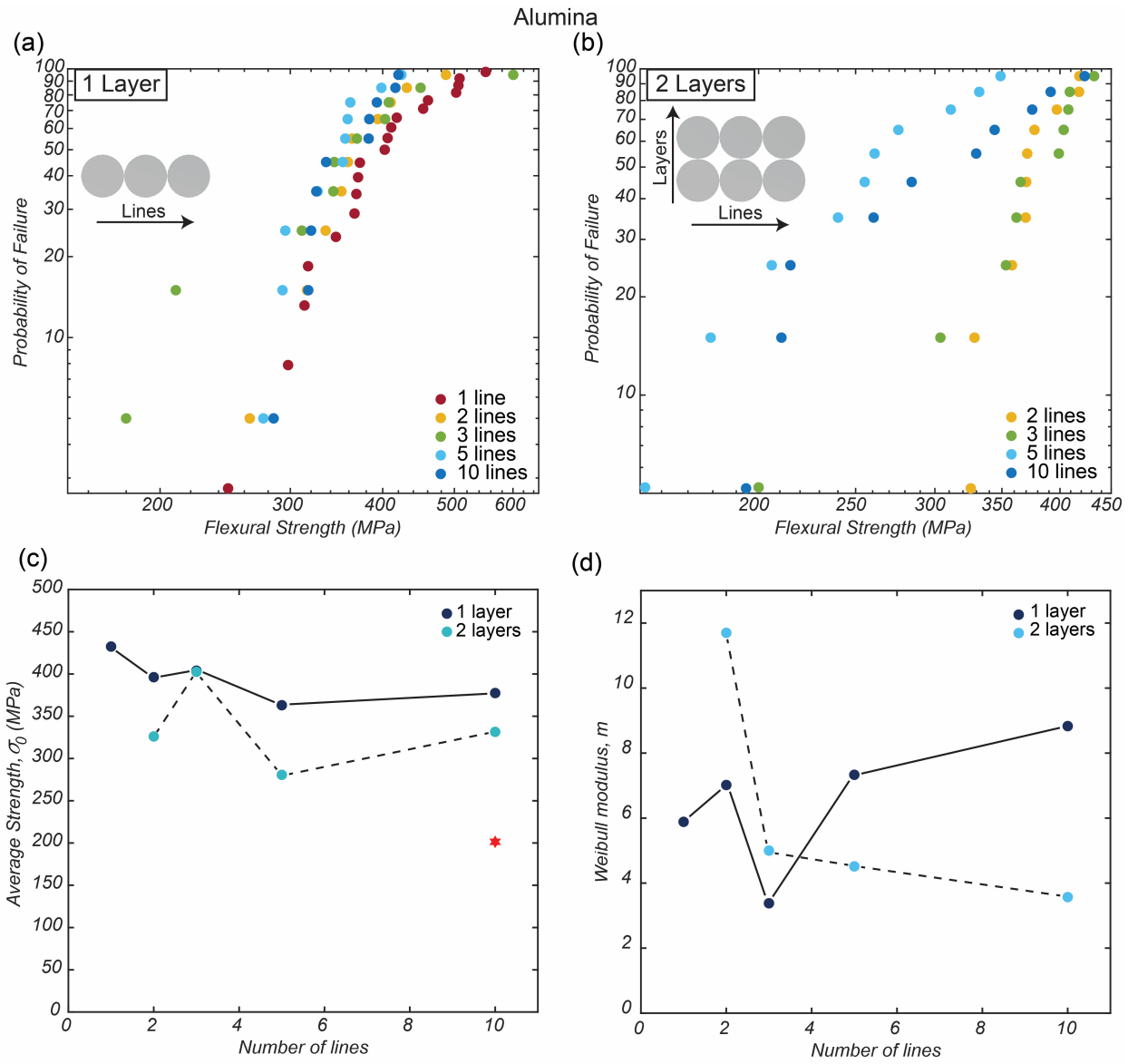

Figure 4.6. *Effect of the increase of lines and layers on the Weibull analysis of alumina samples. The relationship between the probability of failure and the flexural strength with the increase of the number of lines for (a) 1 layer and (b) 2 layers. The Weibull coefficients, (c) σ_0 and (d) m, versus number of printed lines is shown for 1 and 2 layers. The red star represents the average strength of the bulk sample measured in Sec 3.4*

For ZTA10 (Figure 4.7), the strength drops significantly when a second line is added, but the results stabilize thereafter, to 482 - 529 MPa for the 1-layer samples and 385 - 454 MPa for the 2-layer samples, respectively. The 10-line 2-layer sample is still 38% stronger than the bulk sample. We note that the overall trend between strength and line number in the ZTA10 samples is similar

to what is observed in our alumina samples. However, there is a significant drop in the strength between 1 line and 2-line ZTA10. We attribute this to the presence of the transformation toughening ZrO_2 phase in the ZTA10 material, as well as the lack of critical defects in the single line structure. However, the ZTA structures with two or more lines possess interline defects as well as regions of potential stress concentration at the surface, leading to mechanical failure dominated by a critical defect. No clear trend is observed with the Weibull modulus, which oscillates between $m=4$ and $m=10$ for all sample geometries.

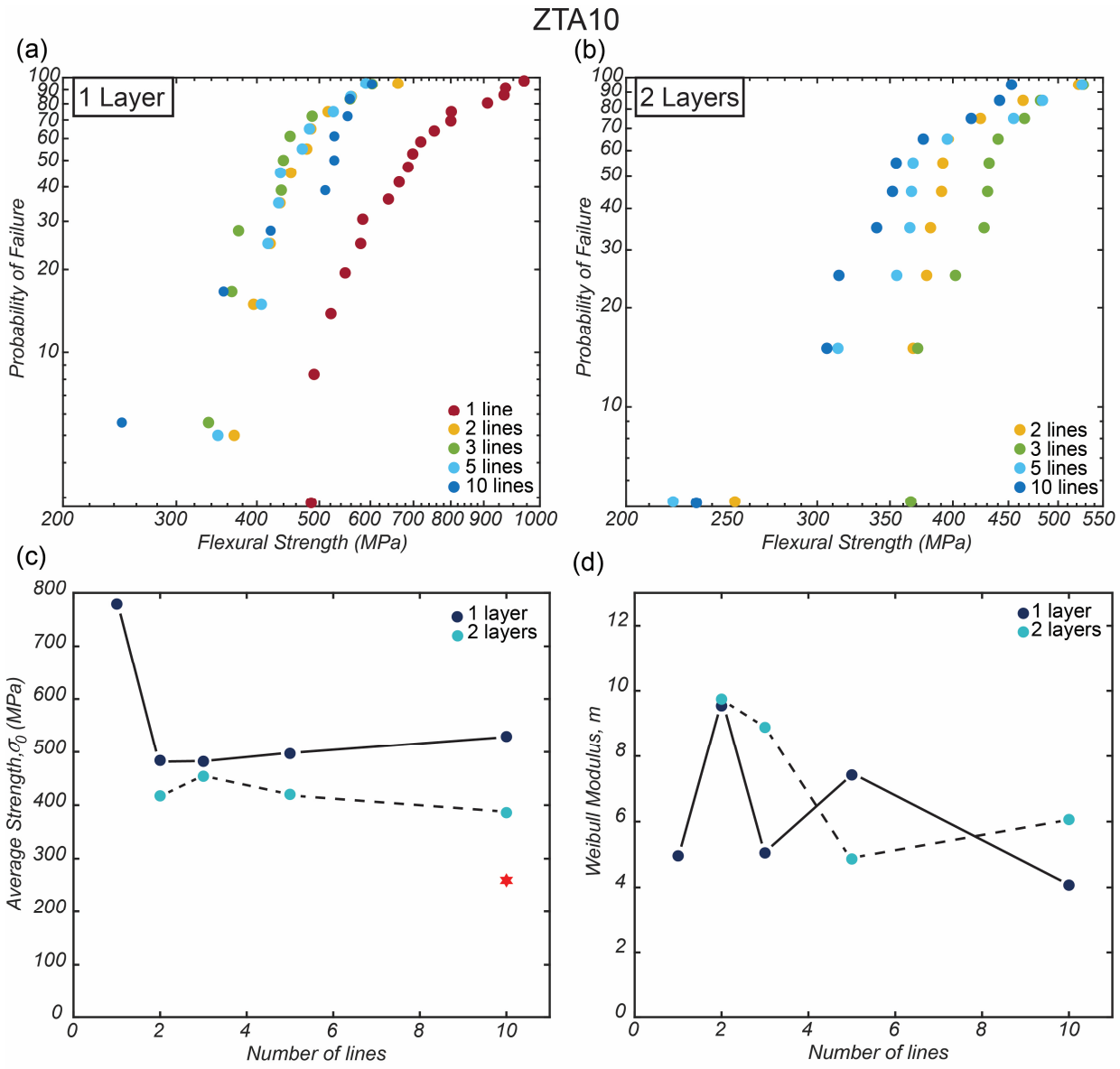

Figure 4.7. *Effect of the increase of lines and layers on the Weibull analysis of ZTA10 samples. The Relationship between the probability of failure and the flexural strength with increase of the number of lines for (a) 1 layer and (b) 2 layers. The Weibull coefficients, (c) σ_0 and (d) m, versus number of printed lines is shown for 1 and 2 layers. The red star represents the average strength of the bulk sample measured in Sec 3.4*

4.3.4 Design of an architected structure with exceptional bending strength

The results in sec. 2.2-3 clearly illustrated that (1) individual alumina and ZTA10 lines display excellent strength with fairly high Weibull modulus, in spite of the residual porosity, and that (2) a knock-down in bending strength is associated with DIW sample scale-up, particularly related to

increasing the sample thickness (number of layers). Here we capitalize on these results to design ceramic structures that sandwich an architected single-line woodpile core between single-layer-thick face sheets. These structures are tested in 3-point bending and compared to monolithic bulk samples (10 lines wide and 6 layers thick). Figure 4.8 displays the flexural strength of all samples as a function of their relative density. The relative density is defined simply as volume of ceramic material divided by the volume of the structure (clearly, for bulk samples, the relative density is equal to 1). A number of interesting results emerge:

(i) Both the monolithic bulk samples and the sandwich structures show significant scatter in their strength, varying between 120 and 320 MPa for bulk structures and between 120 and 460MPa for the sandwich structures.

(ii) ZTA10 samples are generally stronger than alumina samples, in good agreement with the results of sec. 4.3.2.

(iii) The bending strength of sandwich structures generally increases with sample relative density, as expected from basic structural considerations [2,5,28,29,67,73].

(iv) ZTA10 sandwich structures show much higher strength (250 – 460 MPa) than alumina structures (120 – 225 MPa), but with higher standard deviation. This is consistent with strength and Weibull modulus data for single layer samples (Sec. 4.3.3), indicating that face sheet response controls the mechanical behavior of the sandwich structure.

(v) Remarkably, two ZTA10 sandwich structures show 45% higher bending strength than their fully dense counterparts, despite being 20% lighter. This demonstrates that judicious introduction of a significant amount of porosity in a ceramic sample may improve mechanical properties, in contrast with generally established design principles.

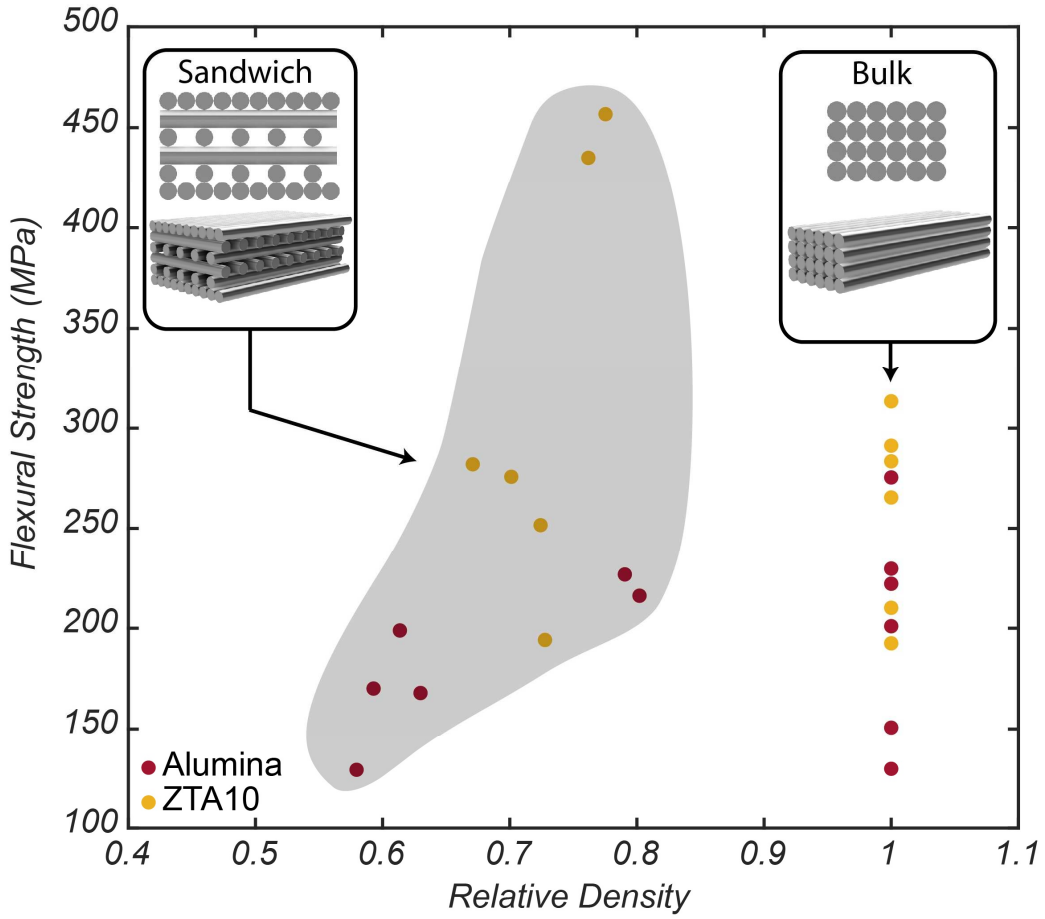

Figure 4.8. *Relationship between maximum flexural strength and the relative density of alumina and ZTA bulk and sandwich structures.*

To correlate these results with differences in microstructure, in Figure 4.9 we report optical images of representative fracture surfaces for sandwich and bulk structures, for both materials; Figure 4.10 shows 3D computed tomography (CT) reconstructions. Notice that while all structures clearly show presence of near-circular pores (introduced during ink preparation and/or extrusion of individual lines), the bulk structures clearly also show smaller and sharper pores between the lines and large cracks and delamination fronts that span multiple printing lines, likely introduced during the sintering process. This clearly correlates with the superior mechanical performance of the sandwich structures and demonstrates that architecting a ceramic material so that it is locally

only one line-thick improves sintering and densification, avoids the occurrence of sharp deleterious cracks and results in significantly higher strength.

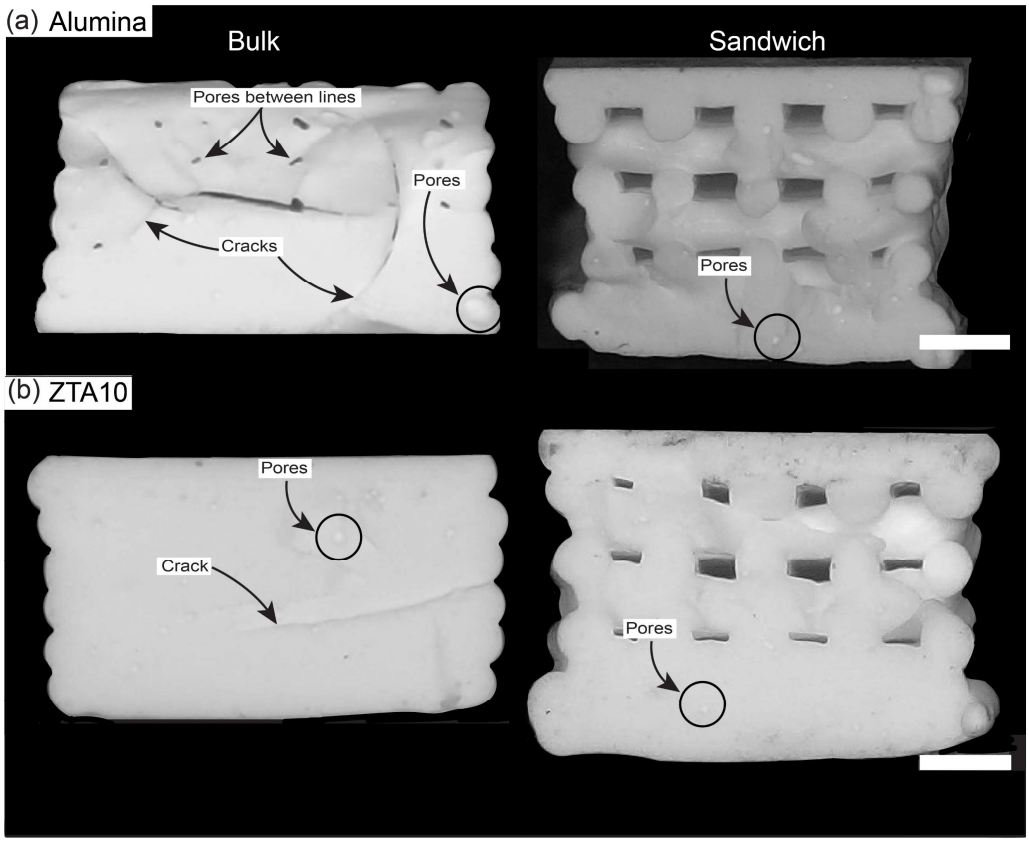

Figure 4.9. *Fracture surface of (a) the alumina and (b) ZTA bulk and sandwich structures. Several types of defects can be identified in the bulk samples such as cracks, pores between the lines which are not present in the sandwich samples. Only pores from the ink preparation are present in all samples. Scale bar: 1 mm.*

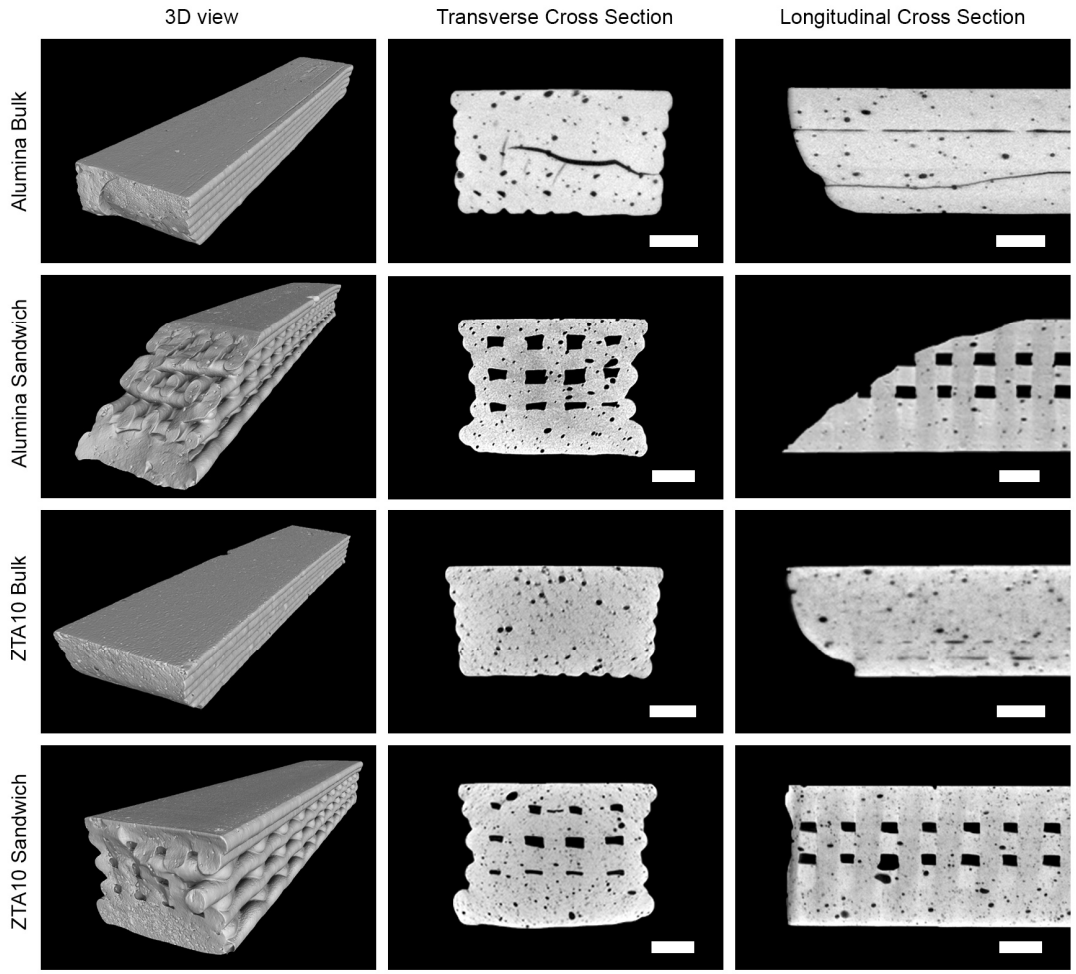

Figure 4.10. *CT scans of the bulk and sandwich structures for the alumina and ZTA10, obtained from post-mortem samples. Scale bar: 1 mm.*

The failure behavior of the sandwich structures was further investigated. Figure 4.11a shows load-displacement curves for the alumina samples extracted from the 3-point bending experiments, juxtaposed with optical images of the post-mortem samples (color coded) in Figure 4.11b. The differences in sample stiffness simply correlate with differences in relative density (Figure S3.1). Notice that the strongest samples display a straight crack propagation path, while the weaker samples fractured at a lower angle. These observations are quantified in Figure 4.11c-d, where bending strength is plotted against fracture surface angle and crack path length. We interpret these results in terms of the location of critical flaws. If no major flaw is present, the sample will fail

starting from the largest tensile stress point, immediately below the center loading anvil, and proceed vertically toward the loading anvil. Conversely, if a major flaw is present on the tensile surface near (but not immediately below) the anvil, fracture can initiate prematurely at that location; once the crack leaves the face sheet, it needs to repeatedly stop and restart as it travels through the porous woodpile core; in doing so, it will naturally move towards the center anvil, following the regions of maximum stress. As a result, stronger samples fail with a straight vertical crack, while weaker samples will fail along a diagonal crack path, consistently with the results in Figure 4.11.

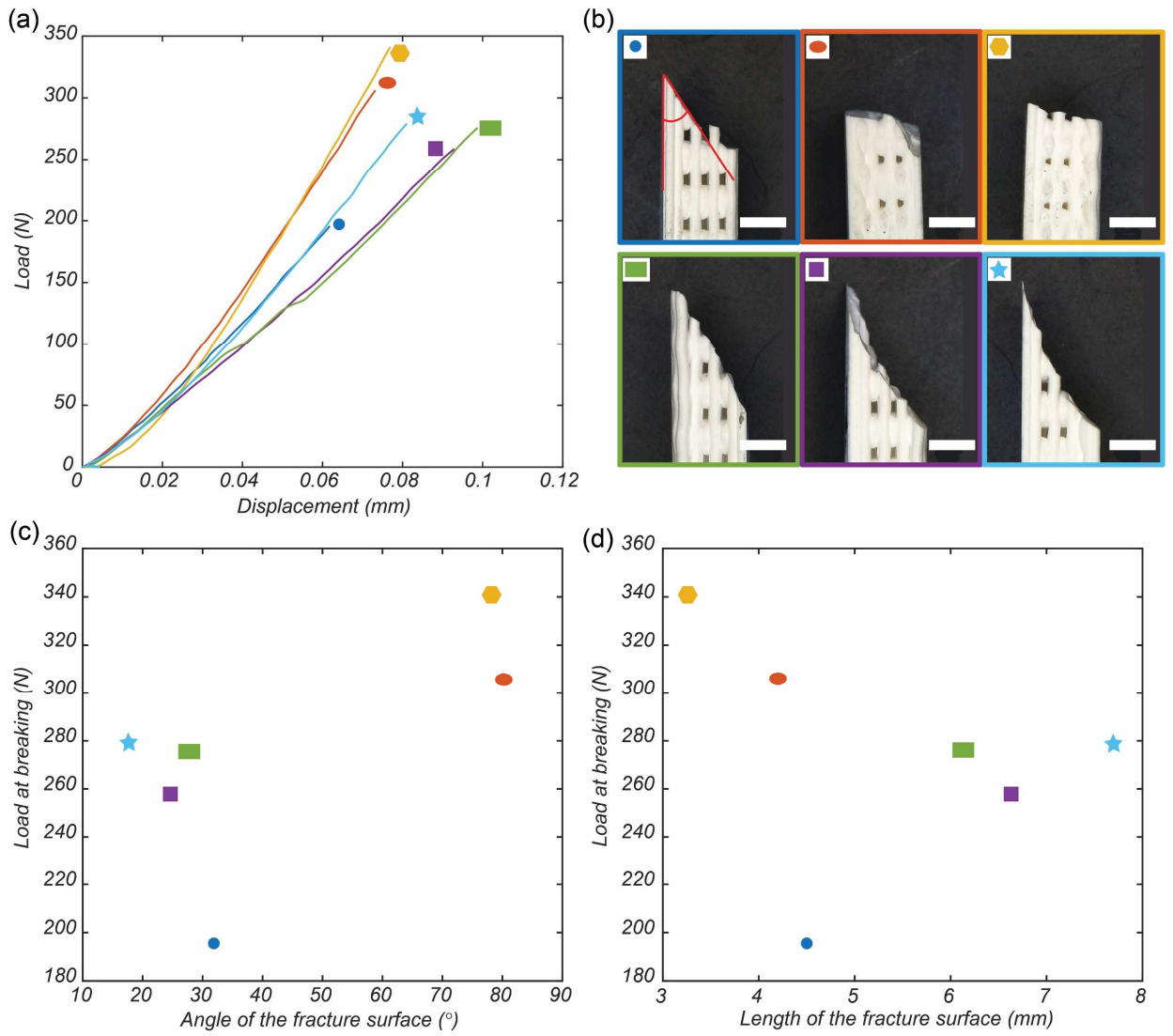

Figure 4.11. *Analysis of the failure of the alumina sandwich structures. (a) Load versus displacement of the alumina samples in a 3-point bending test. (b) Side views of the fracture surface of each sandwich samples tested. Load at breaking versus (c) angle and (d) length of the fracture surface. Scale bar: 2 mm.*

A similar analysis was performed on the ZTA sandwich structures (Figure 4.12). The stiffness of all samples is fairly similar, consistently with smaller deviations in relative density relative to the alumina samples (Figure S3.2). Interestingly, the fracture surfaces of all samples are also very similar, with most cracks following a nearly vertical line. However, the measured load at breaking values generally increases with increasing fracture length. We attribute this to a crack growth

resistance effect in our ZTA samples. ZTA is well known to exhibit crack growth resistance due to the presence of the transformation toughening ZrO_2 phase [137]. The observed crack length will be determined by the distance between the center loading anvil and the critical defect. The further the critical defect is from the center loading anvil, the longer the crack length will be. As the crack path gets longer, the transformation toughening, and crack growth resistance will lead to an increase in the strength of the structures[138,139].

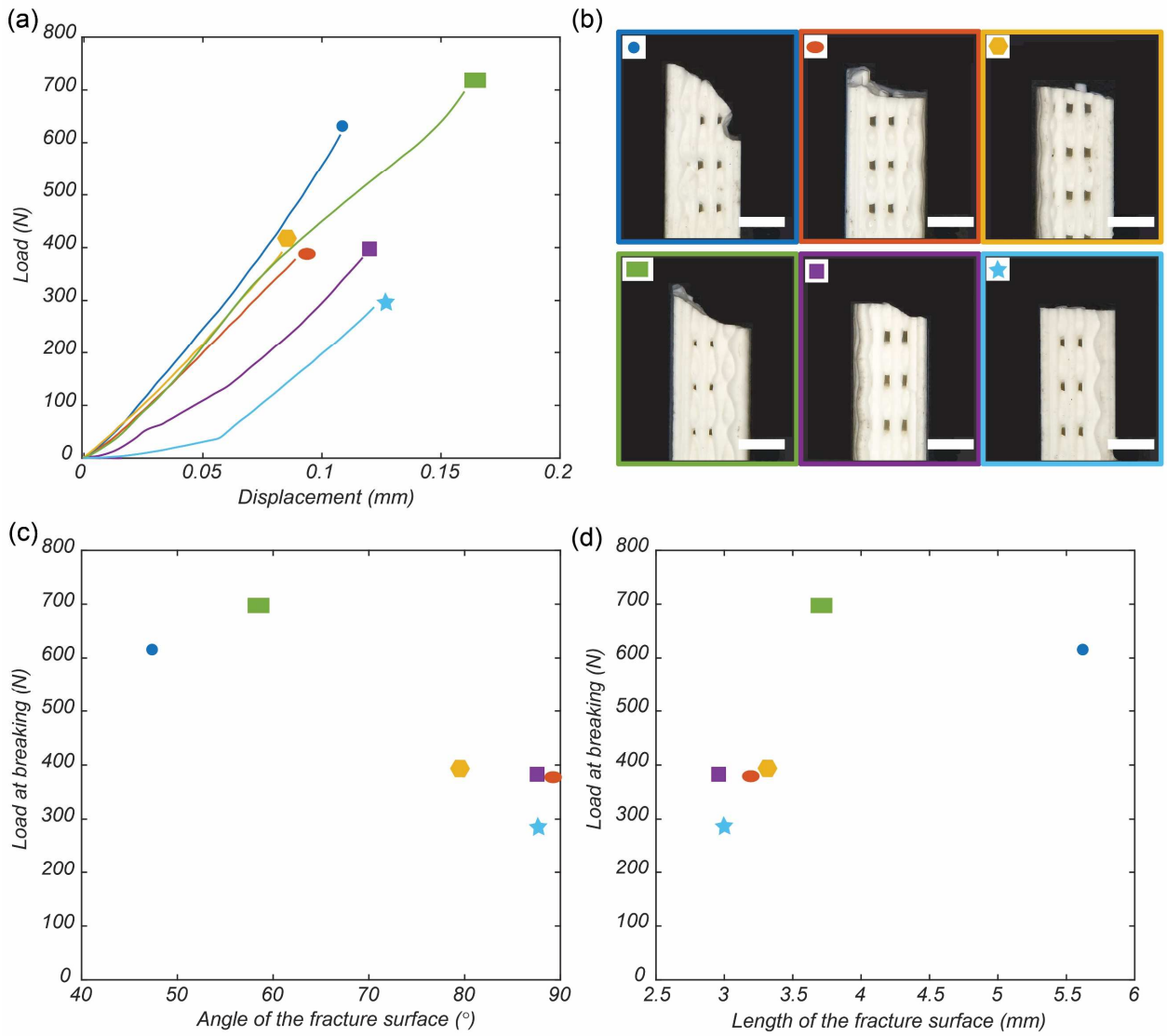

Figure 4.12. *Analysis of the failure of the alumina sandwich structures. (a) Load versus displacement of the alumina samples in a 3-point bending test. (b) Side views of the fracture surface of each sandwich samples. Load at breaking versus (c) angle and (d) length of the fracture surface. Scale bar: 2 mm.*

4.4 Conclusions

A novel multi-scale high-throughput procedure for statistical analysis of ceramic strength was introduced, consisting of preparation of a ceramic-loaded polymeric ink with printable rheology, DIW printing of multiple single-line, multi-line and multi-line / multi-layer samples followed by

sintering, and rapid mechanical testing of all samples by 3-point bending followed by post-mortem geometric characterization of the cross-section to extract average strength and Weibull modulus.

We demonstrated this procedure on 5 well-known ceramic formulations and identified pure alumina and alumina / 10 vol% zirconia (ZTA10) as the most promising materials. ZTA is consistently stronger (779 MPa) than alumina (432 MPa) in single line form, while having a lower Weibull modulus, in good agreement with some of the best literature data. While multi-line and multi-layer samples were consistently weaker than single lines, increasing the number of layers resulted in a more dramatic knock-down on properties, whereas the effect of increasing the number of lined reached a plateau very quickly (2-3 lines).

These results were exploited to design a ceramic structure with single-layer face sheets sandwiching a woodpile core, capitalizing on the strength of individual single-line building blocks. The result is a ZTA10 sandwich structure that is almost 50% stronger than a solid sample of the same material, while being 20% lighter. This simple result shows that judicious introduction of porosity in ceramic materials – combined with the exploitation of size effects, may be a viable approach for the design of high-strength low-density materials.

While this work has focused on DIW structures, suitable inks can be produced and sintered to full densification with virtually any ceramic powder; we conclude that the high-throughput methodology introduced herein is a versatile approach for the characterization of any ceramic material, regardless of the processing route.

5. Direct Ink Writing of alginate/pluronic-based scaffolds for cartilage engineering

5.1 Introduction

Microtia is a congenital condition including diverse malformations of the external ear[140]. The complex shape of the ear, the need to perform interventions at an early age, and the nature of the cartilage tissue make plastic surgery extremely challenging. Several techniques have been developed[141,142], but they are facing many limitations, including invasiveness, excess pain, tissue necrosis, infection, etc. Novel approaches based on tissue engineering have been proposed to address those limitations[143–145]. One method of cartilage engineering consists of the utilization of mesenchymal stem cells (MSCs) co-cultured with chondrocytes[146]. Adipose-derived stem cells (ADSCs) are MSCs that are abundant in fat tissue and can be collected with minimal donor site morbidity. Allograft adipose matrix (AAM) has been shown to serve as a scaffold that supports chondrogenesis when it is seeded with ADSCs and chondrocytes [147,148]. The combination of cartilage engineering and bioprinting provides an alternative solution to traditional surgical intervention, as it allows the fabrication of complex shapes and can limit the invasiveness of the approach. A multitude of additive manufacturing approaches has been demonstrated for bioprinting, such as material jetting[149–151], stereolithography[152–154], material extrusion[155–158]. Direct Ink Writing (DIW) is an extrusion based additive manufacturing technique consisting of the deposition of an ink (slurry or gel) in a layer-by-layer manner. Direct Ink Writing is extremely suitable for bioprinting thanks to its vast materials palette, including cell-loaded inks.

In this study, we use DIW to create a micro-architected scaffold made of AAM for cartilage engineering. AAM is well suited for the attachment and survival of ADSCs, which upon mixing with chondrocytes will boost chondrogenesis. The process for creation of an ear-shaped cartilage in vitro includes 3 steps: (i) an AAM-containing bioink is designed to possess the right rheological

properties for DIW; (ii) an ear shape scaffolds is printed using the bioink; (iii) the scaffold is cultured in a solution containing ADSCs for ~8 weeks. After about 8 weeks in culture, chondrogenesis is assessed. We hypothesize that careful design of the multi-scale porosity within the scaffold should enable the cells to travel easily through the entire structure. After months, we expect the AAM to be consumed, and the cells turning into cartilage.

5.2 Materials and methods

5.2.1 Raw materials and ink preparation

The ink is composed of four materials: (i) Pluronic F-127 (Sigma Aldrich, USA), (ii) Sodium Alginate (Sigma-Aldrich, USA), (iii) Adipose Allograft Matrix (AAM, MTFbiologics, USA), which is made of decellularized fat from a cadaver, or Extra Cellular Matrix (ECM), and (iv) DI water. First, pluronic was mixed with cold DI water at 2,000 rpm for 1 minute, using a centrifugal planetary mixer (AR100, Thinky, USA). After mixing, the solution was cooled down to 5°C to reduce the viscosity of the pluronic solution; this step allowed elimination of most bubbles created by mixing, as they more easily raise to the top in a low viscosity solution. Then, ECM or AAM was added to the solution and mixed at 2,000 rpm for 1 minute. Finally, sodium alginate was mixed into the solution at 2,000 rpm for 1 minute. At each step, the weight of the solution before and after mixing was measured, and DI water added as needed to compensate for evaporation. Finally, the ink was transferred into a syringe using a flat spatula to reduce formation of bubbles.

5.2.2 Rheology

The rheology of the bioinks was investigated using a DHR-3 rheometer (TA Instruments, USA) equipped with a 25 mm sand-blasted parallel plate geometry with a gap of 300 μm. A flow ramp was performed in stress control from high to low stresses to better capture the low shear rates and limit errors. Subsequently, amplitude sweep measurements at a frequency of 1 Hz were

performed to extract the storage and loss moduli as a function of the oscillation stress. Finally, creep tests were performed at low stress within the Linear Viscoelastic Regime (LVR) and at high stress. A temperature of 20 °C was maintained throughout the entire test.

5.2.3 Direct Ink Writing (DIW) procedure

All parts were printed using a custom Direct Ink Writing printer, consisting of a 3-axis motion stage (Aerotech, USA) and an air-powered fluid dispensing system (Ultimus V, Nordson EFD, USA). The printer had a volumetric accuracy of 10 μm^3 and a maximum build volume of 10 cm x 10 cm x 10 cm. The dispensing system provided pressure up to 689 kPa. Woodpile structures were printed by programming the G-code in the Aerobasics environment from a modified version of the code provided in the technical note by William et al. [77] .Woodpile structures were printed by layer-by-layer deposition of the lines, with a change of printing direction by 90 degrees for each layer. The geometry of the woodpile structures was defined by three parameters: the line diameter, the gap between the lines, and the height layer. All prints were performed using a 580 μm nozzle diameter as a good compromise between accuracy and ease of printing, and a gap equal to the line diameter was chosen to create channels large enough for cells without compromising structural integrity. The height between the tip and the substrate/previous layer was set to be 85% of the nozzle diameter to ensure good contact of the layer. The dimensions of the samples were 10 mm x 10 mm x 5 mm. A publicly available 3D model of an ear (from www.thingiverse.com) was printed using the slicing software Ultimaker Cura, controlling the internal porosity. Finally, all printed parts (ear scaffold, and woodpile structures) were immersed in a solution of 20 wt%/v $CaCl_2$ for 20 minutes to allow the alginate to crosslink.

5.2.4 Material characterization

The microstructure of the samples was observed using a FEI Quanta 3D FEG dual-beam microscope operated at 30 kV. The images were taken under low vacuum (1.3 mbar) with water vapor in the chamber to prevent premature drying of the structures. The chamber was then switched to high vacuum to investigate the microstructure of the dried structures. Computed tomography (CT) scans were performed using a VJ Technology micro-CT scan with a voltage of 200 kV, power of 12 W, and a voxel size of approximately 12 μm. The scans were taken for both wet and dry samples. Finally, FTIR measurements were performed using a Jasco FT/IR-4700-ATR-PRO-ONE spectrometer with a range of 600 cm^{-1} to 4000 cm^{-1}. To collect data after crosslinking, the samples were washed twice with DI water to ensure no contamination.

5.2.5 Cell culture

Auricular chondrocytes (ACs) were isolated from pediatric discarded cartilage tissue after microtia reconstruction (IRB exempt). The cartilage was washed in sterile phosphate-buffered saline (PBS) with 1% penicillin and streptomycin (p/s) (Corning Cellgro; Thomas Scientific, Swedesboro, N.J.). The cartilage was minced and digested in collagenase II (Gibco, Gaithersburg, Md.). The collagenase was neutralized with 10% fetal bovine serum (FBS) (Fisher Scientific, Waltham, Mass.). The digested solution was filtered over a 100-μm nylon mesh (Fisher), and the cell suspension was centrifuged. The cell pellet was resuspended in a commercially available chondrocyte growth medium (PromoCell, St. Louis, Mo.) and grown in a flask until confluent. The cells were frozen after reaching confluence to minimize the passage number for the experiments.

Fat tissue was obtained from healthy individuals undergoing elective liposuction at the Department of Plastic Surgery, University of California, Irvine (IRB 2015-2181). The lipoaspirate

was washed in PBS, digested in collagenase I (Sigma, St. Louis, Mo.), and neutralized using Dulbecco's Modified Eagle Medium (Corning Cellgro) supplemented with 10% FBS and 1% p/s. The digested solution was passed over a 100-µm nylon mesh. After centrifugation, the pellet was resuspended in Dulbecco's Modified Eagle Medium with 10% FBS and 1% p/s. The isolated ADSCs were characterized as previously described by our laboratory[159].

5.2.6 Seeding cells on the scaffolds

The printed AAM scaffolds were UV sterilized. The scaffolds were then rehydrated in chondrocyte medium (PromoCell) overnight. To first test cell adherence and survival, $1x10^6$ ADSCs in 150 µl of chondrocyte medium were seeded on the scaffolds. After an overnight incubation at 37°C in a 5% CO_2 humidified environment, another 350 µl of chondrocyte medium was added. The cultures were then replenished with fresh medium twice a week for 2 weeks. To assess chondrogenesis, the ADSCs and ACs were seeded either alone or together on the AAM as described above. For the co-culture, the ACs and ADSCs were seeded together at a ratio of 1:9, respectively. These scaffolds were cultured for 8 weeks. Scaffolds without cells served as negative controls for both aspects of the study.

5.2.7 Histology

After the culture period, the scaffolds were fixed in paraformaldehyde, embedded in paraffin, and sectioned. The sections were stained with hematoxylin and eosin (HE). For the immunohistochemical analysis, the sections were deparaffinized, rehydrated, and blocked in hydrogen peroxide. Then, a trypsin enzymatic antigen retrieval kit (Abcam, Fremont, CA) was utilized. The subsequent processing was done using the Mouse and Rabbit Specific HRP/DAB (ABC) Detection IHC kit (Abcam) alone with a human type I collagen antibody (Novus Biologicals, Cenntenial, CO) or a human type II collagen antibody (Abcam). Furthermore, the

sections were also stained using Masson's Trichrome to detect overall collagen and Alcian Blue to detect glycosaminoglycans (GAGs). The sections were mounted and imaged at 4X. Representative images are shown.

5.3 Results and Discussion

5.3.1 Ink Preparation

To design the ink, the affinity of the AAM with the solvent was initially tested by itself in DI water, with the goal of limiting the number of chemicals used. However, it was found that the solution was unsuitable for printing, as the AAM separated from the water under pressure. It was then observed that mixing the ink with a weight per volume percent of AAM higher than 29 wt/v% resulted in agglomerates, as shown in Figure 5.1. An engineering approach was employed for the ink design, by separately addressing its three primary functions: (1) possessing the appropriate rheological properties to be printable and maintain its shape after deposition, (2) retaining its shape while in the cell-culture bath, and (3) facilitating the attachment and growth of cells. This design method offered several advantages, including the ability to change the biological content, if necessary, without requiring a redesign of the ink, and the potential to perform most of the tuning without the biological content, thereby significantly reducing development costs.

Figure 5.1. *Bioink containing 30w/v% AAM inside the cup after mixing for 1min in the planetary mixer. The agglomerates are present at the surface of the ink which are not present in properly mixed ink.*

To address the first function, pluronic, a biomedical polymer composed of triblock PEO-PPO-PEO copolymers of poly(ethylene oxide) (PEO) and poly(propylene oxide) (PPO), was used as the base ink to carry the AAM. Pluronic hydrogel inks are commonly used for DIW due to their ease of preparation and decreased viscosity at low temperature[78]. Additionally, their high-water content simplifies the printing process by reducing the risk of nozzle clogging and drying. Typically, 20 to 25 wt% of pluronic is used for DIW.

Sodium alginate is a chemical component extracted from brown algae that is soluble in water, and gelation occurs in the presence of divalent ions such as Ca2+ or trivalent ions[160]. Sodium alginate was integrated into the ink to satisfy the second function. The cross-linkage of alginate can be done using either $CaCl_2$ or a mixture of $CaCO_3$ with D-(+)-gluconic acid δ-lactone (GDL). The cross-linking of sodium alginate in $CaCl_2$ is instantaneous but varies from a few minutes to over an hour in the mixture of $CaCO_3$/GDL, depending on the proportions[161]. Whereas Emily *et al.*[161] have shown that slow gelation is often more advantageous as it is more controlled, in the case of sodium alginate mixed with a Pluronic ink, $CaCl_2$ is more suitable for printing. The prints leaked when placed in a solution of $CaCO_3$/GDL, ending up forming a gel-like bubble attached to

the structure, a phenomenon we attribute to the competition between cross-linking of sodium alginate and dissolution of the pluronic ink in the solution, as shown in Figure 5.2.

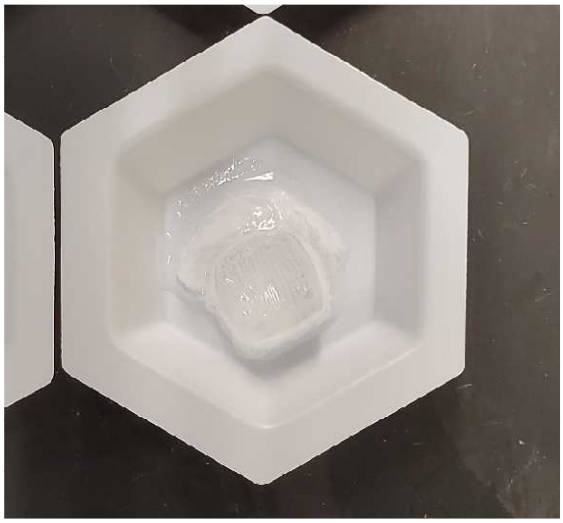

Figure 5.2. *Structure printed with Pluronic ink with alginate cross-linked with $CaCO_3$. The cross-linkage is competing with the desegregation of the structure resulting on the linking of its inside.*

Conventionally, bioprinting uses a maximum amount of 6 wt/v% of sodium alginate, according to previous research[161–164]. However, preliminary tests showed that a formulation consisting of 25 wt% pluronic with 6 wt/v% crosslinked sodium alginate did not maintain structural integrity in PBS solution at 37°C over an extended period. Therefore, the final formulations, which are shown in Table 5.1, were adjusted. The ink was composed of 15 wt% pluronic, which is the maximum amount before gelation [13]. This amount makes the mixing easier, and the remaining chemical can be used to finely tune the rheology. The content of sodium alginate was increased because it was observed that the stiffness of crosslinked alginate increases with an increase in sodium alginate. The study of the bioink 1 was limited as the access to ECM was extremely limited. Therefore, some aspects of the bioink 1 could not be studied.

	Pluronic (wt%)	Sodium Alginate (wt/v%)	AAM (wt/v%)	ECM (wt/v%)
Ink 10SA10ECM	15	10	0	10
Ink 20SA10AAM	15	20	10	0
Ink 10SA30AAM	15	10	30	0
Ink 10SA10AAM	15	10	10	0

Table 5.1. *Chemical composition of the four inks.*

5.3.2 Rheology

The rheology of the three bioinks composed of the AAM was evaluated to determine their suitability for Direct Ink Writing. The rheological behavior of the ink is critical to ensure its flow through the nozzle and retention of shape after deposition. Typically, a shear-thinning behavior with a yield stress is expected for DIW, which is often described using the Herschel-Bulkley (HB) model[44]:

$$\sigma = \sigma_y + K\dot{\gamma}^n \qquad \textbf{EQ. 27}$$

with σ the shear stress (Pa), $\dot{\gamma}$ the shear rate (s^{-1}), σ_y the yield stress (Pa), K the consistency index ($Pa.s^n$) and n the non-dimensional flow index. The HB model is typically used to describe the rheological behavior of the ink at medium and high shear rates, with $n < 1$ indicating a shear-thinning behavior, $n = 1$ indicating a Newtonian behavior, and $n > 1$ indicating a shear-thickening behavior. It is important that the yield stress of the ink be sufficiently high to maintain integrity of the structure after deposition. However, the HB model is not well-suited for low shear rates, where the shear stress falls below the yield stress of the ink. To address this issue, the Herschel-Bulkley-Papanastasiou (HBP) model was introduced to converge at low shear rates. The stress/strain rate response is defined as[165,166]:

$$\sigma = \sigma_y(1 - \exp(-m\dot{\gamma})) + K\dot{\gamma}^n \qquad \textbf{EQ. 28}$$

with *m* a constant coefficient. The HBP model converges to zero at low shear rates and fits the HB model with increasing shear rates. The extracted parameters for the three bioinks are presented in Table 5.2, indicating that all three possess a shear-thinning behavior with yield stress, making them ideal for DIW, as demonstrated in Figure 5.3a. Bioink 10SA30AAM, with its high AAM content, has the highest yield stress (560 Pa). Furthermore, the flow indexes (*n*) for each bioink are similarly low, facilitating their printing process.

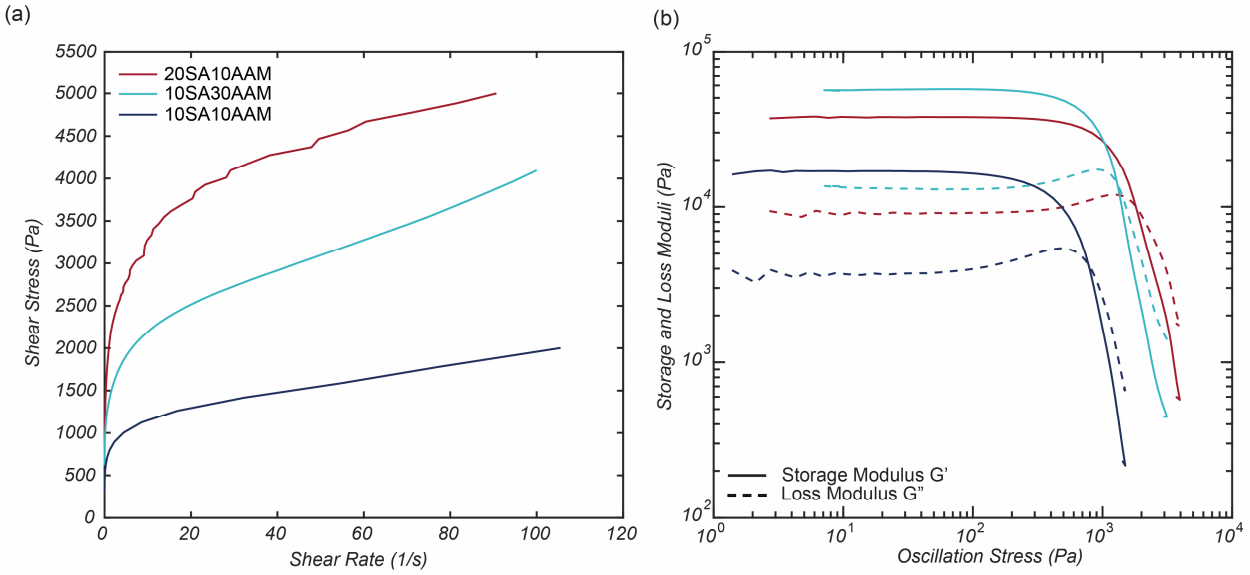

Figure 5.3. *(a) Relationship between shear stress and shear rate for the three bioinks. (b) Evolution of storage and loss moduli in function of the oscillation stress for the three bioink.*

	K (Pa.s^n)	n	Yield Stress (Pa)	Tabletop speed (mm/s)	Pressure (kPa)
Ink 20SA10AAM	1426	0.27	393.7	15	206.8
Ink 10SA30AAM	803.7	0.302	560	15	137.9
Ink 10SA10AAM	474.7	0.267	241.8	10	55.16

Table 5.2. *HBP parameters extracted from the fitting of the flow curves and the printing parameters for the three bioinks.*

The low shear rate behavior of the bioinks presents a challenge due to their complex behavior. For instance, the inks undergo creep in the Linear Viscoelastic Regime, as shown in Figure 5.4a

Furthermore, even after 60 minutes, the bioinks have not reached a stable state. At high stress, the creep is significant, consistent with the liquid-like state of the bioinks at those stresses (Figure 5.4b). Oscillation tests provide a deeper understanding of the ink's behavior (Figure 5.3b). At low stress, the storage modulus is higher than the loss modulus, indicating that the ink is in a solid-like state. As the stress increases, the moduli depart from the Linear Viscoelastic Regime (LVR) that is characterized by invariance of the moduli. Then, the trend reverses, and the loss modulus becomes larger than the storage modulus, defining a liquid-like state. The crossover region can provide a rough estimation of the yield stress. The storage modulus is similar across all three bioinks allowing the printing of similar features.

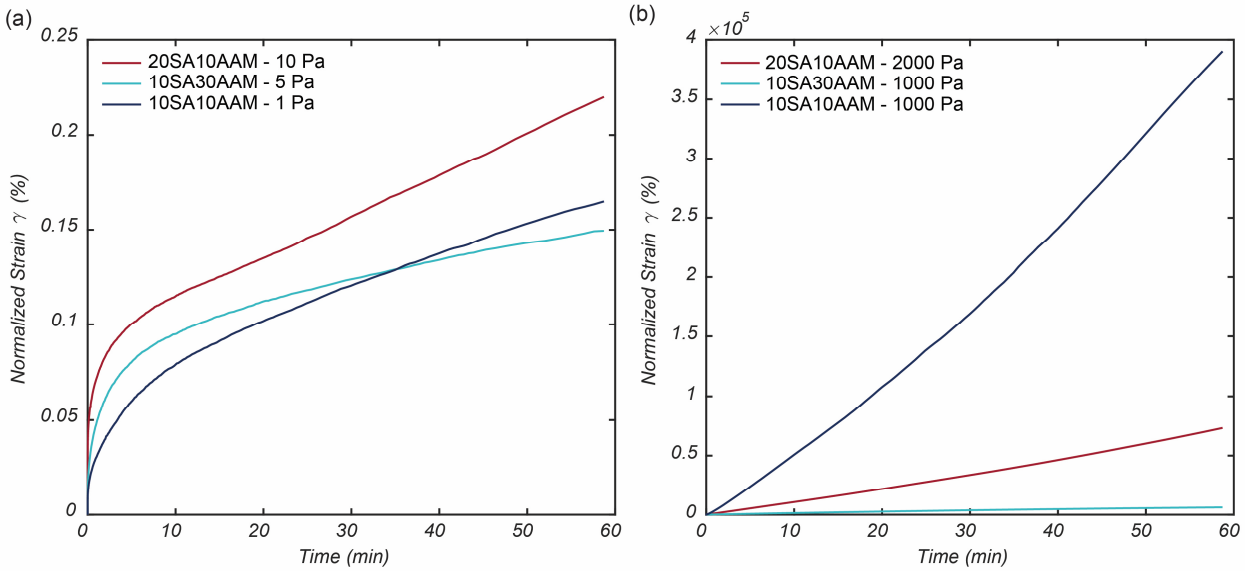

Figure 5.4. *Normalized strain over time for the three bioinks at (a) low stress and (b) at high stress.*

5.3.3 Printing

Printing structures for biological applications requires them to be strong enough to maintain their shape after deposition and during culture, while also facilitating easy cell migration. Optimizing printing parameters is essential for achieving high-quality prints. Sarker et *al.*[46] used

Herschel-Bulkley parameters to predict printing parameters by linking tabletop speed to applied pressure through the flow rate of the ink through a conical nozzle as shown in Figure 5.5. While this relationship was not fully validated in this study due to limited access to AAM, it served as a starting point for determining a set of printing parameters. The pressure was chosen to be high enough for fast printing but not so high as to cause changes in rheology within the nozzle and result in erratic printing. Although the selected parameters (Figure 5.5 black stars) were in good agreement with the model, some adjustments were necessary as each batch of bioink varied slightly (Table 5.2).

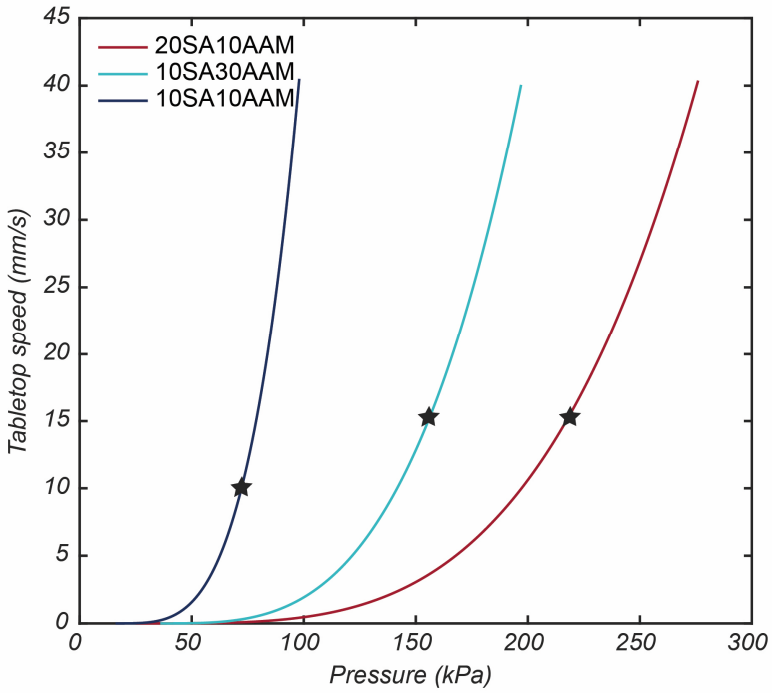

Figure 5.5. *Relationship of the tabletop speed with the pressure for the three bioinks. The black stars represent the set of parameters.*

Although the gcode for a woodpile structure can be easily programmed, the complex shape of an ear necessitates the use of a slicer software to generate the gcode. However, the stiffness of the ink permits the printing of the ear without the need for additional support. To prevent the ink from

being deposited during travel, the travel speed was set to be considerably higher than the printing speed. The printed woodpile structure and ear scaffold are depicted in Figure 5.6.

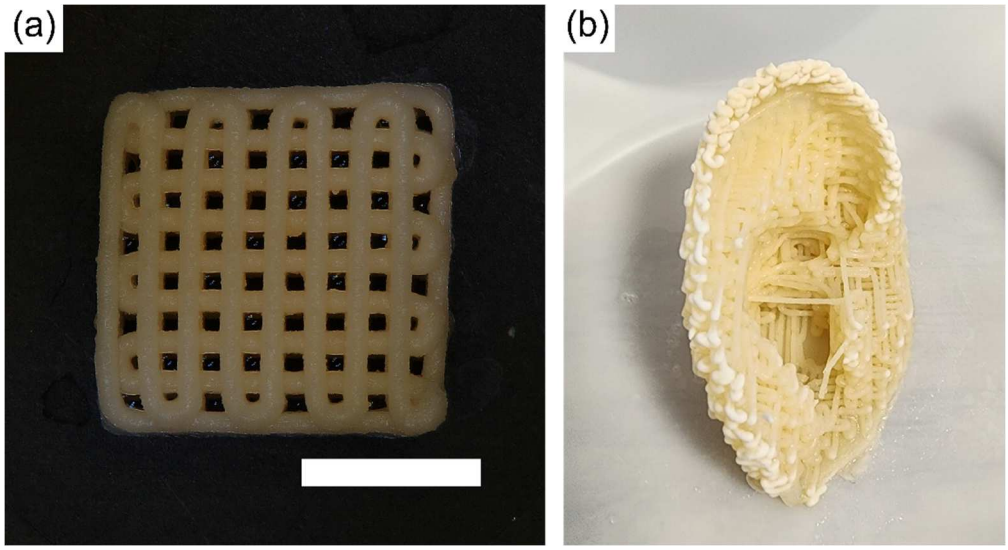

Figure 5.6. *(a) Top view of a woodpile structure of ink 20SA10AAM after crosslinking. Scale bar: 5 mm (b) Perspective view of the scaffold of an ear made of ink 20SA10AAM. The density of the infill is 50% with a woodpile structure of infill.*

5.3.4 Material Characterization

Figure 5.7 depicts the Fourier Transform Infrared (FTIR) spectra of the three ink formulations, both before and after alginate crosslinking. Figure 5.7a presents the spectra of the base materials (pluronic, sodium alginate and AAM): notice that the spectra for sodium alginate and AAM are very similar. The spectra of the three inks, regardless of whether the alginate is crosslinked or not, also appear to be similar. Post crosslinking, the peaks associated with pluronic disappeared, leaving only the peaks associated with sodium alginate and AAM. Pluronic appears to be removed during the crosslinking step, consistently with existing literature for systems with lower levels of alginate[167]. Removal of pluronic facilitates the creation of microscale porosity, thereby enhancing cell attachment to the structures.

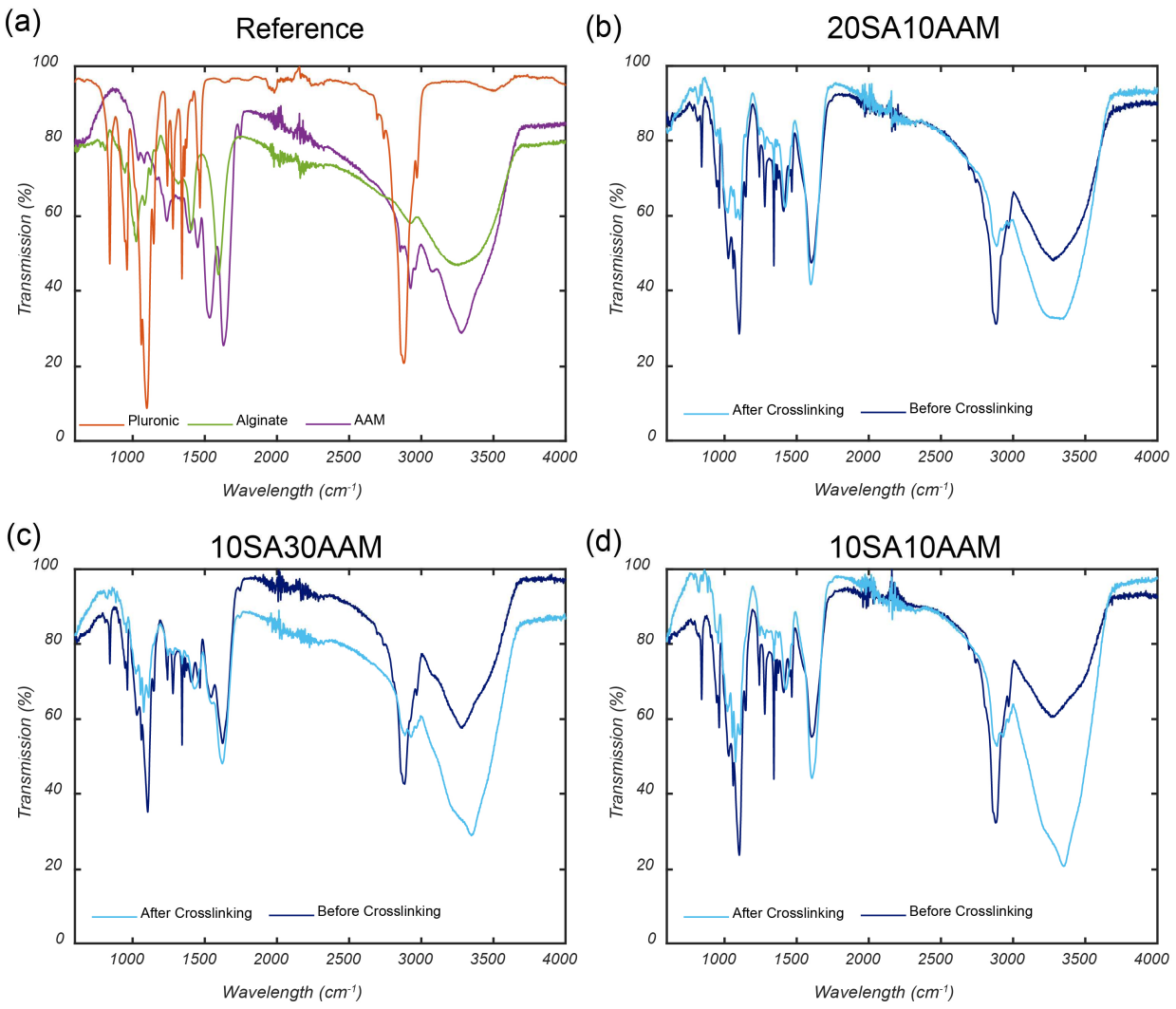

Figure 5.7. *FTIR for the different chemical composition before and after crosslinking. (a) the spectrum of AAM, Pluronic and alginate. (b), (c) and (d) are the spectrum of the ink 20SA10AAM, 10SA30AAM, and 10SA10AAM respectively.*

Figure 5.8 depicts the microstructure of the woodpile structures generated using four different ink formulations. Low vacuum microscopy was employed to prevent water evaporation during imaging. The microstructures across the various formulations are comparable, featuring a cellular microstructure, due to the removal of pluronic. Prior research has demonstrated that a 6 wt% pluronic-to-alginate ratio of 2:1 produces a cellular microstructure, unlike pure alginate[167]. The particles of the extracellular matrix (ECM) in Ink 10SA10ECM are evident within the lines, with

some particles exposed to enable access by cells, rather than being restricted to the crosslinked alginate. The same observation applies to the AAM particles, albeit with smaller particle sizes (the AAM particles absorb electrons more effectively than the alginate, rendering them very dark in appearance). Within the line, large pores are also visible, resulting from ink preparation as shown in previous chapters. The structures exhibit high-quality printing, with well-formed channels measuring around 400 μm, enabling cell travel throughout the structures.

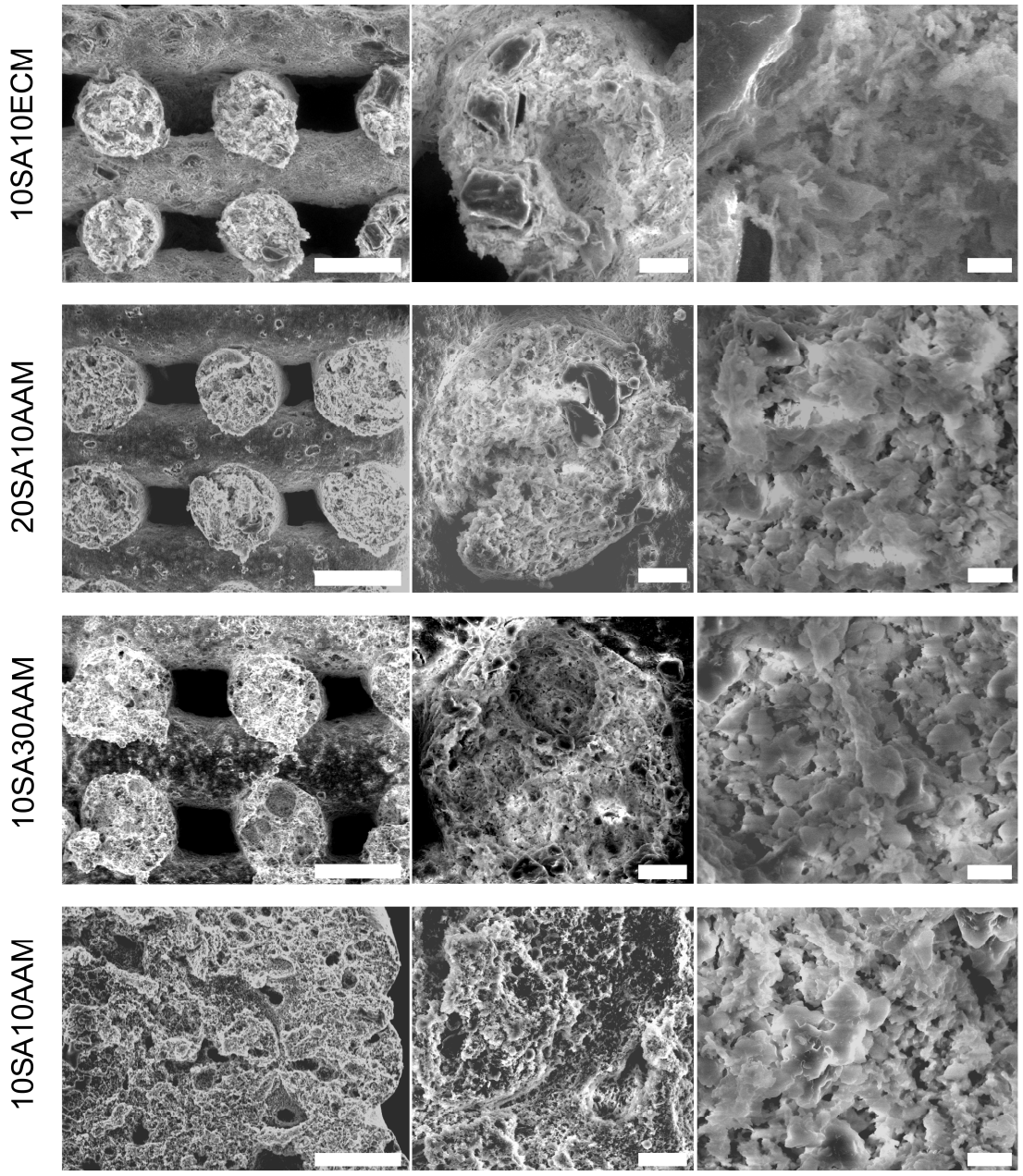

Figure 5.8. *Low-vacuum SEM microscopy of the woodpile structures printed with the four different formulations. Scale Bar: 0.5mm, 0.25mm and 0.1 mm for the first, second and third column, respectively.*

Figure 5.9 depicts the woodpile structures under scanning electron microscopy at high vacuum, where the structures are completely dry. Cracks are visible in all structures, and ink 10SA30AAM and 10SA10AAM exhibit significant shrinkage compared to ink 20SA10AAM, which is attributed

to the higher alginate content in ink 20SA10AAM. Significant delamination is observed in ink 10SA30AAM, while ink 20SA10AAM maintains better structural integrity. Cracks are also visible under low vacuum microscopy, caused by the first drying step before microscopy. The swelling of the lines when hydrated makes observation of the cracks difficult.

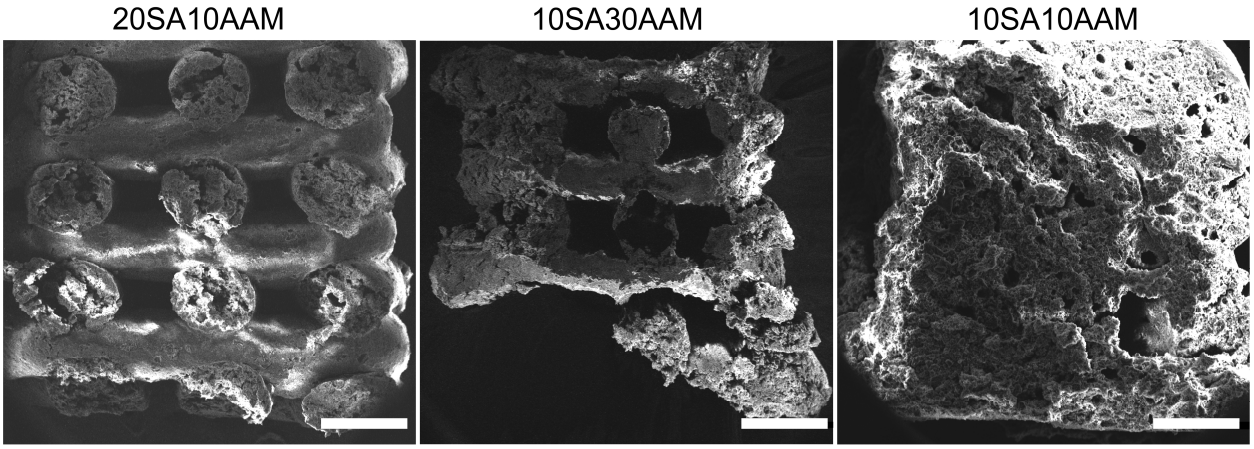

Figure 5.9. *High vacuum SEM microscopy of the woodpile structures printed with inks 20SA10AAM, 10SA30AAM, and 10SA10AAM. Scale bar: 0.5 mm.*

CT scanning of the woodpile structures for each chemical composition was performed both in dry and wet conditions. Significant porosities were observed for every chemical composition, which originated from the bubbles created during ink preparation. The scans demonstrate high-quality prints with the formation of channels for cell migration. The wet samples exhibited good wettability, as water was observed between the lines, which is an important property for ensuring the proper migration of cells through the structure. Consequently, lower porosity was observed in the wet samples, indicating that water penetrated the lines and filled part of the pores, thereby creating an interconnect network.

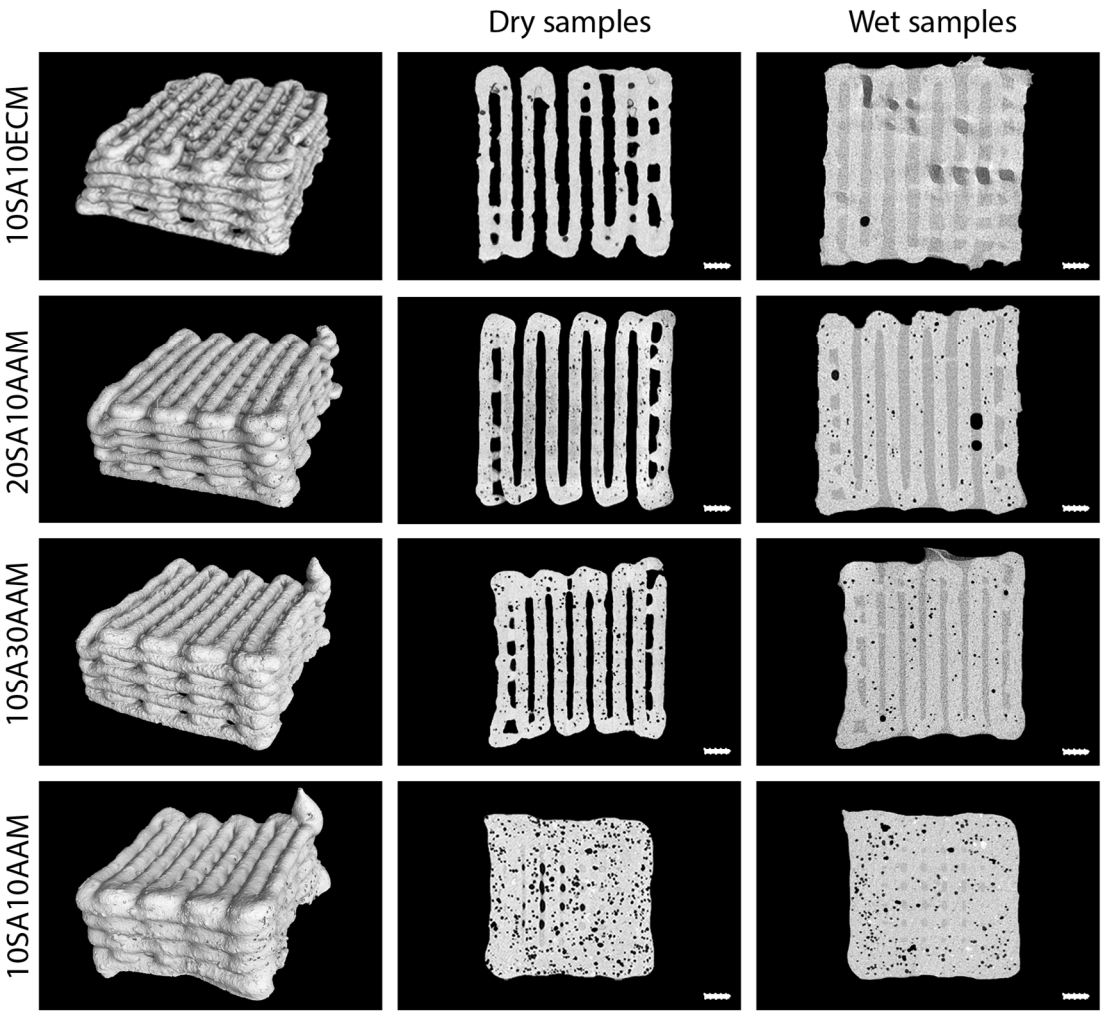

Figure 5.10. *CT scans of the woodpile structures printed with the four inks. For each ink, the images from left to right show a perspective view of the dry sample, a slice of the dry sample and a slice of the wet sample after 2 hours in the water, respectively. Scale bar: 1mm.*

5.3.5 Cell Adherence and Chondrogenesis Assessment

In preliminary studies (data not shown), we assessed the four inks and determined that ink 20SA10AAM provided the best structure for cell culture. To test the adherence of cells to ink 20SA10AAM, we cultured ADSCs on the scaffolds and revealed that collagen content and type I collagen expression were both increased when the scaffolds were seeded with cells (Figure 5.10a and 5.10b, respectively). Several structures printed with ink from each chemical composition with the exception of 20SA10AAM failed during the transfer for the histology. Therefore, the

20SA10AAM ink appears to strong enough to be manipulated while also improving the survivability of the cells and promoting the formation of type 1 collagen.

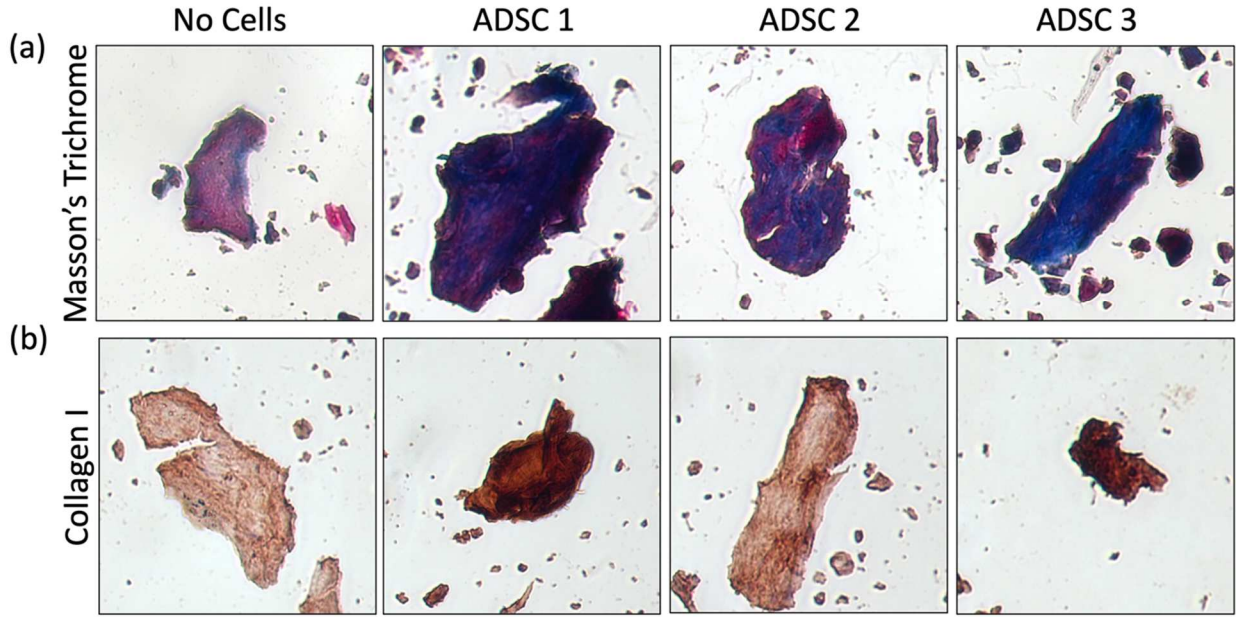

Figure 5.11. *Staining of ink 20SA10AAM scaffolds to assess cell adherence and survival after seeding with ADSCs and in vitro culture for two weeks. (a) Masson's Trichrome reveals higher stain intensity in scaffolds seeded with cells, indicating higher overall collagen content. (b) Immunohistochemistry also shows more intense staining in scaffolds seeded with cells, indicating higher type I collagen expression. ADSC 1-3 are 3 representative areas of the scaffolds seeded with cells.*

The drying step for UV sterilization creates cracks in the structures made of ink 10SA10ECM, 10SA30AAM, and 10SA10AAM that do not heal upon rehydration, leading to the disintegration of the structures and hindering cell attachment and survivability. Although cracks are also present in ink 20SA10AAM structures, their integrity remains intact, making this formulation suitable for cell growth. Despite this, all formulations display a multi-scale porosity network that is suitable for cell survivability and attachment. The formulation of ink 20SA10AAM strikes a good balance between the formation of cracks to facilitate cell migration and maintaining good structural integrity.

5.4 Conclusions

Current treatments for microtia are invasive, painful, and often performed at an early age, highlighting the need for alternative solutions. Additive manufacturing of ear scaffolds that allows mesenchymal stem cells (MSCs) to grow and develop into new cartilage presents a promising approach. To meet the requirements for general bioprinting applications and cartilage engineering, a bioink was developed and optimized for biocompatibility, low toxicity, limitation of the chemical used and the ability to maintain scaffold shape during co-culture. The bioink is designed to allow for an easy substitution of AAM with other biological materials, if required. The fine-tuned ink formulation enables the creation of highly intricate ear scaffolds with exceptional precision, without the need for support or indirect processing. The 3D printing of these bioinks has shown remarkable results, with the formation of multi-scale porosity that creates an optimal environment for cell attachment, migration, and growth. The use of alginate enables the fabrication of stiff scaffolds while providing direct access to the AAM particles for the cells. Bioink 20SA10AAM has been demonstrated to be the most suitable formulation, with the drying process for sterilization creating non-critical cracks that improves cell migration without compromising the scaffold's integrity. MSCs cultured on the scaffold have demonstrated their ability to survive and thrive, producing collagen, a crucial step in generating cartilage.

6. Conclusions

Adopting an architected materials framework and using Direct Ink Writing as the fabrication process, this thesis aimed to answer three fundamental research questions: (i) Can we design and fabricate ceramic architected materials that exploit topological design to control crack propagation and achieve higher strength than monolithic solids at a fraction of the weight? (ii) Can we develop a high-throughput approach for rapid characterization of the statistical distribution of the strength of ceramic materials, thus dramatically accelerating new material design? (iii) Can we demonstrate a framework for the fabrication of architected materials that serve as scaffolds for the growth of biological tissue, with a special application to the development of cartilage from stem cells? These questions were answered in chapters 3-5.

Chapter 3 detailed the development and optimization of an alumina ink to produce woodpile structures using Direct Ink Writing (DIW). Despite the complex rheological behavior of the ink, it was possible to optimize the printing parameters to achieve high-quality prints with feature sizes as small as 200 μm. Fabricating alumina woodpile structures allowed great control over the defect populations (the use of porous structures limited the presence of cracks and delaminations that routinely plague monolithic macroscopic components), as well as tailoring crack growth upon mechanical loading. As a result, we could produce alumina woodpile structures with compressive strength as high as that of bulk monolithic samples, at half the weight.

In chapter 4, a high-throughput characterization approach was developed for the extraction of the statistical distribution of strength from a large number of ceramic samples from multiple materials formulations (all derivatives of the base alumina system discussed in chapter 3). Over 1,500 samples were printed, and 300 samples were characterized. Printing of small-scale structures (lines that were tens of millimeters long and hundreds of microns thick) allowed easy sintering to

complete densification, approaching flexural strengths toward the upper limit of the values found in the literature. While the approach is based on DIW processing, this methodology can be used to characterize nearly any ceramic material, for application to virtually any processing technology. We systematically investigated the decline in mechanical properties that results upon scale-up, when multi-line multi-layer structures are built. The results suggested the design of sandwich-type structures for exceptional bending stiffness and strength. We demonstrated a sandwich structure made of alumina/10% zirconia with bending strength almost 50% higher than for a solid sample of the same material, while being 20% lighter. This study demonstrated that control of defects at multiple scales is essential for the manufacturing of strong and lightweight ceramic architected materials.

In chapter 5, our research focused on developing bioinks for 3D printing scaffolds that can be used for cartilage engineering. We designed the ink by breaking it down into separate functions that could be independently addressed. Woodpile structures were used as building blocks to create more complex scaffold geometries, such as ear-shaped constructs. During the fabrication process, pluronic, which was introduced into the ink for rheological purposes, was appropriately removed, and cracks would form during the drying process for UV sterilization of the sample before seeding. These phenomena, combined with the geometry and the presence of bubbles, created a multi-scale porous material that favored the attachment, survival, and growth of cells. Bioink 20SA10AAM was found to be the most effective due to its chemistry, which allowed for the formation of cracks that facilitated cell migration while maintaining structural integrity. Co-culture using bioink 20SA10AAM was successful, as collagen formation was observed.

Collectively, this thesis demonstrated that Direct Ink Writing, when combined with architected materials design principles, is an exceptionally promising additive manufacturing technology for

the fabrication of novel structural and functional materials with unprecedented combinations of properties, with applications of interest to a wide range of industries, ranging from aerospace to biomedical.

References

1. Kadic, M., Milton, G.W., van Hecke, M. et al. 3D metamaterials. Nat Rev Phys 1, 198–210 (2019).

2. Crook, C. *et al.* Plate-nanolattices at the theoretical limit of stiffness and strength. *Nat Commun* **11**, 1–11 (2020).

3. Hashin, Z. & Shtrikman, S. A variational approach to the theory of the elastic behaviour of multiphase materials. *J Mech Phys Solids* **11**, 127–140 (1963).

4. Suquet, P. M. Overall potentials and extremal surfaces of power law or ideally plastic composites. *J Mech Phys Solids* **41**, 981–1002 (1993).

5. Bauer, J., Schroer, A., Schwaiger, R. & Kraft, O. Approaching theoretical strength in glassy carbon nanolattices. *Nat Mater* **15**, 438–443 (2016).

6. Bauer, J. *et al.* Nanolattices: an emerging class of mechanical metamaterials. *Advanced Materials* **29**, 1701850 (2017).

7. Hall, E. O. The deformation and ageing of mild steel: III Discussion of results. *Proceedings of the Physical Society. Section B* **64**, 747–753 (1951).

8. Skylar-Scott, M. A., Gunasekaran, S. & Lewis, J. A. Laser-assisted direct ink writing of planar and 3D metal architectures. *Proceedings of the National Academy of Sciences* **113**, 6137–6142 (2016).

9. Shahzad, A. & Lazoglu, I. Direct ink writing (DIW) of structural and functional ceramics: Recent achievements and future challenges. *Composites Part B: Engineering* vol. 225 (2021).

10. Zhang, D. *et al.* A 3D-printing method of fabrication for metals, ceramics, and multi-materials using a universal self-curable technique for robocasting. *Mater Horiz* (2020).

11. Lewis, J. A. Direct-write assembly of ceramics from colloidal inks. *Curr Opin Solid State Mater Sci* **6**, 245–250 (2002).

12. CESARANO III, J. Robocasting of Ceramics and Composites Using Fine Particle Suspensions. *University of North Texas Libraries* (1999).

13. Feilden, E. & Ezra. Additive manufacturing of ceramics and ceramic composites via robocasting. (2017).

14. Revelo, C. F. & Colorado, H. A. 3D printing of kaolinite clay ceramics using the Direct Ink Writing (DIW) technique. *Ceram Int* **44**, 5673–5682 (2018).

15. Fu, Z. *et al.* Micro- and macroscopic design of alumina ceramics by robocasting. *J Eur Ceram Soc* **37**, 3115–3124 (2017).

16. Grosskopf, A. K. *et al.* Viscoplastic Matrix Materials for Embedded 3D Printing. *ACS Appl Mater Interfaces* **10**, 23353–23361 (2018).

17. Bertoldi, K., Reis, P. M., Willshaw, S. & Mullin, T. Negative Poisson's Ratio Behavior Induced by an Elastic Instability. *Advanced Materials* **22**, 361–366 (2010).

18. Evans, K. E. & Alderson, A. Auxetic Materials: Functional Materials and Structures from Lateral Thinking! *Advanced Materials* **12**, 617–628 (2000).

19. Lakes, R. Cellular solids with tunable positive or negative thermal expansion of unbounded magnitude. *Appl Phys Lett* **90**, (2007).

20. Wu, L., Li, B. & Zhou, J. Isotropic Negative Thermal Expansion Metamaterials. (2016).

21. Radman, A., Huang, X. & Xie, Y. M. Topology optimization of functionally graded cellular materials. *J Mater Sci* **48**, 1503–1510 (2013).

22. Guell Izard, A. & Valdevit, L. Magnetoelastic Metamaterials for Energy Dissipation and Wave Filtering. *Adv Eng Mater* **22**, 1901019 (2020).

23. Meaud, J. & Che, K. Tuning elastic wave propagation in multistable architected materials. *Int J Solids Struct* **122–123**, 69–80 (2017).

24. Schaedler, T. A. *et al.* Ultralight metallic microlattices. *Science (1979)* **334**, 962–965 (2011).

25. Meza, L. R., Das, S. & Greer, J. R. Strong, lightweight, and recoverable three-dimensional ceramic nanolattices. *Science (1979)* **345**, 1322–1326 (2014).

26. Fleck, N. A., Deshpande, V. S. & Ashby, M. F. Micro-architectured materials: past, present and future. *Proc. R. Soc. A* **466**, 2495–2516 (2010).

27. Deshpande, V. S., Ashby, M. F. & Fleck, N. A. Foam topology bending versus stretching dominated architectures. *Acta mater* vol. 49 (2001).

28. Valdevit, L. & Bauer, J. Fabrication of 3D Micro-Architected/Nano-Architected Materials. in *Three-Dimensional Microfabrication Using Two-Photon Polymerization: Fundamentals, Technology, and Applications* 345–373 (Elsevier Inc., 2016). doi:10.1016/B978-0-323-35321-2.00018-2.

29. Fleck, N. A. & Qiu, X. M. The damage tolerance of elastic-brittle, two-dimensional isotropic lattices. *J Mech Phys Solids* **55**, 562–588 (2007).

30. Griffith, A. A. The phenomena of rupture and flow in solids. (1995)

31. Guell Izard, A., Bauer, J., Crook, C., Turlo, V. & Valdevit, L. Ultrahigh Energy Absorption Multifunctional Spinodal Nanoarchitectures. *Small* **15**, 1903834 (2019).

32. Bauer, J. *et al.* Additive Manufacturing of Ductile, Ultrastrong Polymer-Derived Nanoceramics. *Matter* **1**, 1547–1556 (2019).

33. Cesarano, J. A review of robocasting technology. *Materials Research Society Symposium - Proceedings* **542**, 133–139 (1999).

34. M'Barki, A., Bocquet, L. & Stevenson, A. Linking Rheology and Printability for Dense and Strong Ceramics by Direct Ink Writing. *Sci Rep* **7**, 1–10 (2017).

35. Compton, B. G. & Lewis, J. A. 3D-printing of lightweight cellular composites. *Advanced Materials* **26**, 5930–5935 (2014).

36. Franchin, G., Wahl, L. & Colombo, P. Direct ink writing of ceramic matrix composite structures. *Journal of the American Ceramic Society* **100**, 4397–4401 (2017).

37. Duoss, E. B. *et al.* Direct-Write Assembly of Functional Inks for Planar and 3D Microstructures. *Assembly* 66–70 (2011).

38. Lewis, J. A. Colloidal Processing of Ceramics. *J. Am. Ceram. Soc.*, 83 [10] 2341–59 (2000)

39. Guo, S.-Z., Heuzey, M.-C. & Therriault, D. Properties of Polylactide Inks for Solvent-Cast Printing of Three-Dimensional Freeform Microstructures. *Langmuir* **30**, 1142–1150 (2014).

40. Zhu, C. *et al.* Colloidal Materials for 3D Printing. *Annu Rev Chem Biomol Eng* **10**, 17–42 (2019).

41. Pattanaik, M. & Bhaumik, S. K. Adsorption behaviour of polyvinyl pyrrolidone on oxide surfaces. *Mater Lett* **44**, 352–360 (2000).

42. G. K. Batchelor. The effect of Brownian motion on the bulk stress in a suspension of spherical particles. *J Fluid Mech* **83**, 97–117 (1977).

43. Krieger, I. M. & Dougherty, T. J. A Mechanism for Non-Newtonian Flow in Suspensions of Rigid Spheres. *Transactions of the Society of Rheology* **3**, 137–152 (1959).

44. Herschel, W. H. & Bulkley, R. Ronsistenzmessungen yon (ummi-BenzollGsungen). *Colloid and Polymer Science* **39,** 291 (1926).

45. Morissette, S. L., Lewis, J. A., Cesarano, J., Dimos, D. B. & Baer, T. Solid Freeform Fabrication of Aqueous Alumina-Poly(vinyl alcohol) Gelcasting Suspensions. *Journal of the American Ceramic Society* **83**, 2409–2416 (2004).

46. Sarker, Md. & Chen, X. B. Modeling the Flow Behavior and Flow Rate of Medium Viscosity Alginate for Scaffold Fabrication With a Three-Dimensional Bioplotter. *J Manuf Sci Eng* **139**, (2017).

47. Yuk, H. & Zhao, X. A New 3D Printing Strategy by Harnessing Deformation, Instability, and Fracture of Viscoelastic Inks. *Advanced Materials* **30**, 1704028 (2018).

48. Smay, J. E. *et al.* Colloidal inks for directed assembly of 3-D periodic structures. *Langmuir* **18**, 5429–5437 (2002).

49. Tathe, A., Ghodke, M. & Nikalje, A. P. A brief review: Biomaterials and their apllication. *Int J Pharm Pharm Sci* **2**, 19–23 (2010).

50. Caló, E. & Khutoryanskiy, V. V. Biomedical applications of hydrogels: A review of patents and commercial products. *Eur Polym J* **65**, 252–267 (2015).

51. Correa, S. *et al.* Translational Applications of Hydrogels. *Chem Rev* **121**, 11385–11457 (2021).

52. Ishikawa, K., Matsuya, S., Miyamoto, Y. & Kawate, K. Bioceramics. *Comprehensive Structural Integrity: Nine Volume Set* **1–9**, 169–214 (2003).

53. Piconi, C., Maccauro, G., Muratori, F. & Brach Del Prever, E. Alumina and zirconia ceramics in joint replacements. *J Appl Biomater Biomech* **1**, 19–32 (2003).

54. Tsoi, J. K. H., Lam, W. Y. H., Yu, H., Qu, Y. & Liu, L. Zirconia Materials for Dental Implants: A Literature Review. *Frontiers in Dental Medicine* **1**, 687983 (2021).

55. Salinas, A. J. & Vallet-Regí, M. Bioactive ceramics: from bone grafts to tissue engineering. *RSC Adv* **3**, 11116–11131 (2013).

56. Ohtsuki, C., Kamitakahara, M. & Miyazaki, T. Bioactive ceramic-based materials with designed reactivity for bone tissue regeneration. *J R Soc Interface* **6**, S349 (2009).

57. Wei, S., Ma, J. X., Xu, L., Gu, X. S. & Ma, X. L. Biodegradable materials for bone defect repair. *Military Medical Research 2020 7:1* **7**, 1–25 (2020).

58. Jung, Y. seok, Park, W., Park, H., Lee, D. K. & Na, K. Thermo-sensitive injectable hydrogel based on the physical mixing of hyaluronic acid and Pluronic F-127 for sustained NSAID delivery. *Carbohydr Polym* **156**, 403–408 (2017).

59. Wan, L. Q. *et al.* Calcium Concentration Effects on the Mechanical and Biochemical Properties of Chondrocyte-Alginate Constructs. *Cell Mol Bioeng* **1**, 93–102 (2008).

60. Drury, J. L., Dennis, R. G. & Mooney, D. J. The tensile properties of alginate hydrogels. *Biomaterials* **25**, 3187–3199 (2004).

61. Feilden, E., Glymond, D., Saiz, E. & Vandeperre, L. High temperature strength of an ultra-high temperature ceramic produced by additive manufacturing. *Ceram Int* **45**, 18210–18214 (2019).

62. Golla, B. R., Mukhopadhyay, A., Basu, B. & Thimmappa, S. K. Review on ultra-high temperature boride ceramics. *Progress in Materials Science* vol. 111 100651(2020).

63. Wiederhorn, S. M. Brittle fracture and toughening mechanisms in ceramics. *Ann. Rev. Mater. Sci* vol. 14 (1984).

64. Meza, L. R., Das, S. & Greer, J. R. Strong, lightweight, and recoverable three-dimensional ceramic nanolattices. *Science (1979)* **345**, 1322–1326 (2014).

65. Wendy Gu, X. & Greer, J. R. Ultra-strong architected Cu meso-lattices. *Extreme Mech Lett* **2**, 7–14 (2015).

66. Mieszala, M. *et al.* Micromechanics of Amorphous Metal/Polymer Hybrid Structures with 3D Cellular Architectures: Size Effects, Buckling Behavior, and Energy Absorption Capability. *Small* **13**, 1602514 (2017).

67. Bauer, J., Schroer, A., Schwaiger, R. & Kraft, O. The Impact of Size and Loading Direction on the Strength of Architected Lattice Materials. *Adv Eng Mater* **18**, 1537–1543 (2016).

68. Zhang, X., Vyatskikh, A., Gao, H., Greer, J. R. & Li, X. Lightweight, flaw-tolerant, and ultrastrong nanoarchitected carbon. *Proc Natl Acad Sci U S A* **116**, 6665–6672 (2019).

69. Bauer, J., Hengsbach, S., Tesari, I., Schwaiger, R. & Kraft, O. High-strength cellular ceramic composites with 3D microarchitecture. *Proc Natl Acad Sci U S A* **111**, 2453–2458 (2014).

70. Wu, Q., Maire, M., Lerouge, S., Therriault, D. & Heuzey, M.-C. 3D Printing of Microstructured and Stretchable Chitosan Hydrogel for Guided Cell Growth. *Adv Biosyst* **1**, 1700058 (2017).

71. Feilden, E. *et al.* 3D Printing Bioinspired Ceramic Composites. *Sci Rep* **7**, 13759 (2017).

72. Guo, S. Z. *et al.* Solvent-cast three-dimensional printing of multifunctional microsystems. *Small* **9**, 4118–4122 (2013).

73. Deshpande, V. S., Fleck, N. A. & Ashby, M. F. Effective properties of the octet-truss lattice material. *J Mech Phys Solids* **49**, 1747–1769 (2001).

74. Rueschhoff, L., Costakis, W., Michie, M., Youngblood, J. & Trice, R. Additive Manufacturing of Dense Ceramic Parts via Direct Ink Writing of Aqueous Alumina Suspensions. *Int J Appl Ceram Technol* **13**, 821–830 (2016).

75. Acosta, M., Wiesner, V. L., Martinez, C. J., Trice, R. W. & Youngblood, J. P. Effect of Polyvinylpyrrolidone Additions on the Rheology of Aqueous, Highly Loaded Alumina Suspensions. *Journal of the American Ceramic Society* **96**, 1372–1382 (2013).

76. Wiesner, V. L., Youngblood, J. P. & Trice, R. W. Room-temperature injection molding of aqueous alumina-polyvinylpyrrolidone suspensions. *J Eur Ceram Soc* **34**, 453–463 (2014).

77. Compel, W. S. & Lewicki, J. P. Advanced Methods for Direct Ink Write Additive Manufacturing. (2018).

78. Feilden, E., Blanca, E. G.-T. T., Giuliani, F., Saiz, E. & Vandeperre, L. Robocasting of structural ceramic parts with hydrogel inks. *J Eur Ceram Soc* **36**, 2525–2533 (2016).

79. Baltazar, J. *et al.* Influence of filament patterning in structural properties of dense alumina ceramics printed by robocasting. *J Manuf Process* **68**, 569–582 (2021).

80. Asmani, M., Kermel, C., Leriche, A. & Ourak, M. Influence of porosity on Youngs modulus and poisson's ratio in alumina ceramics. *J Eur Ceram Soc* **21**, 1081–1086 (2001).

81. Auerkari, P. Mechanical and physical properties of engineering alumina ceramics. *VTT Tiedotteita - Valtion Teknillinen Tutkimuskeskus* (1996).

82. Krell, A. & Blank, P. Grain Size Dependence of Hardness in Dense Submicrometer Alumina. *Journal of the American Ceramic Society* **78**, 1118–1120 (1995).

83. Tabor, D. The Hardness of Metals. (Oxford University Press, 2000).

84. Lankford, J. *et al.* The role of plasticity as a limiting factor in the compressive failure of high strength ceramics. *Mechanics of Materials* **29**, 205–218 (1998).

85. Subhash, G., Maiti, S., Geubelle, P. H. & Ghosh, D. Recent Advances in Dynamic Indentation Fracture, Impact Damage and Fragmentation of Ceramics. *Journal of the American Ceramic Society* **91**, 2777–2791 (2008).

86. Gibson, L. J. & Ashby, M. F. Cellular Solids. (Cambridge University Press, 1997).

87. Genet, M., Houmard, M., Eslava, S., Saiz, E. & Tomsia, A. P. A two-scale Weibull approach to the failure of porous ceramic structures made by robocasting: Possibilities and limits. *J Eur Ceram Soc* **33**, 679–688 (2013).

88. Timoshenko, S. P. & Gere, J. M. Theory of Elastic Stability. (1961).

89. Schulson, E. M. Brittle Fracture and Toughening. *Physical Metallurgy and processing of Intermetallic Compounds* 56–94 (1996).

90. Faber, K. T. & Evans, A. G. Crack deflection processes-I. Theory. *Acta Metallurgica* **31**, 565–576 (1983).

91. Davis, J. B., Kristoffersson, A., Carlström, E. & Clegg, W. J. Fabrication and crack deflection in ceramic laminates with porous interlayers. *Journal of the American Ceramic Society* **83**, 2369–2374 (2000).

92. Clegg, W. J. Controlling cracks in ceramics. *Science (1979)* **286**, 1097–1099 (1999).

93. Budiansky, B., Hutchinson, J. W. & Evans, A. G. Matrix fracture in fiber-reinforced ceramics. *J Mech Phys Solids* **34**, 167–189 (1986).

94. Marshall, D. B. & Evans, A. G. Failure Mechanisms in Ceramic-Fiber/Ceramic-Matrix Composites. *Journal of the American Ceramic Society* **68**, 225–231 (1985).

95. Curtin, W. A. Theory of Mechanical Properties of Ceramic-Matrix Composites. *Journal of the American Ceramic Society* **74**, 2837–2845 (1991).

96. Delage, J., Saiz, E. & Al Nasiri, N. Fracture behaviour of SiC/SiC ceramic matrix composite at room temperature. *J Eur Ceram Soc* **42**, 3156–3167 (2022).

97. Li, L. Damage, fracture, and fatigue of ceramic-matrix composites. *Springer Singapore* (2018).

98. Evans, A. G. & Cannon, R. M. Toughening of brittle solids by martensitic transformations. *Acta Metall.; (United States)* **34:5**, 761–800 (1986).

99. Hannink, R. H. J., Kelly, P. M. & Muddle, B. C. Transformation Toughening in Zirconia-Containing Ceramics. *Journal of the American Ceramic Society* **83**, 461–487 (2000).

100. Steinbrech, R. W. Toughening mechanisms for ceramic materials. *J Eur Ceram Soc* **10**, 131–142 (1992).

101. Kolken, H. M. A. *et al.* Mechanisms of fatigue crack initiation and propagation in auxetic meta-biomaterials. *Acta Biomater* **138**, 398–409 (2022).

102. Suksangpanya, N., Yaraghi, N. A., Pipes, R. B., Kisailus, D. & Zavattieri, P. Crack twisting and toughening strategies in Bouligand architectures. *Int J Solids Struct* **150**, 83–106 (2018).

103. Maurizi, M., Edwards, B. W., Gao, C., Greer, J. R. & Berto, F. Fracture resistance of 3D nano-architected lattice materials. *Extreme Mech Lett* **56**, (2022).

104. Conway, K. M., Kunka, C., White, B. C., Pataky, G. J. & Boyce, B. L. Increasing fracture toughness via architected porosity. *Mater Des* **205**, (2021).

105. Thiraux, R. *et al.* Damage tolerance in additively manufactured ceramic architected materials. *J Eur Ceram Soc* **42**, 5893–5903 (2022).

106. Xia, X. & Duan, G. Effect of solid loading on properties of zirconia ceramic by direct ink writing. *Mater Res Express* **8**, 15403 (2021).

107. Sun, Q. *et al.* Creation of three-dimensional structures by direct ink writing with kaolin suspensions. *J Mater Chem C Mater* **6**, 11392–11400 (2018).

108. Bonev, B. & Shopov, A. Computation of Second Area Moments of Cross-section Using Optical Images. in *10th National Conference with International Participation, ELECTRONICA 2019 - Proceedings* (Institute of Electrical and Electronics Engineers Inc., 2019).

109. Weibull, W., Distribution, A. S. & Applicability, W. Waloddi Weibull To cite this version: HAL Id : hal-03112318 A Statistical Distribution Function of Wide Applicability. 0–5 (1951).

110. Tang, S. *et al.* Layered extrusion forming—a simple and green method for additive manufacturing ceramic core. *International Journal of Advanced Manufacturing Technology* **96**, 3809–3819 (2018).

111. Schwentenwein, M. & Homa, J. Additive Manufacturing of Dense Alumina Ceramics. *Int J Appl Ceram Technol* **12**, 1–7 (2015).

112. Li, H. *et al.* The influence of sintering procedure and porosity on the properties of 3D printed alumina ceramic cores. *Ceram Int* **47**, 27668–27676 (2021).

113. Ndinisa, S. S., Whitefield, D. J. & Sigalas, I. Fabrication of complex shaped alumina parts by gelcasting on 3D printed moulds. *Ceram Int* **46**, 3177–3182 (2020).

114. Xing, Z., Liu, W., Chen, Y. & Li, W. Effect of plasticizer on the fabrication and properties of alumina ceramic by stereolithography-based additive manufacturing. *Ceram Int* **44**, 19939–19944 (2018).

115. Ćurković, L. *et al.* 76 Publications 430 Citations Flexural Strength of Alumina Ceramics: Weibull Analysis. 0–8 (2010).

116. Juang, H.-Y. & Hon, M.-H. Effect of Solid Content on Processing Stability for Injection Molding of Alumina Evaluated by Weibull Statistics. *Journal of the Ceramic Society of Japan* **103,** 430–433 (1995).

117. Fu, Y., Tao, Z. & Hou, X. Weibull distribution of the fracture strength of 99% alumina ceramic reshaped by cold isostatic pressing. *Ceram Int* **40**, 7661–7667 (2014).

118. Li, M. *et al.* Influence of yttria-stabilized zirconia content on rheological behavior and mechanical properties of zirconia-toughened alumina fabricated by paste-based stereolithography. *J Mater Sci* **56**, 2887–2899 (2021).

119. Chuankrerkkul, N., Somton, K., Wonglom, T., Dateraksa, K. & Laoratanakul, P. Physical and mechanical properties of Zirconia toughened alumina (ZTA) composites fabricated by powder injection moulding. *Chiang Mai Journal of Science* **43**, 375–380 (2016).

120. Wu, H. *et al.* Fabrication of dense zirconia-toughened alumina ceramics through a stereolithography-based additive manufacturing. *Ceram Int* **43**, 968–972 (2017).

121. Abbas, S., Maleksaeedi, S., Kolos, E. & Ruys, A. J. Processing and Properties of Zirconia-Toughened Alumina Prepared by Gelcasting. *Materials 2015, Vol. 8, Pages 4344-4362* **8**, 4344–4362 (2015).

122. Peng, E. *et al.* Robocasting of dense yttria-stabilized zirconia structures. *J Mater Sci* **53**, 247–273 (2018).

123. Tuan, W. H., Chen, R. Z., Wang, T. C., Cheng, C. H. & Kuo, P. S. Mechanical properties of Al2O3/ZrO2 composites. *J Eur Ceram Soc* **22**, 2827–2833 (2002).

124. An, J., Zhao, J., Su, Z. G., Wen, Z. & Xu, D. S. Microstructure and Mechanical Properties of ZTA Ceramic-Lined Composite Pipe Prepared by Centrifugal-SHS. *Arab J Sci Eng* **40**, 2701–2709 (2015).

125. Zhu, T., Xie, Z., Han, Y. & Li, S. Microstructure and mechanical properties of ZTA composites fabricated by oscillatory pressure sintering. *Ceram Int* **44**, 505–510 (2018).

126. Gafur, Md. A. *et al.* Structural and Mechanical Properties of Alumina-Zirconia (ZTA) Composites with Unstabilized Zirconia Modulation. *Materials Sciences and Applications* **12**, 542–560 (2021).

127. Du, W. *et al.* Formation and control of “intragranular” ZrO2 strengthened and toughened Al2O3 ceramics. *Ceram Int* **46**, 8452–8461 (2020).

128. Sarkar, D., Adak, S., Chu, M. C., Cho, S. J. & Mitra, N. K. Influence of ZrO2 on the thermo-mechanical response of nano-ZTA. *Ceram Int* **33**, 255–261 (2007).

129. Yoshizawa, Y. & Sakuma, T. Improvement of tensile ductility in high-purity alumina due to magnesia addition. *Acta Metallurgica Et Materialia* **40**, 2943–2950 (1992).

130. Harun, Z., Ismail, N. F. & Badarulzaman, N. A. Effect of MgO Additive on Microstructure of Al2O3. *Adv Mat Res* **488–489**, 335–339 (2012).

131. Chakravarty, D., Bysakh, S., Muraleedharan, K., Rao, T. N. & Sundaresan, R. Spark Plasma Sintering of Magnesia-Doped Alumina with High Hardness and Fracture Toughness. *Journal of the American Ceramic Society* **91**, 203–208 (2008).

132. Horn, D. S. & Messing, G. L. Anisotropic grain growth in TiO2-doped alumina. *Materials Science and Engineering A* **195**, 169–178 (1995).

133. Sathiyakumar, M. & Gnanam, F. D. Influence of MnO and TiO2 additives on density, microstructure and mechanical properties of Al2O3. *Ceram Int* **28**, 195–200 (2002).

134. Veljović, D. *et al.* The effect of the shape and size of the pores on the mechanical properties of porous HAP-based bioceramics. *Ceram Int* **37**, 471–479 (2011).

135. Du, T. *et al.* Nanomechanical investigation of the interplay between pore morphology and crack orientation of amorphous silica. *Eng Fract Mech* **250**, 107749 (2021).

136. Rezanezhad, M., Lajevardi, S. A. & Karimpouli, S. Application of equivalent circle and ellipse for pore shape modeling in crack growth problem: A numerical investigation in microscale. *Eng Fract Mech* **253**, 107882 (2021).

137. Heuer, A. H. Transformation Toughening in ZrO2-Containing Ceramics. *Journal of the American Ceramic Society* **70**, 689–698 (1987).

138. De Aza, A. H., Chevalier, J., Fantozzi, G., Schehl, M. & Torrecillas, R. Slow-crack-growth behavior of zirconia-toughened alumina ceramicsprocessed by different methods. *Journal of the American Ceramic Society* **86**, 115–120 (2003).

139. De Aza, A. H., Chevalier, J., Fantozzi, G., Schehl, M. & Torrecillas, R. Crack growth resistance of alumina, zirconia and zirconia toughened alumina ceramics for joint prostheses. *Biomaterials* **23**, 937–945 (2002).

140. van Nunen, D. P. F., Kolodzynski, M. N., van den Boogaard, M. J. H., Kon, M. & Breugem, C. C. Microtia in the netherlands: Clinical characteristics and associated anomalies. *Int J Pediatr Otorhinolaryngol* **78**, 954–959 (2014).

141. Firmin, F. & Marchac, A. A Novel Algorithm for Autologous Ear Reconstruction.

142. Andrews, J. & Hohman, M. H. Ear Microtia. *StatPearls* (2023).

143. Jessop, Z. M. *et al.* Combining regenerative medicine strategies to provide durable reconstructive options: auricular cartilage tissue engineering. *Stem Cell Research & Therapy 2016 7:1* **7**, 1–12 (2016).

144. Schroeder, M. J. & Lloyd, M. S. Tissue Engineering Strategies for Auricular Reconstruction. *J Craniofac Surg* **28**, 2007–2011 (2017).

145. Cohen, B. P., Bernstein, J. L., Morrison, K. A., Spector, J. A. & Bonassar, L. J. Tissue engineering the human auricle by auricular chondrocyte-mesenchymal stem cell co-implantation. *PLoS One* **13**, (2018).

146. Nazempour, A. & van Wie, B. J. Chondrocytes, Mesenchymal Stem Cells, and Their Combination in Articular Cartilage Regenerative Medicine. *Annals of Biomedical Engineering* vol. 44 1325–1354 (2016).

147. Banyard, D. A. *et al.* Preparation, characterization, and clinical implications of human decellularized adipose tissue extracellular matrix (hDAM): A comprehensive review. *Aesthet Surg J* **36**, 349–357 (2016).

148. Ziegler, M. E., Sorensen, A. M., Banyard, D. A., Evans, G. R. D. & Widgerow, A. D. Improving In Vitro Cartilage Generation by Co-Culturing Adipose-Derived Stem Cells and Chondrocytes on an Allograft Adipose Matrix Framework. *Plast Reconstr Surg* **147**, 87–99 (2021).

149. Xu, T., Jin, J., Gregory, C., Hickman, J. J. & Boland, T. Inkjet printing of viable mammalian cells. *Biomaterials* **26**, 93–99 (2005).

150. Xu, T. *et al.* Complex heterogeneous tissue constructs containing multiple cell types prepared by inkjet printing technology. *Biomaterials* **34**, 130–139 (2013).

151. Boland, T., Xu, T., Damon, B. & Cui, X. Application of inkjet printing to tissue engineering. *Biotechnology Journal* vol. 1 910–917 (2006).

152. Ware, H. O. T. *et al.* High-speed on-demand 3D printed bioresorbable vascular scaffolds. *Mater Today Chem* **7**, 25–34 (2018).

153. Guillotin, B. *et al.* Laser assisted bioprinting of engineered tissue with high cell density and microscale organization. *Biomaterials* **31**, 7250–7256 (2010).

154. Elomaa, L. *et al.* Preparation of poly(ε-caprolactone)-based tissue engineering scaffolds by stereolithography. *Acta Biomater* **7**, 3850–3856 (2011).

155. Iwami, K. *et al.* Bio rapid prototyping by extruding/aspirating/refilling thermoreversible hydrogel. *Biofabrication* **2**, (2010).

156. Guo, T. *et al.* Three dimensional extrusion printing induces polymer molecule alignment and cell organization within engineered cartilage. *J Biomed Mater Res A* **106**, 2190–2199 (2018).

157. Mäkitie, A. A. *et al.* Novel additive manufactured scaffolds for tissue engineered trachea research. *Acta Otolaryngol* **133**, 412–417 (2013).

158. Touri, M., Moztarzadeh, F., Osman, N. A. A., Dehghan, M. M. & Mozafari, M. 3D–printed biphasic calcium phosphate scaffolds coated with an oxygen generating system for enhancing engineered tissue survival. *Materials Science and Engineering C* **84**, 236–242 (2018).

159. Banyard, D. A., Salibian, A. A., Widgerow, A. D. & Evans, G. R. D. Implications for human adipose-derived stem cells in plastic surgery. *J Cell Mol Med* **19**, 21–30 (2015).

160. Rezende, R. A., Bártolo, P. J., Mendes, A. & Filho, R. M. Rheological behavior of alginate solutions for biomanufacturing. *J Appl Polym Sci* **113**, 3866–3871 (2009).

161. Growney Kalaf, E. A., Flores, R., Bledsoe, J. G. & Sell, S. A. Characterization of slow-gelling alginate hydrogels for intervertebral disc tissue-engineering applications. *Materials Science and Engineering C* **63**, 198–210 (2016).

162. Gori, M. *et al.* Biofabrication of Hepatic Constructs by 3D Bioprinting of a Cell-Laden Thermogel: An Effective Tool to Assess Drug-Induced Hepatotoxic Response. *Adv Healthc Mater* **9**, (2020).

163. Ooi, H. W. *et al.* Thiol-Ene Alginate Hydrogels as Versatile Bioinks for Bioprinting. *Biomacromolecules* **19**, 3390–3400 (2018).

164. Abrami, M. *et al.* Physical characterization of alginate-Pluronic F127 gel for endoluminal NABDs delivery. (2014).

165. Han, Z. *et al.* Numerical simulation of debris-flow behavior based on the SPH method incorporating the Herschel-Bulkley-Papanastasiou rheology model. *Eng Geol* **255**, 26–36 (2019).

166. Papanastasiou, T. C. Flows of Materials with Yield. *Journal of Rheology* **31**, 385 (1987).

167. Armstrong, J. P. K., Burke, M., Carter, B. M., Davis, S. A. & Perriman, A. W. 3D Bioprinting Using a Templated Porous Bioink. Advanced Healthcare Materials 5, 1724–1730 (2016).

Supplementary Materials 1

Damage Tolerance in additively manufactured ceramic architected materials

Figure S1.1. *Failed woodpile printed at 69 kPa with 410 µm nozzle diameter. Scale bar: 5 mm.*

Nozzle Size (mm)	*Theoretical Gap (mm)*	*Side 1 (mm)*	*Side 2 (mm)*	*Height (mm)*	*Volume (mm3)*	*Weight (g)*	*Density (g/cm3)*	*Relative Density*	*Average Relative Density*
0.41	0.41	8.48	8.43	7.79	556.88	1.485	2.67	0.69	0.70
		8.40	8.48	7.80	555.61	1.521	2.74	0.71	
		8.59	8.53	7.90	578.79	1.641	2.84	0.73	
		8.53	8.59	7.92	580.65	1.51	2.60	0.67	
	0.82	8.43	8.29	7.81	545.80	1.141	2.09	0.54	0.55
		8.52	8.52	7.68	557.49	1.128	2.02	0.52	
		8.48	8.59	7.71	561.62	1.115	1.99	0.51	
		8.48	8.46	7.80	559.54	1.221	2.18	0.56	
		8.51	8.48	7.82	564.73	1.279	2.26	0.58	
		8.53	8.69	7.49	555.51	1.182	2.13	0.55	
0.58	0.58	8.09	8.26	7.14	477.12	1.092	2.29	0.59	0.59
		8.42	8.78	6.74	498.27	1.005	2.02	0.52	
		8.24	8.38	6.61	456.43	0.961	2.11	0.54	
		8.59	8.61	7.06	521.99	1.207	2.31	0.60	
		8.43	8.28	7.06	493.06	1.23	2.49	0.64	
		8.08	8.00	7.09	457.98	1.099	2.40	0.62	
	1.16	9.19	9.17	7.11	599.62	1.164	1.94	0.50	0.46
		9.37	9.27	7.06	613.57	1.099	1.79	0.46	

		9.19	9.30	7.09	605.75	1.139	1.88	0.49	
		9.10	9.06	6.96	573.82	1.107	1.93	0.50	
		9.35	9.40	6.76	594.14	1.038	1.75	0.45	
		9.09	9.03	7.01	575.40	1.1	1.91	0.49	
		9.70	9.78	6.58	624.20	0.935	1.50	0.39	
		9.55	9.58	7.01	641.12	1.101	1.72	0.44	
		9.55	9.45	6.96	628.03	1.072	1.71	0.44	
0.84	0.84	9.53	9.19	6.63	580.61	1.188	2.05	0.53	0.60
		9.14	9.45	6.63	572.78	1.227	2.14	0.55	
		9.30	9.09	6.76	571.15	1.241	2.17	0.56	
		9.40	9.37	6.73	592.89	1.269	2.14	0.55	
		9.68	9.70	6.86	643.95	1.84	2.86	0.74	
		9.40	9.42	6.83	605.10	1.446	2.39	0.62	
		9.34	9.58	6.51	582.50	1.439	2.47	0.64	
		9.64	9.76	6.92	651.08	1.622	2.49	0.64	
		9.60	9.66	6.80	630.60	1.469	2.33	0.60	
Fully		9.02	9.30	6.02	504.99				
dense		9.12	9.28	7.01	593.28				

Table S1.1 *Dimensions and relative density of the samples used for the compression experiments.*

Nozzle Size (mm)	*Theoretical Gap (mm)*	*Line Diameter (mm)*	*Gap (mm)*	*Pitch (mm)*	*d/p*	*Number of Layer*	*Compressive Strength (MPa)*	*Average Strength (MPa)*	*Number of Drops*
0.41	0.41	0.43	0.28	0.74	0.58	28	200.28	212.80	2
		0.42	0.28	0.74	0.57	28	317.03		3
						26	133.29		3
						28	200.6		3
	0.82	0.46	0.56	1.11	0.41	26	167.9	184.05	12
		0.53	0.51	1.12	0.47	26	248.95		3
		0.49	0.54	1.10	0.44	28	219.69		3
						28	221.13		3
						28	187.24		3
						26	59.38		12
0.58	0.58	0.55	0.40	1.03	0.54	18	382.43	202.23	3
		0.54	0.47	1.04	0.52	18	120.9		10
		0.54	0.45	1.03	0.53	18	113.27		17
						18	124.52		3
						18	214.81		2
						18	257.45		2
	1.16	0.61	0.89	1.56	0.39	18	82.82	79.54	12
		0.60	0.86	1.50	0.40	18	82.85		9
		0.62	0.88	1.53	0.41	18	85.79		11
		0.63	0.82	1.46	0.43	17	75.07		20
		0.63	0.75	1.53	0.41	17	73.96		13
		0.62	0.84	1.53	0.40	18	97.3		15
						14	36.9		8

						18	67.65		5
						18	113.53		3
0.84	0.84					12	121.56	159.94	3
						12	221.23		2
						12	160.72		4
		0.80	0.65	1.46	0.55	12	111.4		8
		0.95	0.53	1.49	0.64	12	154.57		4
		0.80	0.62	1.49	0.54	12	161.89		2
		0.82	0.58	1.50	0.55	12	140.27		11
		0.88	0.57	1.48	0.60	12	137.8		14
		0.82	0.61	1.46	0.56	12	230.01		4
Fully dense							156.11	170.89	7
							185.67		4

Table S1.2 *Measurement of the dimensions and mechanical properties of the woodpile and fully dense samples.*

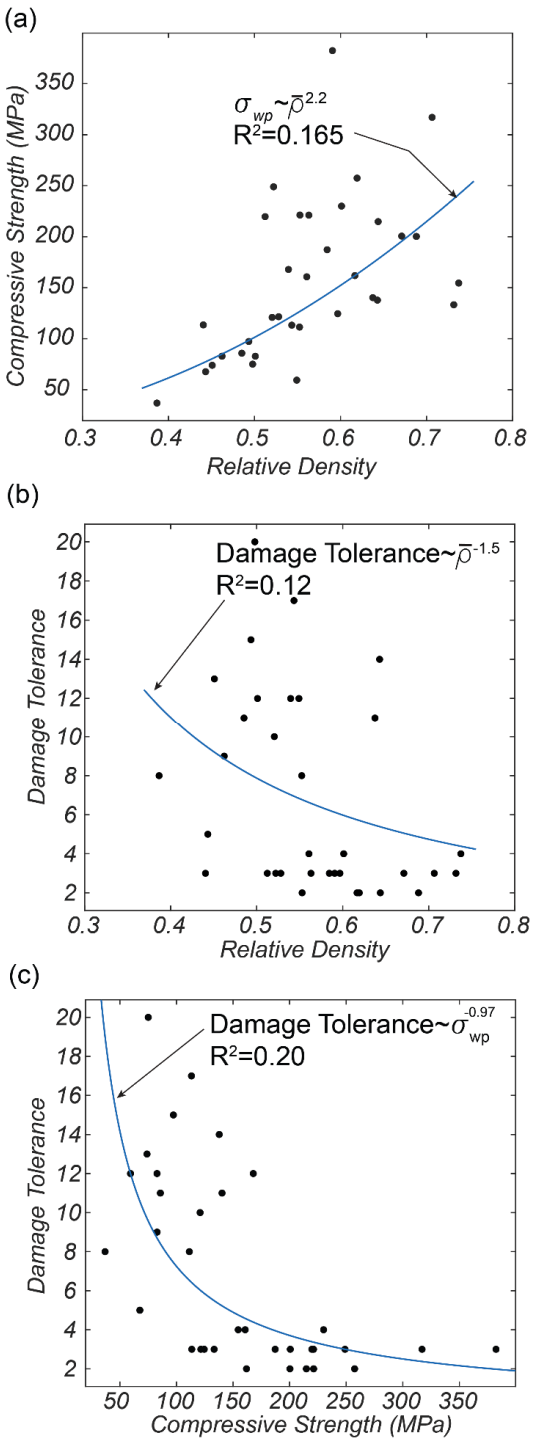

Figure S1.2. *Power-law fits extracted from the experimental data: (a) Compressive strength VS relative density; (b) Damage tolerance (interpreted as the number of load drops in the experiment) VS relative density; (c) Damage tolerance VS compressive strength.*

Supplementary Materials 2

Printability of Ceramic Matrix Composites for Direct Ink Writing

S2.1 Introduction

Ceramic Matrix Composites (CMC) maintain the best properties of ceramic materials (high melting point and thermal stability, high stiffness, low density) while significantly increasing the fracture toughness and hence the tensile strength. The global market size of CMC is predicted to grow from USD 8.8 billion in 2021 to USD 25.0 billion by 2031 (data extracted from https://www.marketsandmarkets.com/Market-Reports/ceramic-matrix-composites-market-60146548.html). CMCs, including SiC/SiC, Al_2O_3/SiC and C/C, are stable at elevated temperatures, with maximum operating temperatures ranging from 1300°C to 2000°C, and have high mechanical properties. Thanks to the reinforcement/matrix interaction, CMCs have a higher toughness and fracture resistance than monolithic ceramics (with toughness of ~ 5 and 7.5 $MPa.m^{1/2}$ for Si_3N_4 and Si_3N_4/SiC1, respectively). To further increase the tensile strength of CMCs, it would be essential to design structures with features at the nanoscale, thus reducing the size of the average defect below the level required for brittle fracture and allowing the materials to perform at their theoretical strength. Multiscale CMC mechanical metamaterials with overall dimensions at the macroscale and minimum feature sizes at the micro and nanoscale can offer a potential solution. DIW is exceptionally suited for the printing of CMC structures as an optimized base ink can be easily reinforced.

In this chapter, several CMC inks containing SiC whiskers 10 vol% will be developed.

S2.2 Preliminary data

S2.2.1 Ink development

The CMC inks are created from the base alumina ink. Since the alumina ink is already highly loaded, the addition of the reinforcement would bring the total ceramic volume fraction close to or over the maximum volume fraction, ϕ_{max} (ϕ_{max}=0.64 for a monodispersed system). As it has been shown in the previous chapter, the alumina ink is suitable for the printing of woodpile structures, therefore, the total volume fraction of ceramic is maintained close to the alumina volume fraction in the base ink to ensure similar rheology. The formulation of the inks is kept to as close as possible from the base ink for two main reasons: (1) to compare the effect of the reinforcement on the rheology and the flow of the ink, (2) to simplify the design of the inks. For the development of the ink, boundaries on the volume fraction can be set to define the region where the ink is worth testing in the rheometer. For example, if at the end of the mixing process, the ink can flow under its own weight then the yield stress is too small; conversely, if the ink seems to dry and form agglomerates, then the total volume fraction is too high for DIW. Those observations during the mixing process help narrowing down a range of volume fraction of ceramics that could be suitable for DIW without requiring to test the rheology for each formulation. The addition of the reinforcement could exhibit interesting change in the rheology as the reinforcement is often of different shapes, sizes, or surface interactions from the matrix particles. Table S2.1 shows the reinforcement used for this study with their shape and their dimensions.

	SiC
Shape	Whiskers
Size	Average diameter: 0.1 – 0.8 µm Length: 2.0 - 60µm

Table S2.1. *Description of SiC reinforcement (shape, dimensions) used for the fabrication of CMC ink.*

S2.2.2 Rheology and flow behavior

The control of the rheology for those inks is less essential on the printability as only lines will be printed directly on the substrate. No tall structure or over hanged line will be printed for this study making the tuning of the rheology more flexible. Figure S2.1 shows the rheological behavior of the ink. The rheology of the Alumina/SiC ink is similar to the rheology of the base ink. The shear-thinning behavior is more predominant in the CMC ink which is attributed to a lower total volume fraction of ceramic and the aspect ratio of the whiskers which once aligned with the flow have less resistance to it.

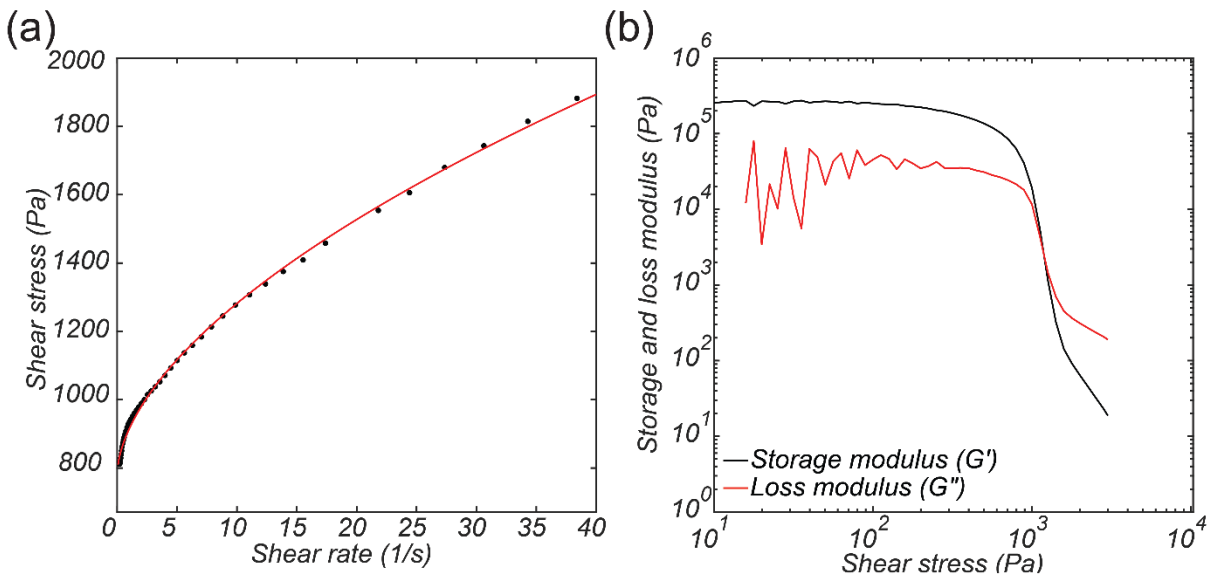

Figure S2.1. *(a) Shear stress vs shear rate for the alumina/SiC ink. (b) Storage and loss moduli for the alumina/SiC ink, showing a yield stress of ~10^3 Pa.*

As previously done, the Hershel-Bulkley parameters were extracted from the fit of the shear stress vs shear rate curve and integrated into the analytical model to obtain a relationship between the tabletop speed and the pressure. In parallel, the mass flow rate was experimentally measured for different values of pressure then converted into the tabletop speed as shown in Figure S2.2a. Some woodpile structures were printed by selecting sets of printing parameters as shown Figure S2.2b. Overall the quality of the woodpile structures is good. However, the print of woodpile structures with pressure of 138 kPa for 410 µm and 580 µm nozzle diameter, and of 207 kPa for 410 µm have failed but by slightly readjusting the tabletop speed excellent print quality can be achieved as shown in Figure S2.3. This slight difference can be attributed to the slight difference in the mixing from batch to batch. Figure S2.4 shows the comparison between the model and experiment for different nozzle sizes. As expected, the results are similar to the alumina ink and the model is in good agreement with the experiment at low pressure and diverge with the increase of the pressure. However, the ink features a different behavior at higher pressure as the speed does

not plateau. This difference could be attributed to the lower volume fraction lowering the probability of jamming at the nozzle tip, the aspect ratio of the whiskers facilitating the flow or interparticle interaction between the silicon carbide and alumina or dispersant.

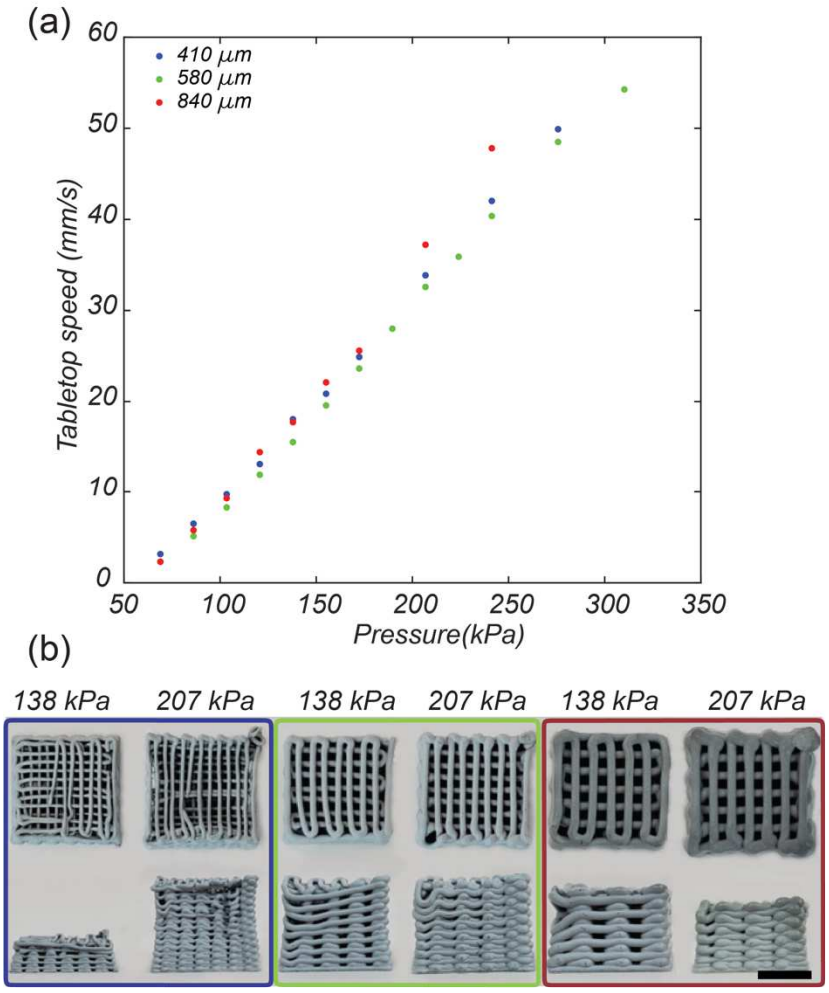

Figure S2.2. *(a) Relationship between the tabletop speed and the pressure applied for different nozzle diameters (410 μm, 580 μm and 840 μm) for the alumina/SiC ink. (b) woodpile structures printed for different pressures and nozzle sizes. Scale bar: 5 mm.*

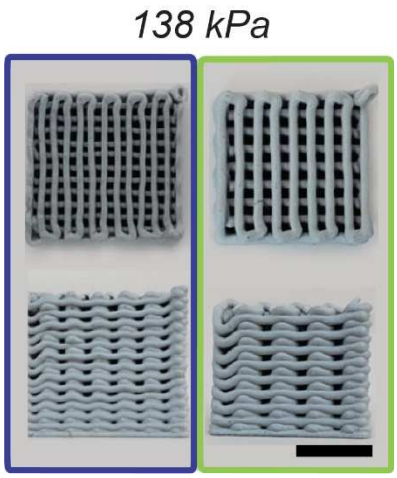

Figure S2.3. *Woodpile structures printed with slightly readjusted printed parameters for the diameter of 410 µm and 580 µm at a pressure of 138 kPa.*

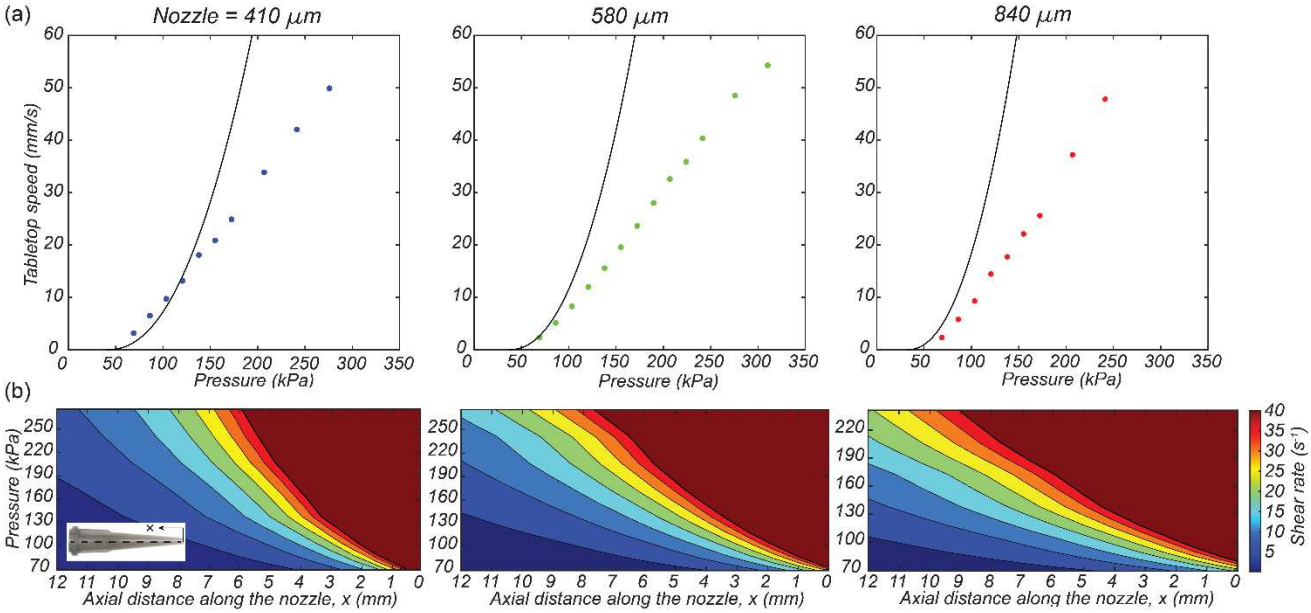

Figure S2.4. *(a) Comparison between the analytical model and the experimental measurements for the alumina/SiC ink. (b) Map of the maximum shear rate along the conical nozzle, at different dispenser pressure values. Results are presented for three nozzle diameters: 410 µm, 580 µm and 840 µm.*

	Al_2O_3 particles (vol%)	DI water (vol%)	PVP (vol%)	Dispersant (vol%)	SiC (vol%)
Base ink	53	32.9	9.9	4.2	0
Al_2O_3/-10 vol% SiC	45	35.9	9.9	4.2	5

Table S2.2. *Composition of the CMC ink. The base ink is the alumina ink used in previous chapter.*

S2.2.3 Printing of individual lines

The printing of lines had a major obstacle to be overcome, namely the warping of the lines during drying and sintering. This warping, which is attributed to the non-homogenous drying and sintering, was often severe and caused fracture of the lines. The investigation was performed on the alumina ink as a proof of concept. For post-printing drying, the substrate was coated with Teflon spray to allow the lines to move while drying. Plus, some oil was added on top of the lines after printing to slow down the evaporation of the water creating a more homogeneous drying. Therefore, the lines remained flat, and no warping was observed.

By applying the same sintering cycle as the one for the alumina woodpile, warping of pure alumina lines was also observed. The warping was identified to happen after the burn-out of the polymer. Several parameters such as rate, sintering temperature, extra dwells were tuned to lower the effect of the warping. The rate of the ramp up was lowered as well as the sintering temperature, and dwells were added. After numerous iterations, the optimum sintering cycle was found to be a ramp at 5°C/min up to 700°C followed by a dwell time of one hour. Then a ramp at 1 °C/min up to 1500°C with dwell for one hour at every 100°C beyond 1100°C. Plus, the lines were sandwiched between two blocs of alumina to constraint them. Following this protocol, the lines remained completely flat after sintering. To conclude, we were able to print lines of different CMC inks with

different reinforcement contents and sinter them without distortions during drying or sintering. Even though the warping of the lines is eliminated, the lines tend to stick onto the blocs which might damage the lines and create internal flaws. This issue will have to be addressed.

S2.2.4 Sintering of Alumina/Silicon carbide composites

Whereas oxide ceramics can be sintered in the ambient air since they are stable at high temperature, the introduction of silicon carbide reinforcement in the alumina matrix makes the sintering more complex. The Alumina/SiC composites were sintered in air following the alumina woodpile structure cycle for different sintering temperatures (1400, 1500 and 1600 °C) to investigate the oxidation of the whiskers. Figure S2.5 shows the TGA and DSC of the Al_2O_3 during sintering in air and in argon. The decomposition of the polymer is observed around 400°C with an important drop in the mass percent. As the sintering of alumina is stable process any change above the decomposition of the polymer can be attributed to the presence of SiC. The reaction of the SiC whiskers appears to be more predominant when sintered in air where there is an excess of oxygen than in an inert gas. This reaction is happening as low as 1100°C. Mass gain is observed beyond this point which could be attributed to the reaction of the SiC with oxygen. A small drop in mass is observed at high temperature in Figure S2.5b which can be attributed to the reaction of Al_2O_3 at the surface of the SiC to create mullite.

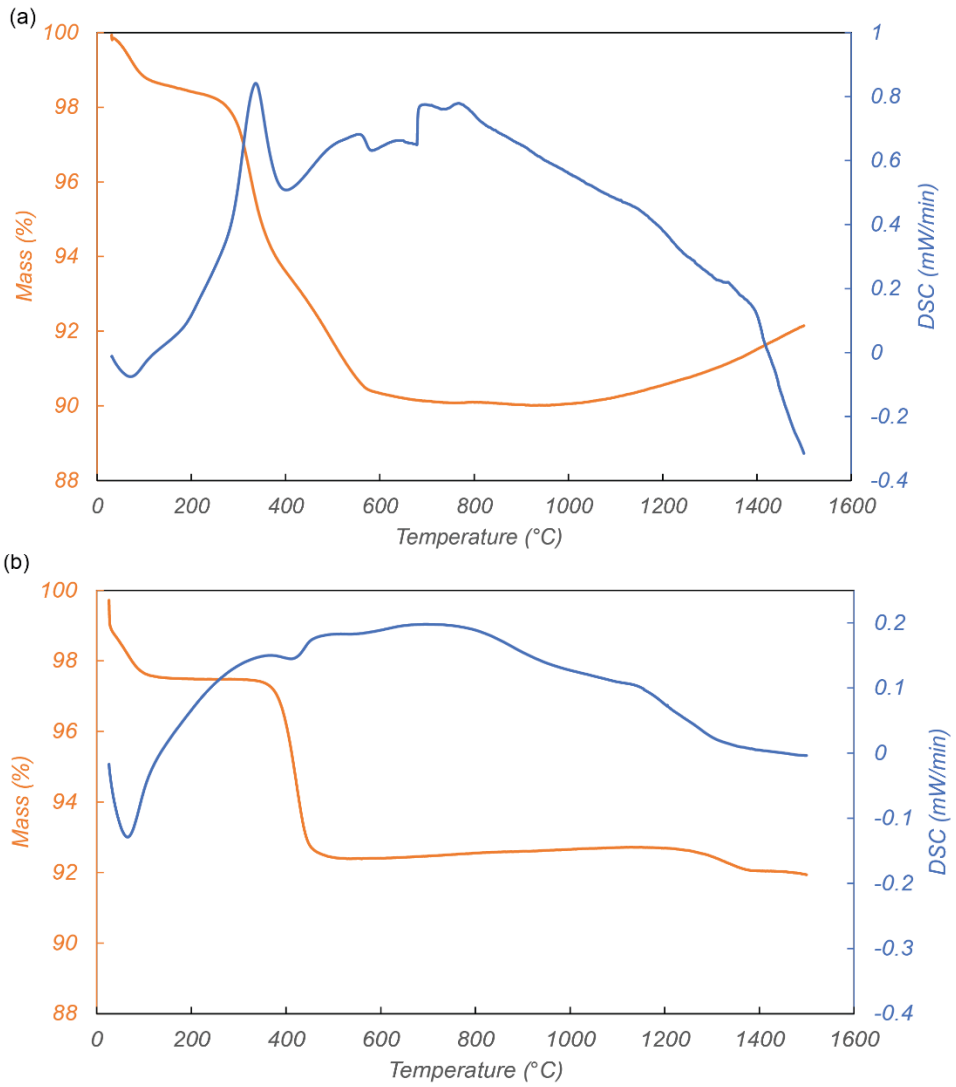

Figure S2.5. *TGA/DSC of Al_2O_3/SiC composites in (a) air and (b) argon.*

Furthermore, the reaction of the whiskers with Al_2O_3 in air is confirmed by using XRD for sintered samples at different temperatures. Several types of secondary phases have been identified such as AlSiOC type-phase, AlSiO type-phase at 1500 °C and 1600 °C and $Al_4C_4O_3$ at 1400 °C. The peak corresponding to the SiC phase is really small, which might imply that the whiskers are consumed and only few remained. No further work on the identification of secondary phases will be performed, as it is out of the scope of this chapter. The need to use an inert gas to sinter the

Al_2O_3/ SiC composite is crucial to limit the reaction of SiC, and guarantee that the reinforcement can remain intact.

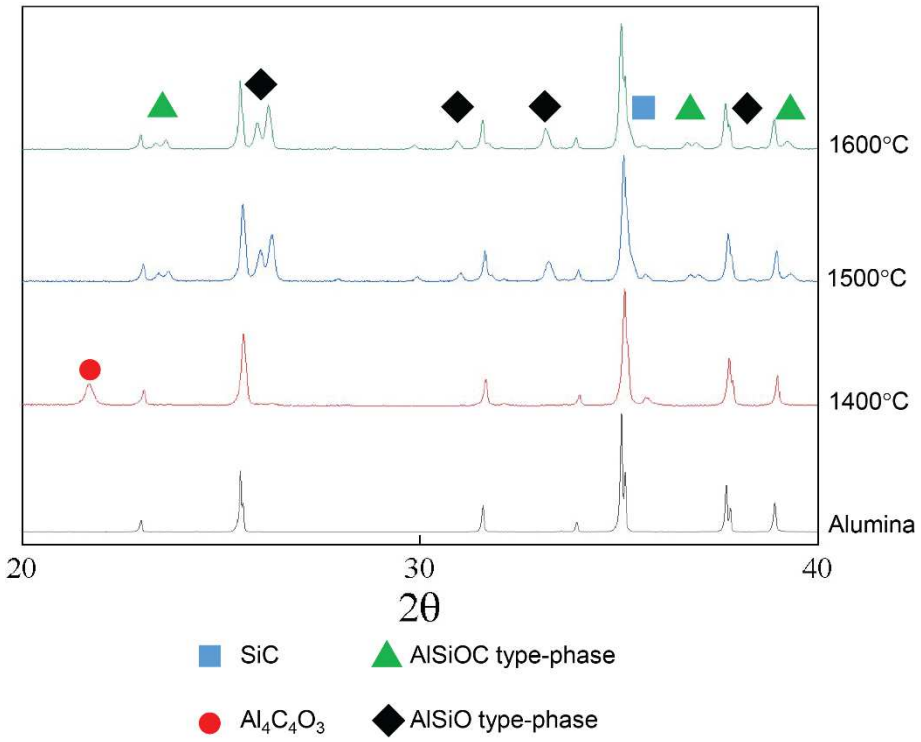

Figure S2.6. *XRD pattern of the alumina/SiC samples sintered at different sintering temperatures in air. The reference is the alumina sample sintered at 1600°C. The SiC oxidizes in air during sintering creating secondary phases.*

Supplementary Materials 3

A high-throughput process for mechanical characterization of ceramic materials produced by Direct Ink Writing

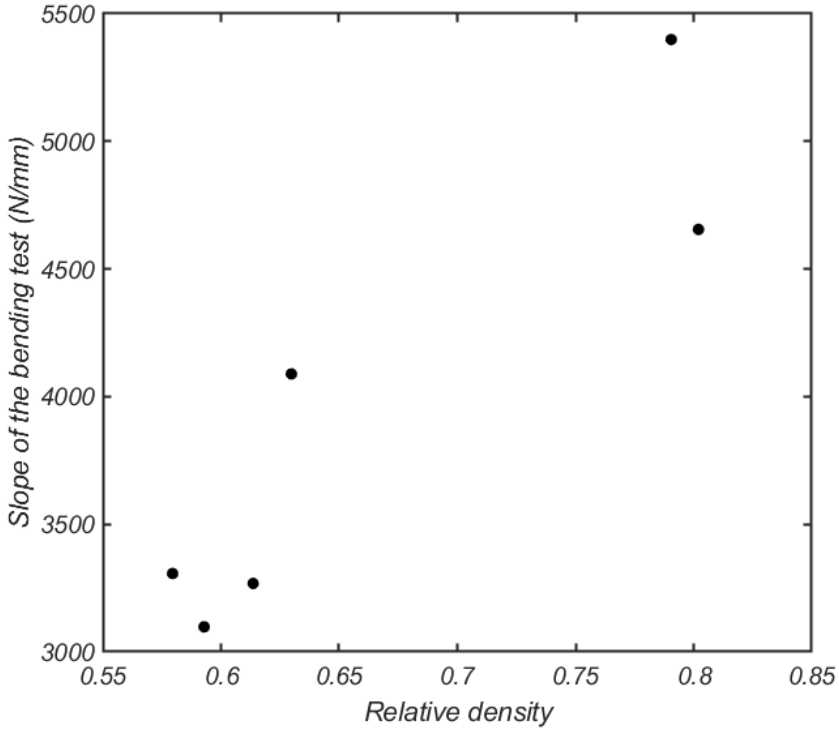

Figure S3.1. *Relationship between the slope extracted from load/displacement of the 3-point bending test and the relative density for the alumina sandwich structures.*

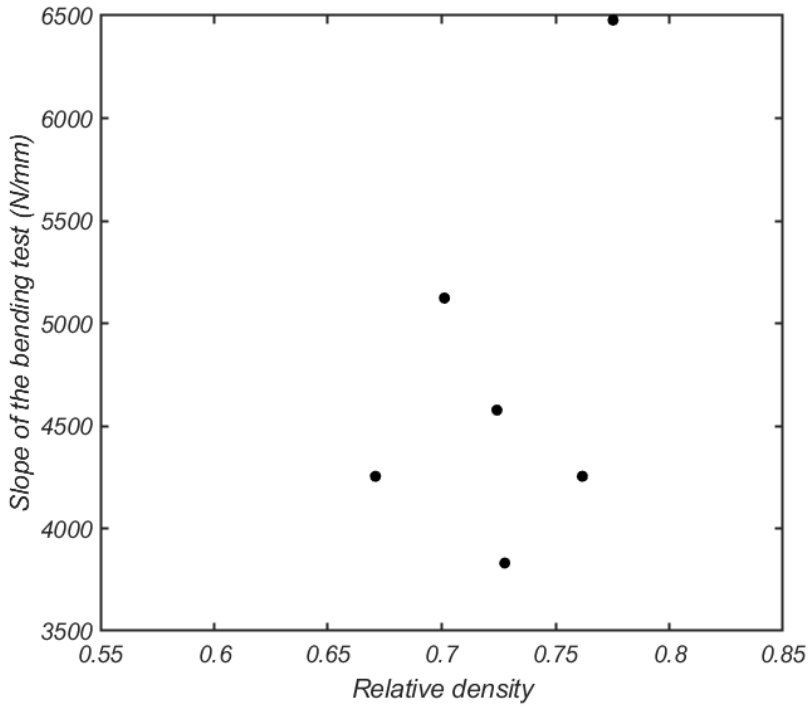

Figure S3.2. *Relationship between the slope extracted from load/displacement of the 3-point bending test and the relative density for the ZTA sandwich structures.*